

AD-A053 585

NORTH CAROLINA STATE UNIV RALEIGH DEPT OF ELECTRICAL--ETC F/G 20/12
A THEORETICAL SEARCH FOR SUPER-VELOCITY SEMICONDUCTORS.(U)
JAN 78 M A LITTLEJOHN, J R HAUSER

N00014-76-C-0480

NL

UNCLASSIFIED

1 OF 2
AD
A053 585



AD NO.

DDC FILE COPY

AD A 053585

REPORT DOCUMENTATION PAGE		READ INSTRUCTIONS BEFORE COMPLETING FORM
1. REPORT NUMBER	2. GOVT ACCESSION NO.	3. RECIPIENT'S CATALOG NUMBER
4. TITLE (and Subtitle) A THEORETICAL SEARCH FOR SUPER-VELOCITY SEMICONDUCTORS		5. TYPE OF REPORT & PERIOD COVERED Technical Annual 1/1/77 - 12/31/77
7. AUTHOR(s) M. A. / Littlejohn, J. R. / Hauser T. H. / Glisson		6. PERFORMING ORG. REPORT NUMBER 8. CONTRACT OR GRANT NUMBER(s) N00014-76-C-0480
9. PERFORMING ORGANIZATION NAME AND ADDRESS N. C. State University Department of Electrical Engineering Raleigh, NC 27650		10. PROGRAM ELEMENT PROJECT, TASK AREA & WORK UNIT NUMBERS PE 61153N RR 021-02-03 NR 243-006
11. CONTROLLING OFFICE NAME AND ADDRESS Office of Naval Research		12. REPORT DATE Jan 1978
14. MONITORING AGENCY NAME & ADDRESS (if different from Controlling Office) Annual rept. 1 Jan - 31 Dec 77		13. NUMBER OF PAGES 114 p
16. DISTRIBUTION STATEMENT (of this Report) RR 02102 RR 0210203		15. SECURITY CLASS. (of this report) Unclassified
15a. DECLASSIFICATION/DOWNGRADING SCHEDULE		
17. DISTRIBUTION STATEMENT (of the abstract entered in Block 20, if different from Report) Approved for Public Release; distribution unlimited.		
18. SUPPLEMENTARY NOTES ONR Scientific Officer; Tel. (202) 696-4218		
19. KEY WORDS (Continue on reverse side if necessary and identify by block number) III-V Compound semiconductors, III-V Alloys, High-Field Transport, III-V Semiconductor Devices, Microwave devices.		
20. ABSTRACT (Continue on reverse side if necessary and identify by block number) This report presents the results of research on carrier transport in III-V semiconducting compounds and alloys and the performance of microwave devices fabricated from those compounds and alloys.		

404 862

DDC
 RECEIVED
 MAY 4 1978
 REGISTERED
 B

INDEX

	<u>Page</u>
1. SUMMARY OF WORK -----	1
2. APPENDIX A: PUBLICATIONS FOR 1977 -----	3
3. DISTRIBUTION LIST -----	112

ACCESSION for	
NTIS	White Section <input checked="" type="checkbox"/>
DDC	Buff Section <input type="checkbox"/>
UNANNOUNCED	<input type="checkbox"/>
JUSTIFICATION _____	
BY _____	
DISTRIBUTION/AVAILABILITY CODES	
Dist: _____ or SPECIAL	
A	23 E.L.

1. SUMMARY OF WORK

Many of the past year's research results have been described in seven publications. Reprints of those publications are included as Appendix A of this report, and will be referenced as A.1-A.7 in the following.

The specific topics addressed during the past year are:

1. Effects of alloy scattering on transport and device characteristics [A.1].
2. Origins of negative resistance in polar III-V semiconductors [A.2]
- *3. Transport in $\text{Ga}_{1-x}\text{In}_x\text{P}_{1-y}\text{As}_y$ [A.3].
- *4. Qualitative analysis of thin GaN films [A.4]
5. Velocity-field characteristics of GaAs with the Γ -L-X conduction band ordering recently demonstrated by Aspnes⁺ [A.5]
6. Energy bandgap and lattice constant contours of III-V quaternary alloys. The contours for the 2:2 alloy systems of the form $\text{A}_{1-x}\text{B}_x\text{C}_{1-y}\text{D}_y$ were calculated first, and were published this year [A.6]. The contours for the 1:3 and 3:1 alloys were calculated and have been submitted for publication.
7. Performance of microwave MESFET's constructed from III-V compounds and alloys [A.7].
8. Refinement and extension of the Monte-Carlo transport programs
 - (a) Inclusion of p-state mixing
 - (b) Work toward modeling of degenerate materials
 - (c) Transient field program
 - (d) Position-dependent field program
9. Systematic search for promising materials (calculation of v-E characteristics of III-V compounds and alloys).

*This work was done during the grant period 1 Jan 76-31-Dec 76. The papers were published this year and are included for completeness.

+D. E. Aspnes, Phys. Rev. B 14, 5331 (1976).

The past year's research efforts have been quite fruitful. Considerable progress has been made in the areas of high-field transport and the identification of materials that show promise for microwave device application.

Appendix A: Publications for 1977

The following publications are collected in this Appendix for ready reference.

1. Littlejohn, M. A., J. R. Hauser, T. H. Glisson, D. K. Ferry, and J. W. Harrison. "Alloy Scattering and High-Field Transport in Ternary and Quaternary III-V semiconductors". Paper presented at the 1st Int. Conf. on Hot Electrons, Denton, EX, July 1977. Also accepted for publication in Dec. 77 issue of Sol. St. Electronics.
2. Hauser, J. R. , M. A. Littlejohn, and T. H. Glisson. "Negative Resistance and Peak Velocity in the Central (000) Valley of III-V Semiconductors". Paper presented at the 1st Int. Conf. on Hot Electrons, Denton, TX, July 1977.
3. Littlejohn, M. A., J. R. Hauser, and T. H. Glisson. "Velocity-Field Characteristics of $\text{Ga}_{1-x}\text{In}_x\text{P}_{1-y}\text{As}_y$ Quaternary Alloys". Appl. Phys. L., v30, no. 5 (March 1977).
4. Andrews, J. E., A. P. Duhamel, and M. A. Littlejohn. "Qualitative Analysis of Thin Gallium Nitride Films with Secondary Ion Mass Spectrometry". Anal. Chem., v49, no. 11 (September 1977).
5. Littlejohn, M. A., J. R. Hauser, and T. H. Glisson. "Velocity-Field Characteristics of GaAs with Γ_{6C}^C - X_{6C}^C Conduction-Band Ordering". J. Appl. Phys., v48, no. 11 (November 1977).
6. Glisson, T. H., J. R. Hauser, and M. A. Littlejohn. "Energy Bandgap and Lattice Constant Contours of III-V Quaternary Alloys". Accepted for publication in Dec. 1977 issue of J. Elec. Mat.
7. Littlejohn, M. A., J. R. Hauser, T. H. Glisson, and L. A. Arledge. "High Field Transport and Microwave MESFET Performance in Ternary and Quaternary III-V Semiconductors", Accepted for publication in the Proceedings of the Sixth Biennial Cornell Microwave Conference.

ALLOY SCATTERING AND HIGH FIELD TRANSPORT
IN TERNARY AND QUATERNARY III-V SEMICONDUCTORS*

M. A. Littlejohn, J. R. Hauser, T. H. Glisson
Electrical Engineering Department
N. C. State University
Raleigh, NC 27607

D. K. Ferry
Office of Naval Research
Arlington, VA 22217

J. W. Harrison
Research Triangle Institute
Research Triangle Park, NC 27709

ABSTRACT

A technique is described for the estimation of the influence of random potential alloy scattering on the high field transport properties of quaternary III-V semiconductors obtained by Monte Carlo simulation. The approach is based on an extension of a theoretical model for scattering in the ternary alloys. The magnitude of the scattering potential is an important parameter in alloy scattering, and three proposed models for calculating this potential are discussed. These are the energy bandgap difference, the electron affinity difference, and the heteropolar energy difference for the appropriate binary compounds.

The technique is used in the Monte Carlo method to study the influence of alloy scattering on the transport properties of III-V quaternary alloys. The results of this study are used in a device model to estimate device parameters for FET's.

*This work was supported by research contract No. N00014-70-A-0120-004 from the Office of Naval Research, Arlington, VA, and by research contract No. F33615-76-C-1265 from the Air Force Avionics Laboratory, Wright Patterson AFB, Ohio.

INTRODUCTION

In a semiconductor solid solution alloy, the scattering of free carriers due to the deviations from the perfect periodicity of the virtual crystal model, originally conceptualized by Nordheim [1], can be called random potential alloy scattering. The discussion of alloy scattering in relation to experimental electron mobility in III-V semiconductor ternary alloys has been based on an unpublished result of Brooks [2], as quoted and used for example in the results of Tietjen and Weisberg [3], Makowski and Glicksman [4], Glicksman, et al. [5], and Takeda, et al. [6]. Recently, theoretical calculations [7,8] have elaborated on physical models for alloy scattering in ternary III-V semiconductors, and these models have been applied in the Monte Carlo method to include the effects of alloy scattering in high field transport calculations for $\text{In}_{1-x}\text{P}_x\text{As}_x$ ternary alloys [9] and $\text{Ga}_{1-x}\text{In}_x\text{P}_{1-y}\text{As}_y$ quaternary alloys [10].

The III-V quaternary semiconductor alloys are becoming of great technological importance, and offer for device applications the unique feature that the energy band gap can be varied while maintaining a fixed lattice constant [11] by varying the alloy composition. It is important in these materials to be able to estimate the influence of alloy scattering on the electronic transport properties. The Monte Carlo method [12] is one of the more reliable techniques for making such an estimate, and this technique does become a predictive tool for III-V ternary and quaternary materials as long as reliable material property data are available for the binary constituents [7-10].

The purpose of this paper is to present a technique for estimating the effect of alloy scattering on transport properties of III-V ternary and quaternary semiconductors. This procedure has been used previously [9,10], and will be discussed in detail in this paper. The results obtained from the method applied in Monte Carlo transport calculations are also used to predict the influence of alloy scattering on device performance. The intent is to establish some reasonable upper- and lower-bounds for the effect of this scattering process in the ternary and quaternary materials.

TERNARY ALLOY SCATTERING POTENTIAL

The electron scattering rate in ternary semiconductors due to alloy scattering is important for the development of the quaternary scattering rate. Of particular importance is the scattering potential used in this calculation. The scattering rate (transition probability) for a ternary alloy ($A_{1-x}B_xC$) with nonparabolic energy bands is given in r.m.k.s. units by [7-9].

$$\frac{1}{\tau_{TA}} = \frac{3\pi}{8\sqrt{2}} \frac{(m^*)^{3/2}}{\hbar^4} [x(1-x)] \gamma(\epsilon) \frac{d\gamma(\epsilon)}{d\epsilon} \Omega |\Delta U|^2 S(\alpha) \quad 1)$$

where the notation used is described in Reference 10. Here $S(\alpha)$ is an energy-dependent parameter which describes the effect of ordering on the scattering rate [13]. In general, $0 \leq S \leq 1$, where $S=0$ for a perfectly ordered ternary (superlattice) and $S=1$ for a completely random alloy. The evaluation of S is complex and depends on the scattering potential, ΔU . In this paper the two cases $S=0, 1$, along with different scattering potentials for the case $S=1$, will be used to give lower- and upper-bound effects of alloy scattering, according to results obtained from the Monte Carlo method.

Besides the effect of ordering, the most significant parameter in Eqn. 1 is the scattering potential, ΔU . The derivation of Eqn. 1 is based on the Mott-inner potential [8], since this potential results in a relaxation time which leads to the accepted temperature dependence of electron mobility due to alloy scattering [5,7]. Previous calculations have used either a) the difference in energy band gaps between the binary

constituents [2-6], or b) the difference in electron affinities between the binary constituents [7-10] for this scattering potential.

Recently, Ferry [14] has suggested another form for the scattering potential based on the electronegativity theory of Phillips [15]. In this work, the energy difference between the bonding and antibonding hybridized molecular (sp^3) orbitals of a tetrahedrally coordinated crystal can be decomposed into contributions due to symmetric and antisymmetric potentials within a unit cell. This relation is described by [15]

$$E_G^2 = E_H^2 + C^2 \quad (2)$$

where E_G is the energy difference between the bonding and antibonding molecular states, E_H is the homopolar (symmetric) part and C is the heteropolar (antisymmetric) part of this energy difference. The heteropolar energy C represents the charge transfer or ionic contribution to E_G , and if in the alloy all bond lengths are equal, then it can be assumed that any fluctuations in the crystal potential arise from fluctuations in C [16]. This approach has had some limited success in explaining energy bandgap "bowing" effects in ternary semiconductors [16,17].

In Appendix A an expression for the scattering potential in a ternary alloy $A_{1-x}B_xC_x$ based on the electronegativity theory is given [14]. This expression is

$$\Delta U_{EN} = \frac{bZ}{4\pi\epsilon_0} \left[\frac{1}{r_A} - \frac{1}{r_B} \right] \exp[-k_s R_A] \quad (3)$$

Each quantity in this expression is defined in Appendix A.

Table 1 lists values of ΔU_{EN} for several ternary III-V alloys, along with ΔU_{EG} , the energy gap difference, and ΔU_{EA} , the electron affinity difference. The values of ΔU_{EN} are given in Table 1 for $x=0.5$, since there is a slight functional dependence of ΔU_{EN} on the alloy composition x . This is illustrated in Figure 1 where the compositional dependence of ΔU_{EN} is shown for several ternary alloys.

Figure 2 shows the effect of the use of these three scattering potentials on the velocity field characteristics for $\text{Ga}_{0.5}\text{In}_{0.5}\text{As}$ obtained from Monte Carlo calculations. Also shown in this figure is the characteristic for $S=0$ (no alloy scattering), and the curve for GaAs for comparison. These calculations have used the Γ -L-X conduction band ordering proposed for GaAs by Aspnes [18], and GaAs material parameters resulting in a good fit to experimental data [19]. Also given in Figure 2 is a tabulation of the low-field electron mobility for each scattering potential. In the recent work of Takeda, et al. [6] the experimental Hall mobility for $\text{Ga}_{.47}\text{In}_{.53}\text{As}$ is $8450 \text{ cm}^2/\text{volt sec}$. The Monte Carlo drift mobilities calculated by the maximum likelihood estimation technique [9,10] are $7350 \text{ cm}^2/\text{volt sec}$, $8300 \text{ cm}^2/\text{volt sec}$, and $8900 \text{ cm}^2/\text{volt sec}$ using ΔU_{EG} , ΔU_{EA} , and ΔU_{EN} , respectively, in the calculations. In general, the Hall mobility is greater than the drift mobility, so that based on these low field mobility calculations the scattering potential is possibly closer to that predicted by the electron affinity difference for this material.

If one examines the trends for the eighteen possible III-V ternary alloys it appears that often $\Delta U_{\text{EN}} < \Delta U_{\text{EA}} < \Delta U_{\text{EG}}$. However, this is not always true, as can be seen by the examples chosen for Table I. At best, this ordering of the ΔU 's seems fortuitous, and the ordering between ΔU_{EN} and ΔU_{EA} is especially in question. The band gap differences are the most accurately known parameters, while there are uncertainties in the available values of electron affinities [20] and covalent radii [21]. Thus the ordering in Table 1 could be the result of experimental variations,

especially between the ΔU_{EN} and the ΔU_{EA} . At the present time there are no firm theoretical or experimental reasons for choosing either scattering potential to evaluate the scattering rate due to alloy scattering in the ternaries. The point to be made is that alloy scattering as used in the Monte Carlo method and based on Eqn. 1 has a very detrimental effect on the transport properties of III-V ternary alloys and thus will be a factor in their use in devices, if the proposed models are correct.

QUATERNARY ALLOY SCATTERING RATE

Appendix B develops an extension of the ternary alloy scattering rate model to a quaternary material, $A_{1-x}B_xC_{1-y}D_y$, where A and B are group III atoms and C and D are group V atoms. This relation, which applies to the case where the A and B atoms are randomly distributed on the group III sites and the C and D atoms are randomly distributed on the group V sites, is given by

$$\frac{1}{\tau_{QA}} = K |\Delta U_Q(x,y)|^2, \quad (4)$$

where

$$K = \frac{3\pi}{8\sqrt{2}} \frac{(m^*)^{3/2}}{\hbar^4} \gamma(\epsilon) \frac{d\gamma(\epsilon)}{d\epsilon} \Omega,$$

and

$$|\Delta U_Q(x,y)|^2 = x(1-x)y^2 |\Delta U_{ABD}|^2 + x(1-x)(1-y)^2 |\Delta U_{ABC}|^2 \\ + y(1-y)x^2 |\Delta U_{BCD}|^2 + y(1-y)(1-x)^2 |\Delta U_{ACD}|^2$$

Here the effective mass, m^* , and the primitive cell volume, Ω , are calculated according to an interpolation procedure described previously [10].

Table 2 lists the quaternary alloy scattering potential ΔU_{QA} of Eqn. 4 at the mid-composition range $x=y=0.5$ for three quaternary alloys, $Ga_{1-x}In_xP_{1-y}As_y$, $Ga_{1-x}In_xP_{1-y}Sb_y$, and $Al_{1-x}In_xP_{1-y}As_y$ for each of the three ternary scattering potentials described in the last section. When comparing the results of Tables 1 and 2, the numbers given in Table 1 should be divided by 1/4 since the factor $x(1-x)$ in Eqn. 1 is not included in the Table 1 entries, whereas

the analogous factor is included in the entries of Table 2. In general, the quaternary scattering potential (not the scattering rate) is larger than the scattering potential for any of the four ternaries of which the quaternary is composed.

Figure 3 shows a plot of the quaternary alloy scattering parameter surface (ΔU_{QA}^2) for $\text{Ga}_{1-x}\text{In}_x\text{P}_{1-y}\text{As}_y$ in the compositional plane ($0 \leq x \leq 1$, $0 \leq y \leq 1$) for the case where the ternary scattering potentials are taken as the electron affinity differences. This figure shows a relative minimum of the quaternary alloy scattering parameter, ΔU_{QA}^2 , along a region which is very close to the compositions required for lattice matching this quaternary to InP substrates. This contributes to the large predicted peak velocity [10] of this particular quaternary alloy matched to InP. However, if the energy gap difference is used for the scattering potential the shape of the curve is shifted to a less favorable situation for minimum alloy scattering using InP as a substrate. Also, for compositions away from this region of minimum alloy scattering, the effects of alloy scattering are more detrimental. This can be seen in Figure 4, where the velocity-field characteristic for $\text{Ga}_{.55}\text{In}_{.45}\text{P}_{.1}\text{As}_{.9}$ are shown. Without alloy scattering these characteristics are nearly as attractive for device applications as those previously reported for $\text{Ga}_{.27}\text{In}_{.73}\text{P}_{.4}\text{As}_{.6}$. However, alloy scattering has a much more detrimental effect on the velocity-field curves for this particular composition. Also, for the composition shown in Figure 4, the effect of alloy scattering due to the use of ΔU_{EN} and ΔU_{EA} are almost identical, and only one velocity-field curve is shown for the calculations made from each of these alloy scattering potentials.

Other different effects of alloy scattering in quaternary alloys are illustrated in the velocity-field characteristics shown in Figures 5 and 6 for $\text{Al}_{.25}\text{In}_{.75}\text{P}_{.25}\text{As}_{.75}$ and $\text{Ga}_{.25}\text{In}_{.75}\text{P}_{.84}\text{Sb}_{.16}$, respectively. Since our interest in these materials has been primarily for FET's, the velocity-field curves are given for a doping level of 10^{17}cm^{-3} . It is seen that when alloy scattering is not used in the Monte Carlo simulations, the general features of these velocity-field curves are most attractive for a wide variety of solid state Gunn-effect electronic devices [24]. These features include large low-field mobility, high peak velocity, low threshold field, large energy band gap, large intervalley energy band separation, large negative differential mobility, and large peak-to-valley drift velocity ratio. When alloy scattering is included, its effects are generally detrimental to all these desirable properties. The extent of this degradation is certainly open to question, although the use of Monte Carlo method with the present alloy scattering model can provide a very good estimation of the range of this degradation.

At the same time the results of the Monte Carlo analysis can be used in device models to estimate device figures-of-merit and to examine their degradation from alloy scattering. This is illustrated in Table 3, where the FET model of Lehovec and Zuleeg [25] has been used to calculate some device parameters for MESFET's using the ternary and quaternary materials discussed in this paper. While this particular device model includes velocity saturation, but does not include a negative differential mobility, it has recently been used as a design model for GaAs MESFET's [26], with good results. The important comparison to be made is that between the device parameters for GaAs and the ternary and quaternary materials, and to consider the effect of alloy scattering on these device figures-of-merit. These three materials have properties which suggest possible improvements

in MESFET performance over GaAs (although the bandgap of 0.8 eV for $\text{Ga}_{.5}\text{In}_{.5}\text{As}$ may be somewhat too low), and these first-order model calculations verify this suggestion. Depending on the amount of alloy scattering and the physical correctness of the proposed model, alloy scattering reduces the advantages the materials offer. However, even considering the uncertainty in the magnitude of the alloy scattering the ternary and quaternary device parameters, such as f_T in Table 3, are seen to be improved considerably over the GaAs device parameters.

SUMMARY

This paper has presented techniques which can be used in the Monte Carlo method to estimate the effects of random potential alloy scattering on the high field transport properties of ternary and quaternary III-V semiconductors. These materials have many properties which suggest that their utilization in Gunn-effect electron devices can improve presently achievable device performance. At the same time, the effect of alloy scattering on material properties and characteristics which determine device performance present questions which challenge the extent of this conclusion.

The intent of this paper, and other publications [7-10], has been to offer a reasonable calculation of the effects of alloy scattering on the material and transport properties of ternary and quaternary III-V semiconductors. Of the three methods discussed for estimating the magnitude of the scattering potential, the bandgap difference is probably least accurate. The other two estimations represent two different views of the alloy scattering potential. For some materials the electron affinity difference technique and heteropolar energy difference technique give comparable magnitudes for the scattering potential. For other materials such as $\text{GaP}_{1-x}\text{As}_x$, $\text{AlP}_{1-x}\text{As}_x$ and $\text{GaP}_{1-x}\text{Sb}_x$ the electron affinity difference gives a very small alloy scattering effect while the heteropolar energy difference gives a large alloy scattering effect. Experimental data on these particular ternary alloys appears to be most useful in experimentally determining which of these models is most accurate for the III-V semiconductors.

List of References

1. L. Nordheim, *Annalen der Physik*, I. 9 607 and II. 9 641 (1931).
2. H. Brooks, unpublished results
3. J. J. Tietjen and L. R. Weisberg, *Appl. Phys. Lett.* 7 261 (1965).
4. L. Makowski and M. Glicksman, *J. Phys. Chem. Sol.* 34 487 (1973).
5. M. Glicksman, R. E. Enstrom, S. A. Mittleman, and J. R. Appert, *Phys. Rev B* 9 1621 (1974).
6. Y. Takdea, A. Sasaki, Y. Imamura, and T. Takagi, *Jour. Appl. Phys.* 47 5405 (1976).
7. J. W. Harrison and J. R. Hauser, *Jour. Appl. Phys.* 47 292 (1976).
8. J. W. Harrison and J. R. Hauser, *Phys. Rev. B* 9 5347 (1976).
9. J. R. Hauser, M. A. Littlejohn, and T. H. Glisson, *Appl. Phys. Lett.* 28 458 (1976).
10. M. A. Littlejohn, J. R. Hauser, and T. H. Glisson, *Appl. Phys. Lett.* 30 242 (1977).
11. C. J. Neuse, *Jour. Elec. Mat.* 6 253 (1977).
12. W. Fawcett, A. D. Boardman, and S. Swain, *J. Phys. Chem. Solids* 31 1963 (1970).
13. A. E. Asch and G. L. Hall, *Phys. Rev.* 132 1047 (1963).
14. D. K. Ferry, unpublished results.
15. J. C. Phillips, *Rev. Mod. Phys.* 42 317 (1970).
16. J. A. Van Vecten and T. K. Bergstresser, *Phys. Rev. B* 1 3351 (1970).
17. M. Altarelli, *Solid State Commun.* 15 1607 (1974).
18. D. E. Aspnes, *Phys. Rev. B* 14 5331 (1976).
19. M. A. Littlejohn, J. R. Hauser, and T. H. Glisson, *Appl. Phys. Lett.*, to be published, Aug. 15, 1977.
20. H. Kroemer, *CRC Crit. Rev. in Sol. State Sci.* 5 555 (1975).
21. J. A. Van Vecten, *Phys. Rev.* 182 891 (1969).
22. C. Kittel, *Introduction to Solid-State Physics*, 4th ed., John Wiley, New York, p. 279, 1971.

23. J. C. Phillips, Bonds and Bands in Semiconductors, Academic Press, New York, p. 22, 1973.
24. B. G. Basch and R. W. Englemann, Gunn-effect Electronics, John Wiley, Halstead Press, New York, 1975.
25. K. Lehovec and R. Zuleeg, Solid-St. Electron. 13 1415 (1970).
26. S. Asai, S. Okazaki, and H. Kodera, Solid-St. Electron. 19 461 (1976).

Table 1. Alloy scattering potentials in electron volts for several ternary III-V semiconductors for a) the electronegativity theory (ΔU_{EN}) b) the electron affinity difference (ΔU_{EA}) c) the energy band gap difference (ΔU_{EG}).

Material	a) $\Delta U_{EN}(x=0.5)$	b) ΔU_{EA}	c) ΔU_{EG}
$\text{Ga}_{1-x}\text{In}_x\text{As}$	0.529	0.830	1.08
$\text{InP}_{1-x}\text{As}_x$	0.581	0.50	0.981
$\text{GaP}_{1-x}\text{As}_x$	0.637	0.07	1.30 *
$\text{InAs}_{1-x}\text{Sb}_x$	0.801	0.310	0.184
$\text{Al}_{1-x}\text{In}_x\text{As}$	0.466	1.320	1.790
$\text{AlP}_{1-x}\text{As}_x$	0.636	0.08	0.267
$\text{Ga}_{1-x}\text{In}_x\text{P}$	0.559	0.40	0.92
$\text{Al}_{1-x}\text{In}_x\text{P}$	0.541	0.90	1.08
$\text{Ga}_{1-x}\text{In}_x\text{Sb}$	0.486	0.53	0.515
$\text{InP}_{1-x}\text{Sb}_x$	1.32	0.19	1.165
$\text{GaP}_{1-x}\text{Sb}_x$	1.51	0.06	1.57

Table 2. Quaternary alloy scattering parameter in electron volts for quaternary III-V semiconductors for a) the electronegativity theory (ΔU_{EN}) b) the electron affinity difference (ΔU_{EA}) c) the energy gap difference (ΔU_{EG}). The composition is chosen as $x=y=0.5$ for convenience.

Material	a) $\Delta U_{QA}(\Delta U_{EN})$	b) $\Delta U_{QA}(\Delta U_{EA})$	c) $\Delta U_{QA}(\Delta U_{EG})$
$Ga_{1-x}In_xP_{1-y}As_y$	0.289	0.263	0.540
$Ga_{1-x}In_xP_{1-y}Sb_y$	0.536	0.173	0.555
$Al_{1-x}In_xP_{1-y}As_y$	0.280	0.419	0.581

Table 3. Field-effect transistor parameters based on the model of Lehevec and Zuleeg [25] for the materials discussed in this paper, illustrating the effect of alloy scattering.

Material	g_m (mS)	C_{gs} (pf)	f_T (GHz)	r_{Ds} (ohms)	f_{max} (GHz)	τ_T (psec)
GaAs	30.48	.3640	13.33	445.06	24.55	9.25
$Ga_{.5}In_{.5}As$						
a) No alloy	61.39	.4886	20.00	202.31	35.23	5.79
b) ΔU_{EN}	54.61	.4884	17.79	228.28	31.40	6.51
c) ΔU_{EA}	48.39	.4914	15.67	247.39	27.12	7.39
d) ΔU_{EG}	43.24	.4910	14.02	278.39	24.32	8.27
$Ga_{.25}In_{.75}P_{.84}Sb_{.16}$						
a) No alloy	47.55	.3820	19.81	335.42	39.56	6.12
b) ΔU_{EA}	44.16	.3778	18.60	390.17	38.61	6.64
c) $\Delta U_{EN}, \Delta U_{EG}$	35.55	.3811	14.85	456.20	29.89	8.25
$Al_{.25}In_{.75}P_{.25}As_{.75}$						
a) No alloy	57.85	.4073	22.60	235.35	41.70	5.34
b) ΔU_{EN}	56.73	.4082	22.12	236.15	40.47	5.46
c) ΔU_{EA}	47.47	.4059	18.62	294.33	34.79	6.49
d) ΔU_{EG}	42.66	.4101	16.56	303.41	29.78	7.28

Notation: g_m = device transconductance, C_{gs} = gate-source capacitance, f_T = gain-bandwidth product, r_{Ds} = small signal drain-source resistance, f_{max} = maximum frequency of oscillation, τ_T = source-drain transit time.

These calculations were made for a device with a channel doping of 10^{17} cm^{-3} and the following dimensions: Channel width = $0.3 \mu\text{m}$, Channel length = $1.5 \mu\text{m}$, Channel depth = $300 \mu\text{m}$. The gate voltage = 0 volts and the drain voltage equals the pinch-off voltage.

Figure Captions

- Figure 1. Electron scattering potential for ternary alloys obtained from the heteropolar energy difference of the binary constituents.
- Figure 2. Velocity-field characteristic for $\text{Ga}_{.5}\text{In}_{.5}\text{As}$ obtained by Monte Carlo simulation. The notation is: Curve a) No alloy scattering $\mu = 9700 \text{ cm}^2/\text{volt}\cdot\text{sec}$; Curve b) Calculated using ΔU_{EN} , $\mu=8600 \text{ cm}^2/\text{volt sec}$; Curve c) Calculated using ΔU_{EN} , $\mu=8600 \text{ cm}^2/\text{volt sec}$; Curve e) GaAs, $N_{\text{D}}=10^{17} \text{ cm}^{-3}$, $\mu=4900 \text{ cm}^2/\text{volt sec}$.
- Note: For $\text{Ga}_{.47}\text{In}_{.53}\text{As}$ at $T=300\text{K}$ $\mu=8450 \text{ cm}^2/\text{volt sec}$ [ref.6].
- Figure 3. Quaternary alloy scattering parameter, $|\Delta U_{\text{QA}}|^2 (\text{eV}^2)$, for $\text{Ga}_{1-x}\text{In}_x\text{P}_{1-y}\text{As}_y$
- Figure 4. Velocity-field characteristic for $\text{Ga}_{.55}\text{In}_{.45}\text{P}_{.1}\text{As}_{.9}$ obtained by Monte Carlo simulation. The notation is: Curve a) No alloy scattering; Curve b) Calculated using ΔU_{EA} and ΔU_{EN} ; Curve c) Calculated using ΔU_{EG} .
- Figure 5. Velocity-field characteristic for $\text{Al}_{.25}\text{In}_{.75}\text{P}_{.25}\text{As}_{.75}$ obtained by Monte Carlo simulation. The notation is: Curve a) No alloy scattering; Curve b) Calculated using ΔU_{EN} ; Curve c) Calculated using ΔU_{EA} ; Curve d) Calculated using ΔU_{EG} .
- Figure 6. Velocity-field characteristic for $\text{Ga}_{.25}\text{In}_{.75}\text{P}_{.84}\text{Sb}_{.16}$ obtained by Monte Carlo simulation. The notation is: Curve a) No alloy scattering; Curve b) Calculated using ΔU_{EA} ; Curve c) Calculated using ΔU_{EN} and ΔU_{EG} .

APPENDIX A: TERNARY SCATTERING POTENTIAL FROM THE HETEROPOLAR CRYSTAL ENERGY

The heteropolar crystal energy in a binary $A^{III}B^V$ semiconductor is given in r.m.k.s. units by [15,16]

$$C_{AB} = \frac{b}{4\pi\epsilon_0} \left[\frac{Z_A}{r_A} - \frac{Z_B}{r_B} \right] \exp(-k_s R), \quad (A-1)$$

where Z_A and Z_B are the valence numbers (3 and 5, respectively), r_A and r_B are the covalent radii, $R = 0.5(r_A + r_B)$ is the A-B bond length, and k_s is the Thomas-Fermi screening wave number. The factor b accounts for the fact that the Thomas-Fermi approximation overestimates screening for small interatomic distances [16]. The Thomas-Fermi wave number is given in r.m.k.s. units by [22]

$$k_s^2 = \frac{1}{4} \left(\frac{\pi}{3} \right)^{1/3} \frac{a_B}{n_0}, \quad (A-2)$$

where n_0 is the valence electron density [15] and a_B is the Bohr radius. The valence electron density is then given by

$$n_0 = \frac{32}{a_0^3}, \quad (A-3)$$

where a_0 is the zincblende lattice constant.

If the binary materials $A^{III}C^V$ and $B^{III}C^V$ are alloyed to form $A_{1-x}^{III}B_x^{III}C^V$ and it is assumed that the A-C and B-C bond lengths are equal, then the fluctuations in the heteropolar energy in the alloy can be expressed as [16]

$$\Delta C = |C_{AC} - C_{BC}| \quad (A-4)$$

$$\text{or } \Delta C = \frac{bZ}{4\pi\epsilon_0} \left[\frac{1}{r_A} - \frac{1}{r_B} \right] \exp(-k_s R_A),$$

where Vegard's law is assumed to apply to both a_0 and R_A . Thus

$$a_0 = (1-x)a_{AC} + xa_{BC} \quad (A-5)$$

$$R_A = \frac{1}{2} [r_C + xr_B + (1-x)r_A]$$

If this fluctuation is taken to be the scattering potential, then $\Delta U_{EN} = \Delta C$, according to the electronegativity theory of Phillips [15,16]. Equations 1 through 5 are used to calculate the entries in Table 1. Here the rationalized covalent radii given by Phillips [23] have been used in the calculations.

APPENDIX B: QUATERNARY ALLOY SCATTERING RATE

For a quaternary III-V alloy, $A_{1-x}^{III} B_x^{III} C_{1-y}^V D_y^V$, the virtual crystal potentials for group III and V elements, respectively, are [1]

$$U_{III} = (1-x)U_A + xU_B \quad (B-1)$$

$$U_V = (1-y)U_C + yU_D,$$

where U_A , U_B , U_C , and U_D are the atomic crystal potentials of each element. If the A and B atoms are randomly placed on the group III sites and the B and C atoms are similarly placed on V sites, the scattering rates due to potential fluctuations of both III and V sites will be proportional to the square of the matrix elements and the probability of occurrence of each species of atom. The probabilities for occurrence in a random crystal are $(1-x)$, x , $(1-y)$, and y for A, B, C, and D atoms, respectively. The matrix elements are given by

$$|m_i|^2 = \left| \int \psi^* \Delta U_i \psi d\vec{r} \right|^2 \quad (B-2)$$

where $\Delta U_i = U_{III} - U_i$ for $i=A$ or B , and $\Delta U_i = U_V - U_i$ for $i=C, D$. Thus, the total scattering rate for the quaternary alloy is given by

$$\frac{1}{\tau_{QA}} \sim x(1-x)|M_{III}|^2 + y(1-y)|M_V|^2 \quad (B-3)$$

with

$$|M_{III}|^2 = \left| \int \psi^* (U_A - U_B) \psi d\vec{r} \right|^2 \quad (B-4)$$

$$|M_V|^2 = \left| \int \psi^* (U_C - U_D) \psi d\vec{r} \right|^2$$

If $U_A - U_B$ is regarded as the change in group III potential with group V atom fixed, and $U_C - U_D$ is regarded as the change in group V potential with group III atom fixed, then the composition weighted averages for $U_A - U_B$ and $U_C - U_D$ are

$$U_B - U_A = (1-y)(U_{BC} - U_{AC}) + y(U_{BD} - U_{AD}) \quad (B-5)$$

$$U_C - U_D = (1-x)(U_{BD} - U_{BC}) + x(U_{AD} - U_{AC})$$

Here $(U_{BC} - U_{AC})$ represents the difference in the effective potential for electrons with either group B or group A atoms on group III sites with a C atom definitely on a group V site, and so on for the other three terms.

By substitution of Eqn. (5) into Eqn. (4) and neglecting the "overlap" integrals one obtains

$$\frac{1}{\tau_{QA}} = K[x(1-x)y^2 |M_{ABD}|^2 + x(1-x)(1-y)^2 |M_{ABC}|^2 + y(1-y)x^2 |M_{BCD}|^2 + y(1-y)(1-x)^2 |M_{ACD}|^2] \quad (B-6)$$

where

$$|M_{ABD}|^2 = \left| \int \psi^* (U_{BD} - U_{AD}) \psi d\vec{r} \right|^2$$

with analogous expressions for the remaining matrix elements. Here the factor K is a quaternary material constant. If the Mott-inner potential model is used [8], the expression for the scattering rate for the quaternary alloy becomes

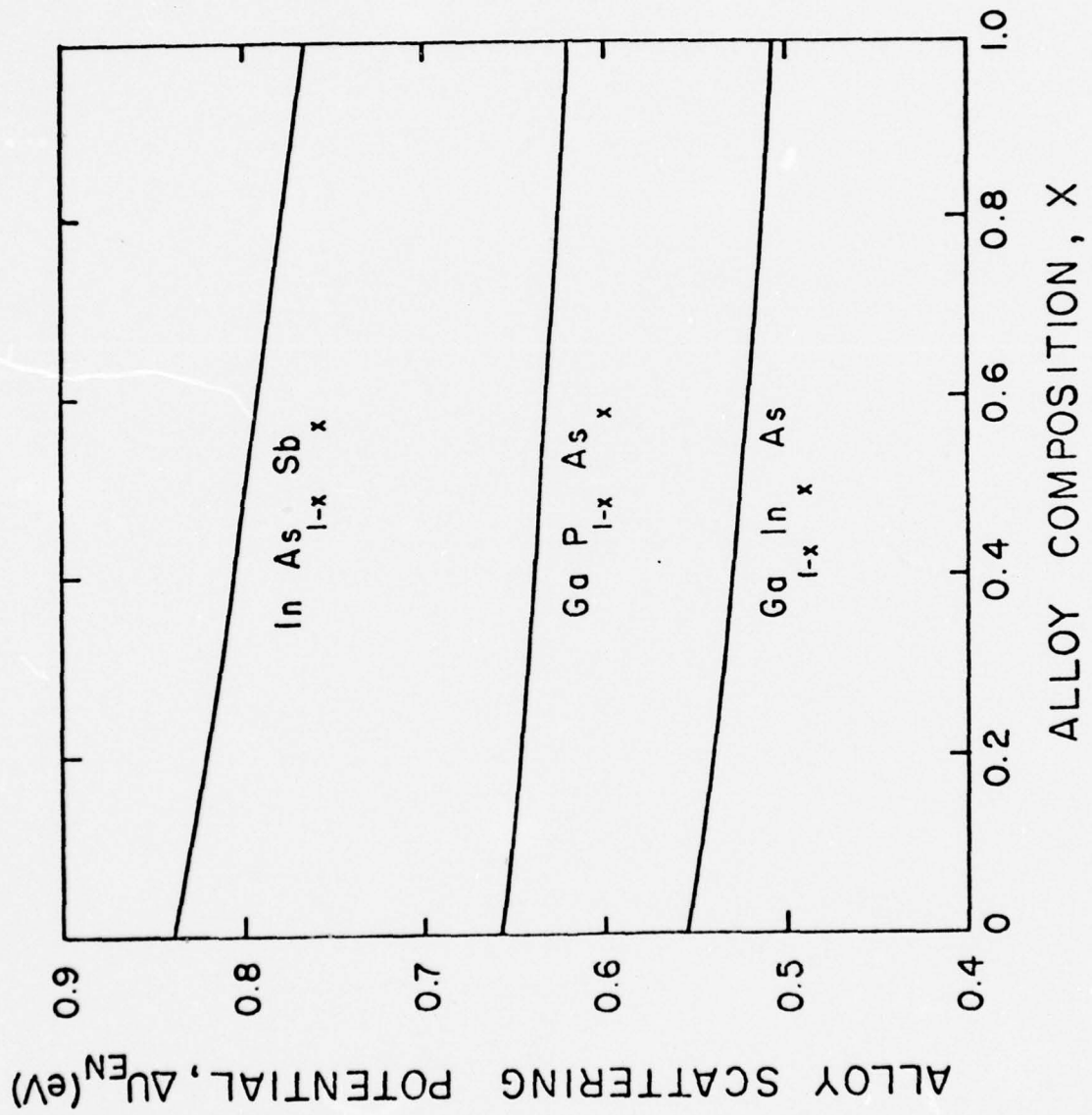
$$\frac{1}{\tau_{QA}} = \frac{3\pi}{8\sqrt{2}} \frac{(m^*)^{3/2}}{\hbar^4} \gamma(\epsilon) \frac{d\gamma}{d\epsilon} \Omega |\Delta U_Q(x,y)|^2, \quad (B-7)$$

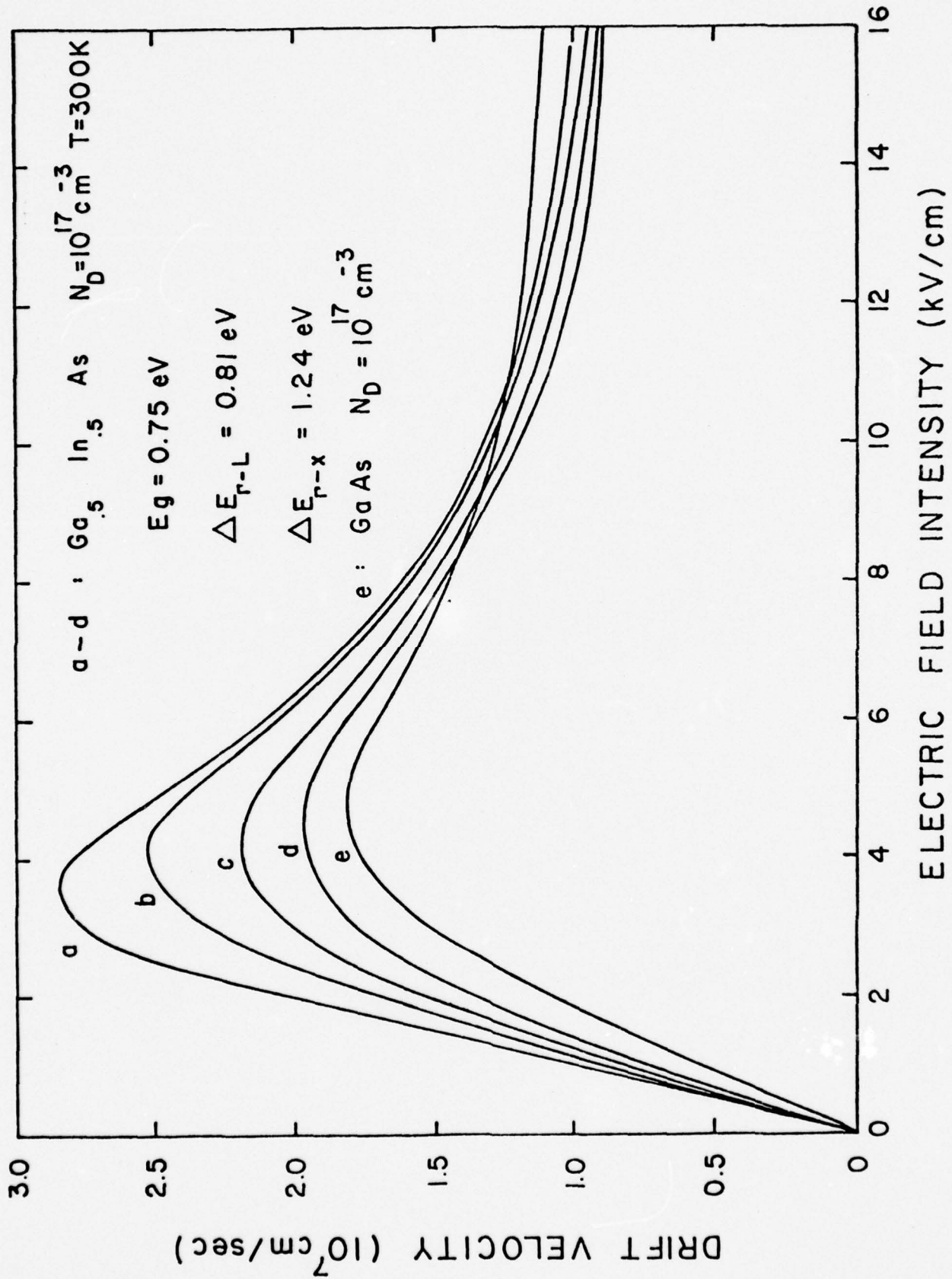
with

$$|\Delta U_Q(x,y)|^2 = x(1-x)y^2 |\Delta U_{ABD}|^2 + x(1-x)(1-y)^2 |\Delta U_{ABC}|^2 + y(1-y)x^2 |\Delta U_{BCD}|^2 + y(1-y)(1-x)^2 |\Delta U_{ACD}|^2$$

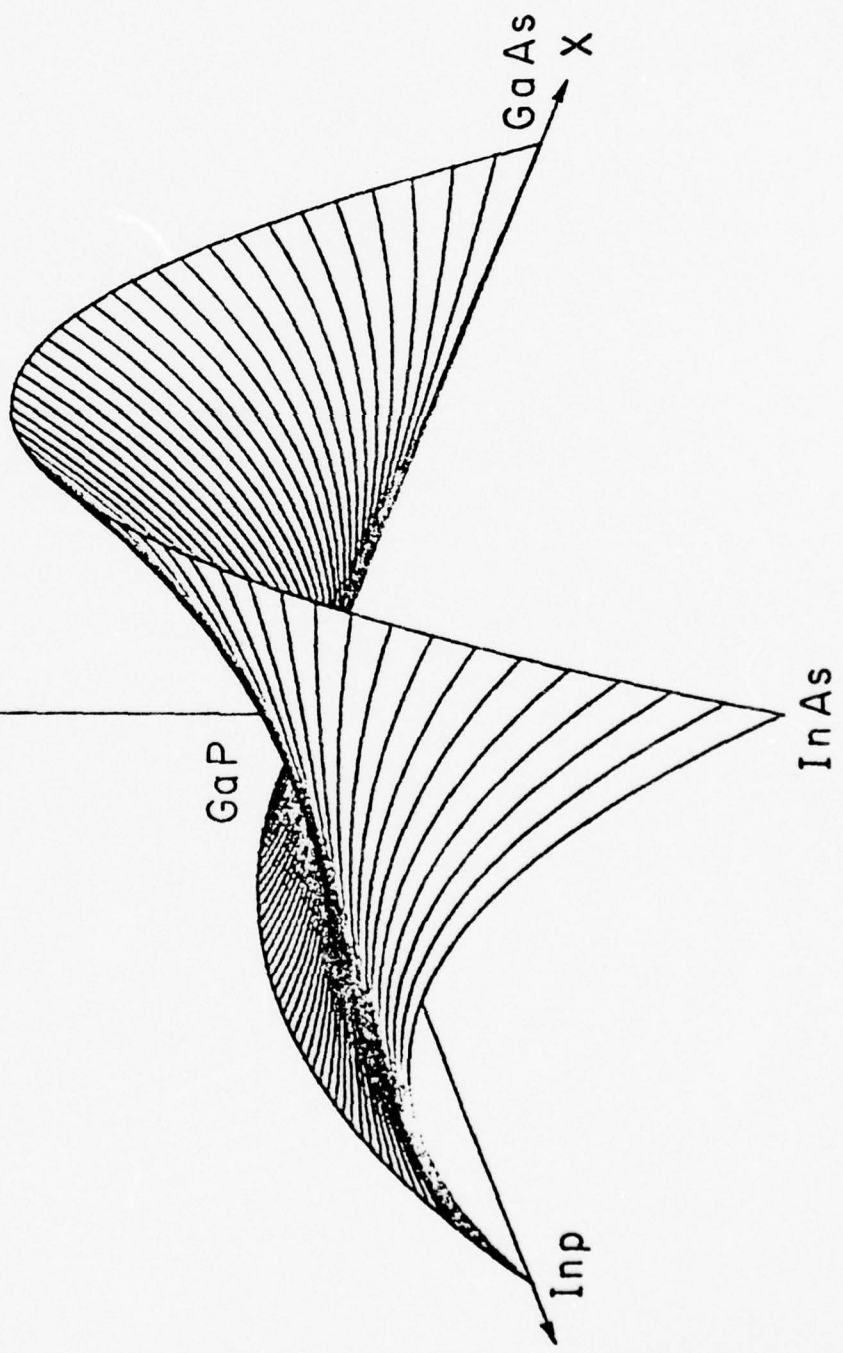
Here the ΔU 's on the r.h.s. of Eqn. 7 are ternary scattering potentials.

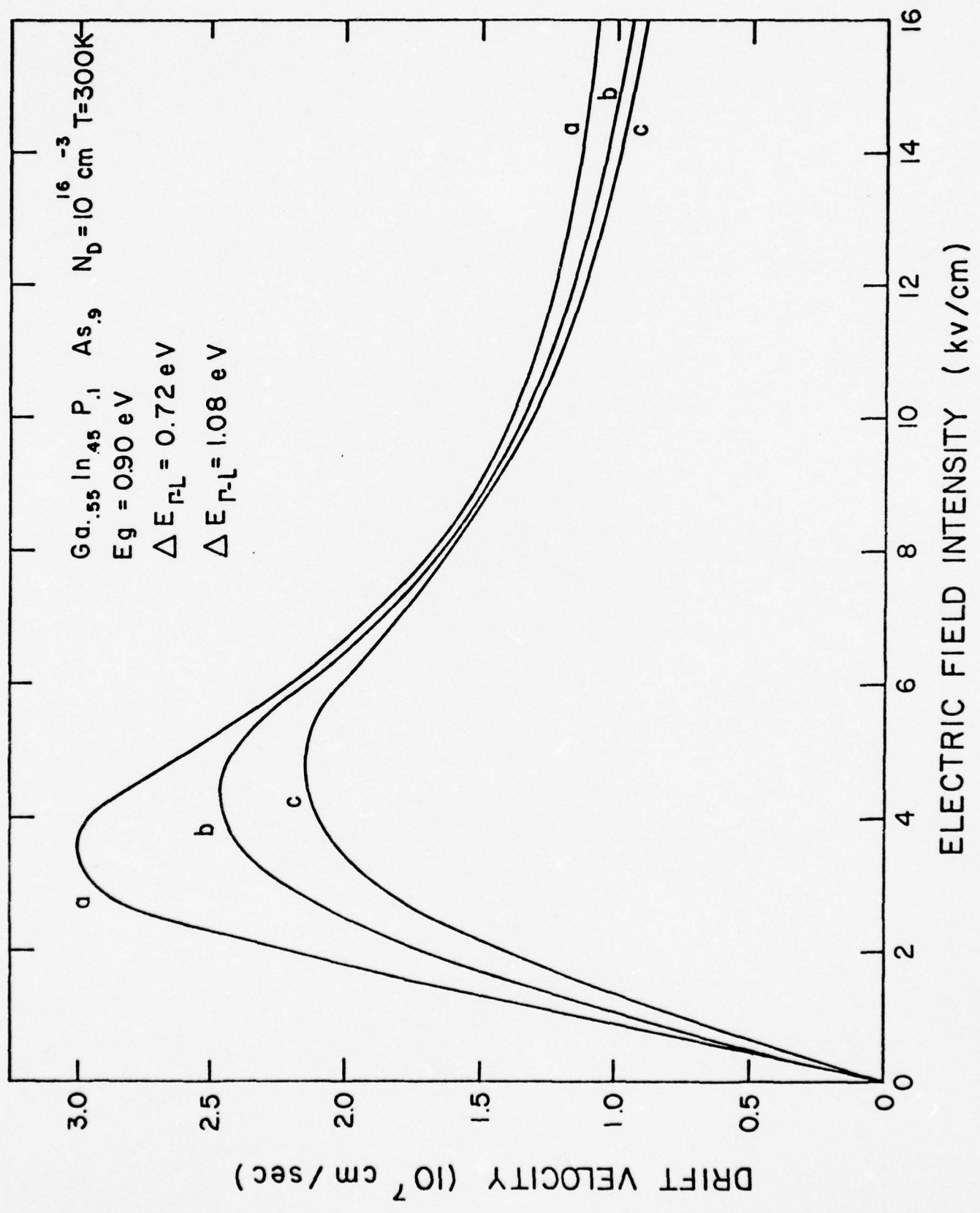
For example, ΔU_{ABD} is the scattering potential of the ternary $A_{1-x}B_xD$ and ΔU_{BCD} is the scattering potential of the ternary $BC_{1-y}D_y$. In addition, each material parameter in Eqn. 7 is a material parameter of the quaternary alloy, which can be estimated from binary and ternary material parameters by the interpolation procedures previously described [10].

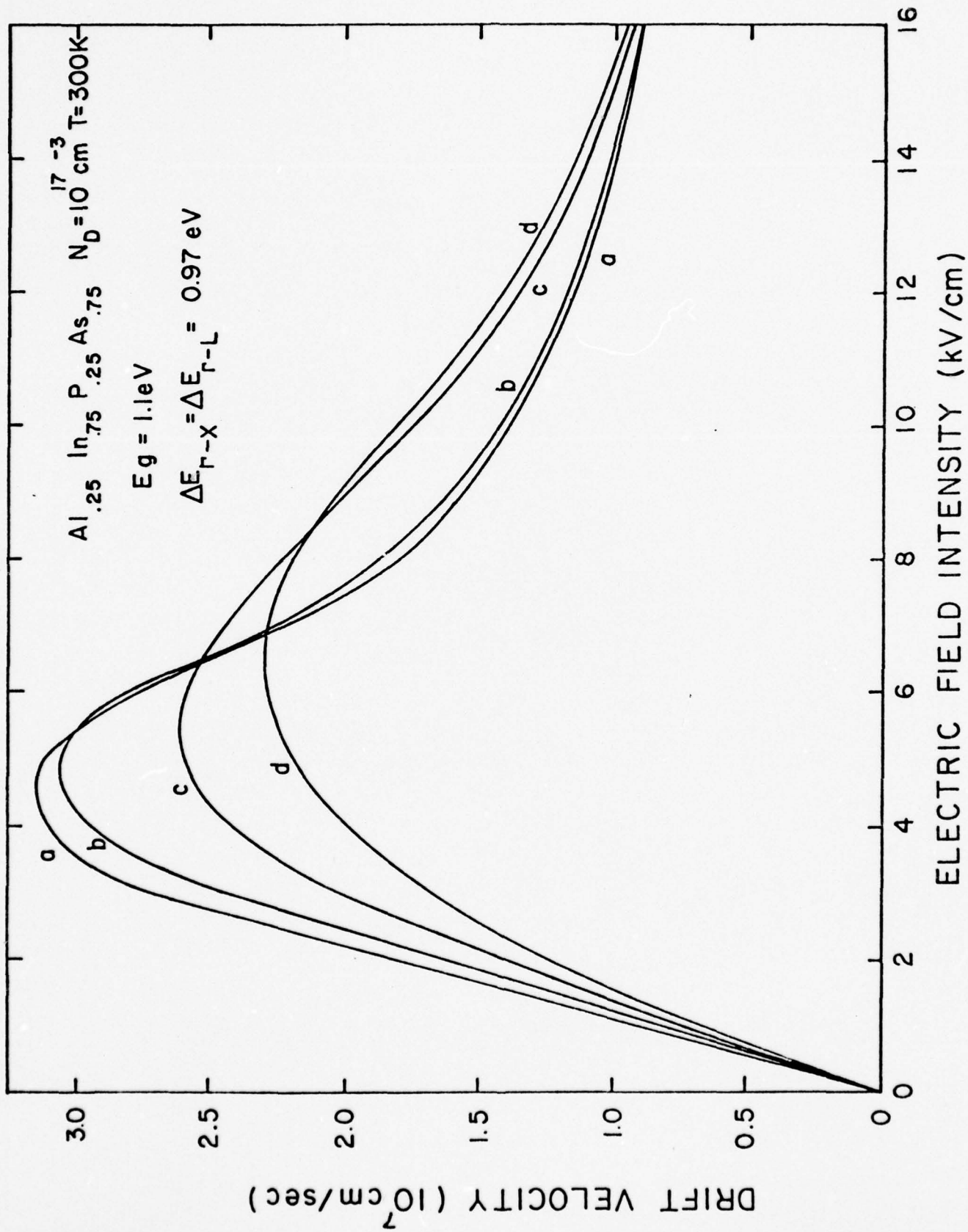


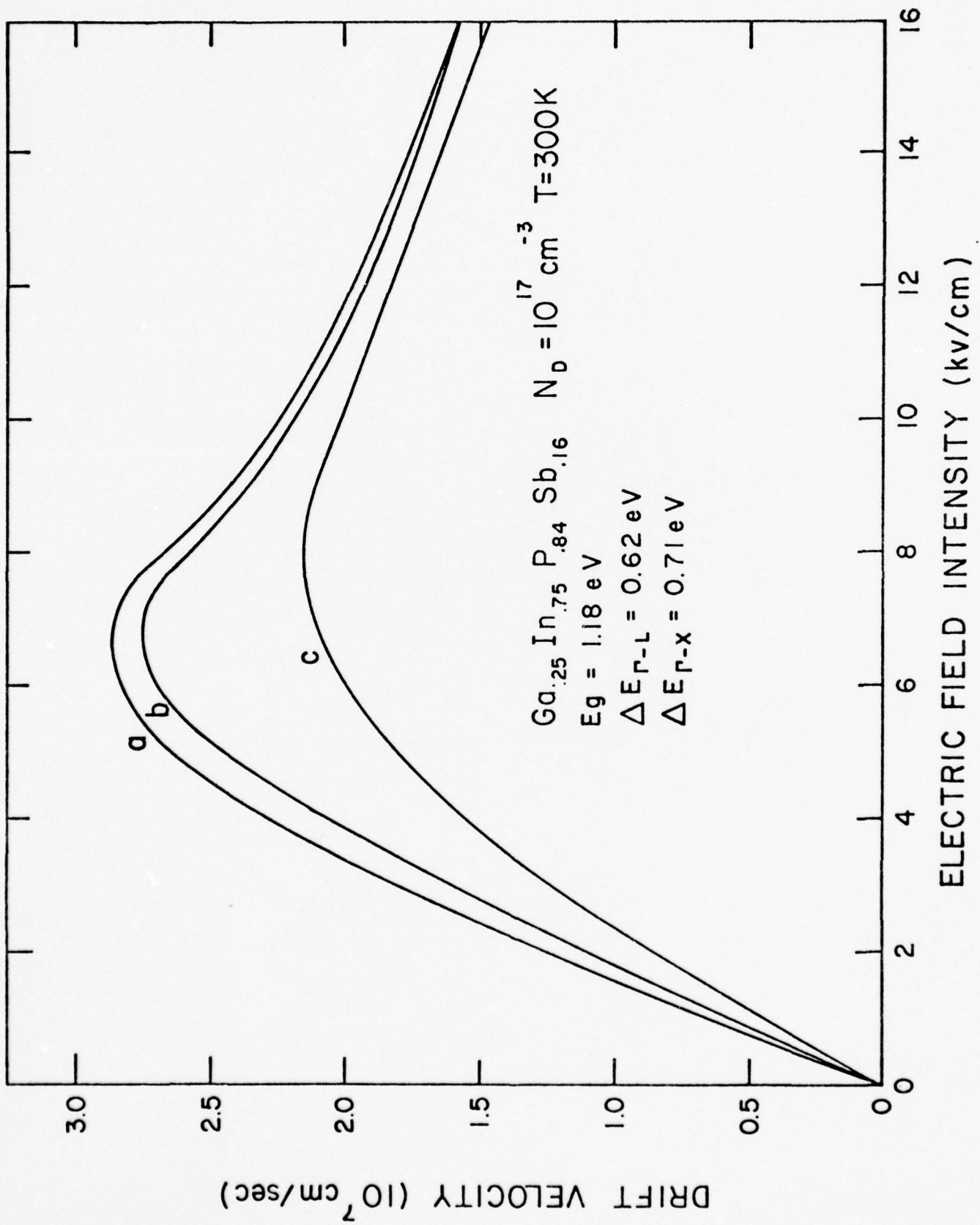


$I \Delta U_{\text{GaAs}}$, Alloy Scattering Parameter (eV^2)









NEGATIVE RESISTANCE AND PEAK VELOCITY
IN THE CENTRAL (000) VALLEY OF III-V SEMICONDUCTORS*

J. R. Hauser, T. H. Glisson and M. A. Littlejohn
Electrical Engineering Department
N. C. State University
Raleigh, N. C. 27607

ABSTRACT

The negative resistance in III-V materials such as GaAs at large electric fields is generally recognized as arising from the transfer of electrons from the central (000) valley to higher lying minima in the conduction band. Monte Carlo transport studies show that the negative resistance effect is still present in III-V materials when the valley spacing is increased to large values (> 0.5 eV) and even present when the higher minima are eliminated entirely from the calculations. This negative resistance arises from basic transport properties of the central valley. Studies are presented of the basic negative resistance effect in the central valley of III-V materials as well as studies of $\text{Al}_{1-x}\text{In}_x\text{As}$ ($x \sim 0.75$) and $\text{Ga}_{1-x}\text{In}_x\text{As}$ ($x \sim 0.6$) which are two specific materials where the negative resistance effect is due predominantly to the central valley.

*This work was supported by a research grant from the Office of Naval Research, Arlington, VA.

NEGATIVE RESISTANCE AND PEAK VELOCITY
IN THE CENTRAL (000) VALLEY OF III-V SEMICONDUCTORS

I. Introduction

The negative resistance effect as first reported by Gunn [1,2] has been observed in most of the III-V binary and ternary compounds which are direct bandgap materials. The major factors determining the negative resistance characteristic are now thought to be fairly well understood, and a good summary has recently been given by Ridley [3]. A brief summary of the conventional understanding is useful in relationship to the present work.

The negative resistance effect in GaAs has been identified with a transfer of electrons at large electric fields from the high mobility Γ or central valley to higher lying L or X minima having lower mobilities. The validity of this basic model has been verified by simple analytical calculations [3-5] as well as by more detailed Monte Carlo calculations [6-11]. The energy bands for a general III-V semiconductor are shown in Figure 1, where ΔE is the energy separation between the central valley and the next lowest valley, which is assumed to be the L valley. In some materials a three band model including both the X and L minima is required to give good agreement between theory and experimental results.

In the presence of a large electric field, central valley electrons are heated by the field to large kinetic energies, and as the average kinetic energy approaches the valley separation, a large percentage of the electrons transfer to the upper valley. This transfer is enhanced by the larger effective mass of the upper valleys as compared with the central

valley. Ridley has used an energy balance approach to estimate the average energy of the electrons as a function of electric field and equated this average energy to the valley separation to estimate the threshold electric field for a variety of transferred electron materials [3].

Simple considerations of the transferred electron effect lead to the conclusion that high peak velocities should be achieved in materials with a) a large low field mobility and b) a large energy separation between the central valley and the higher lying minima. The binary semiconductor GaAs has a relatively small valley separation on the order of 0.31 eV. The separation for InP is somewhat larger at 0.60 eV and InP is predicted to have a larger peak velocity than GaAs although the field at which the peak velocity occurs is also somewhat larger.

The largest valley separation in the binary III-V materials is 1.11 eV in InAs. This large valley separation, however, cannot be used in TED devices because of the low breakdown voltages of InAs due to the small bandgap of 0.36 eV. Thus, of the binary III-V materials, InP is predicted to have the largest peak velocity of the materials which are useful for TEDs.

The ternary and quaternary III-V materials provide a wider range of bandgaps and valley separation for potentially higher peak velocities than can be achieved in the binary materials. The quaternary $\text{Ga}_{1-x}\text{In}_x\text{P}_{1-y}\text{As}_y$ lattice matched to InP substrates has recently been predicted to have a peak velocity larger than that of either GaAs or InP [12]. The large low field mobility needed for high velocities requires low bandgap materials with small effective masses. However, too low a bandgap, as in InAs, leads to low breakdown voltages. Thus a compromise must be found between these two requirements. From breakdown voltage and device considerations, the bandgap of high velocity materials for either TEDs or FETs should probably be around 1 eV or larger.

If a minimum bandgap of around 1 eV is selected then all the III-V ternary and quaternary materials can be searched to find which material has the largest valley separation. This material turns out to be $\text{Al}_{1-x}\text{In}_x\text{As}$ for which the energy band diagram vs. composition is shown in Figure 2. At a composition of $x=0.75$ the energy gap is about 0.91 eV while the Γ -to-L valley separation is about 1.12 eV. Monte Carlo calculations for this composition (to be discussed in the next section) lead to a low field mobility of about $11,700 \text{ cm}^2/\text{V}\cdot\text{sec}$ and this coupled with the large valley separation leads to an expected large peak velocity before the onset of a negative resistance effect.

Another ternary material which has a large valley separation and also has a large bandgap is $\text{Ga}_{1-x}\text{In}_x\text{As}$ with $x \sim 0.3-0.4$. For example at $x=0.4$ the bandgap is 0.86 eV and the valley separation is 0.72 eV. These values are not quite as good as those for the $\text{Al}_{1-x}\text{In}_x\text{As}$ system but the technology for $\text{Ga}_{1-x}\text{In}_x\text{As}$ is much more highly developed. The quaternary $\text{Ga}_{1-x}\text{In}_x\text{P}_{1-y}\text{As}_y$ previously reported on [12] also has a favorable bandgap and valley separation for large peak velocities.

Monte Carlo calculations on both the $\text{Al}_{1-x}\text{In}_x\text{As}$ and $\text{Ga}_{1-x}\text{In}_x\text{As}$ systems have not shown as large a peak velocity as initially expected. This has been found to be due to fundamental physical limitations for the peak velocity which occur within the central valley. For valley separations larger than about 0.5 eV, the peak velocity and the threshold field have been found to be determined almost entirely by the properties of the central valley. Materials with large valley separations will be referred to in this work as central valley dominated materials since such materials show a peak velocity and a negative resistance determined mainly by the central valley. The high field properties of such materials are discussed in detail in the next section.

II. Central Valley Dominated Materials

The calculated velocity field curve for $\text{Al}_{.25}\text{In}_{.75}\text{As}$ is shown in Figure 3. The material parameters used in the calculations were obtained from the binary III-V parameters as discussed in previous publications [10-12] and are given in Table I. Included in the calculations are scattering processes due to acoustic phonon, polar optical phonons, ionized impurity ($10^{16}/\text{cm}^3$ impurity density), piezoelectric, alloy scattering processes, and equivalent and nonequivalent intervalley processes. The calculated peak velocity is about 2.7×10^7 cm/sec at a field of about 4000 V/cm. This peak value is about 35% higher than the calculated and measured values for GaAs and this verifies to some extent the discussion of the previous section as to the need for a large valley separation to achieve large peak velocities. However, the peak velocity is not as large as was expected before the calculations were performed.

The numerical values shown at various points along the curve of Figure 3 give the percentages of electrons in the L plus X minima. At the peak of the velocity curve it is seen that only 0.07% of the electrons have been transferred to the upper valleys. At 10^4 V/cm which is far into the negative resistance region only 9.2% of the electrons have been excited to the upper valley. These percentages which were obtained from the Monte Carlo calculations are much too low to account for the peak in velocity and the negative resistance for this material. For example at 10^4 V/cm a transfer of all electrons back to the central valley would increase the velocity by no more than 10% and this is much too small an effect to eliminate the negative resistance. This leads to the conclusion that the peak velocity is being controlled by the central valley in this material and is not due to electron transfer to the upper valley.

The dominance of the central valley in determining the peak velocity is shown in Figure 4 which compares the calculated velocity-field relationship of Figure 3 with that obtained by including only the central valley in the Monte Carlo calculations. The two calculations give very similar velocity-field relationships with the peak velocity being unchanged by the elimination of scattering to the upper valleys. The solid curve gives an inherent negative resistance phenomena which has not previously been recognized to occur for III-V materials within the central valley alone. A comparison of the two curves in Figure 4 shows that transfers to the upper valleys increase the magnitude of the negative resistance beyond the peak but the upper valleys are not required for the existence of the negative resistance. Upper valley transfers are also seen to cause a larger drift velocity at very large fields (at 10^5 V/cm for example).

The dominance of the central valley is not limited to just $\text{Al}_{1-x}\text{In}_x\text{As}$ but has also been seen in other ternary materials such as $\text{Ga}_{1-x}\text{In}_x\text{As}$ with $x \sim 0.4 - 0.6$. The velocity field curve for this ternary with $x=0.6$ is shown in Figure 5. This particular material has an energy gap of 0.65 eV and a valley separation of 0.90 eV. As with the $\text{Al}_{.25}\text{In}_{.75}\text{As}$ case, the presence of the upper valleys has essentially no effect on the peak velocity or threshold field for negative resistance. The upper valleys again increase the negative resistance effect and increase the high field velocity.

The two materials discussed so far have large valley separations, and this is the condition for the peak velocity and threshold field being determined by the central valley. For lower valley separations, however, such as the 0.31 eV for GaAs the question arises as to how

important is the intervalley transfer of electrons in determining the peak velocity. Calculations for GaAs have shown that without the L and X valleys present the velocity would peak at about 2.5×10^7 cm/sec as opposed to the value of about 2.0×10^7 cm/sec including the upper valleys. Thus the transfer of carriers to the upper valleys reduces the peak velocity in GaAs by about 20%. A somewhat similar central valley dominance of the velocity field relationship has been seen in Monte Carlo calculations on CdTe [13]. This material also has a large valley separation similar to that of the III-V materials discussed above.

The central valley dominated materials such as shown in Figure 4 are predicted by the Monte Carlo calculations to have a large peak-to-valley ratio for the velocity-field curve. The peak-to-valley ratio in Figure 4 ranges from about 4 to 7 for peak fields from 20 kV to 100 kV. For GaAs with a smaller valley spacing, the peak-to-valley ratio is at most about 2.5 by both experimental measurement [14] and theoretical calculations [15]. This large peak-to-valley ratio for the central valley dominated semiconductors may be especially useful in certain device applications.

The preceding discussion has demonstrated that when the valley spacing becomes large the peak velocity and threshold field are no longer determined by electron transfer from the central valley to higher lying minima. The peak velocity is rather determined by the fundamental transport properties of the central valley. In order to understand these central valley limitations a study has been made of the high field properties of model semiconductors with only a central valley. These studies are discussed in detail in the next section.

III. Transport in Central Valley Only

This section considers a semiconductor in which the spacing between the central valley [$\Gamma(000)$ valley] and higher lying minima (either X or L valley) is so large that only the central valley must be considered in the transport. In all of the III-V ternary and quaternary materials the spacing can never be made so large that it has no effect on the transport process. However, as the previous section illustrates the spacing can be so large that intervalley transfers have a negligible effect on the peak velocity and threshold field for certain materials. A study of transport in only the central valley can thus lead to an understanding of the physical processes leading to a peak velocity and negative resistance effect in these materials as well as provide an upper limit to the peak velocity for other materials. Since the $\text{Al}_{.25}\text{In}_{.75}\text{As}$ comes the closest of all the ternary III-V materials to being dominated by the central valley, the parameters for the calculations presented in this section using only the central valley have been selected as those of this material which are listed in Table I.

The negative resistance and peak velocity in the central valley have been found to be due to the fundamental properties of polar optical scattering in this valley. This is shown in Figure 6 which shows the calculated velocity-field curve (solid curve) for only polar optical scattering in the central valley. The dotted curve shows the velocity-field curve when all central valley scattering processes are included. Polar optical scattering alone is seen to determine the general shape of the curves with the other scattering processes simply reducing the velocity

by almost a constant factor at all field values. This dominance of polar optical scattering is to be expected since it is the major energy loss process.

The central valley negative resistance for only polar optical scattering can be understood with fairly simple models. In steady state the use of energy balance and momentum balance expressions gives

$$qE\tau_m = m^*v, \quad (1)$$

$$qEv = \frac{\Delta\mathcal{E}(P_e - P_a)}{\tau_e}, \quad (2)$$

where m^* is the effective mass, v is the average drift velocity, τ_m is the momentum relaxation time, τ_e is the energy relaxation time, $\Delta\mathcal{E} = \hbar\omega_{\ell_0}$ is the energy lost or gained in a polar optical scattering event, P_e is the probability of phonon emission and P_a is the probability of phonon absorption. At large energies

$$P_e - P_a \rightarrow \left(\frac{e^x - 1}{e^x + 1} \right) = \tanh(x/2), \quad (3)$$

where $x = \hbar\omega_{\ell_0}/kT$. Solving both Equations (1) and (2) for the velocity gives

$$v = \frac{q\tau_m}{m^*} E, \quad (4)$$

$$v = \frac{\hbar\omega_{\ell_0} \tanh(\hbar\omega_{\ell_0}/2kT)}{q\tau_e} \frac{1}{E} \quad (5)$$

If τ_m is independent of field then Equation (4) predicts a linearly increasing velocity with field such as is observed in Figure 6 in the positive resistance region. If τ_e is constant or varies slowly with field then this equation predicts a decreasing velocity with field such as observed in Figure 6 in the negative resistance region.

The agreement between these two expressions and the Monte Carlo calculations is shown in Figure 7. The solid curve is the Monte Carlo results while the dotted curves show Equations (4) and (5) in the low field and high field regions. In using Equations (4) and (5) τ_m and τ_e have not been taken as constant but the curve of τ shown in Figure 7 has been used in the calculations. This τ was obtained from the Monte Carlo calculations and is the mean time between polar optical scatterings^a. Simple analytical expressions for τ_m or τ_e as a function of field are not easily derived so the results of the Monte Carlo calculations were used to verify Equations (4) and (5).

The good agreement of the Monte Carlo calculations with Equations (4) and (5) in the limiting regions shows that at low fields the velocity is primarily determined by momentum balance considerations while at high fields in the negative resistance region the velocity is determined by energy balance considerations. With optical phonon processes there is a fixed energy loss per scattering event and the drift velocity must decrease with field or too much energy will be gained from the field to be lost in the scattering events.

An estimation of the peak velocity which can be achieved by carriers in the central valley can be obtained by equating the limiting expressions as given by Equations (4) and (5) and solving for $qE\tau/m^*$. This gives for the peak velocity

a. The use of the same τ for both τ_m and τ_e will be approximately valid as long as only polar optical scattering is important. When other scattering events are present τ_m and τ_e will be significantly different.

$$v_p \leq v_{\max} = \left[\frac{\hbar\omega_{\ell_0}}{m^*} \tanh(\hbar\omega_{\ell_0}/2kT) \right]^{1/2}. \quad (6)$$

Values of v_{\max} for several binary and compound materials are shown in Figure 8. Also shown for several materials are the peak velocity values which result from Monte Carlo calculations including all bands and all scattering processes. For the binary materials GaAs, InP and InAs the Monte Carlo results give peak velocities which are about 82%-90% of the values predicted by Equation (6). For the two ternary and one quaternary materials shown, the Monte Carlo results differ from Equation (6) by large amounts. The lower Monte Carlo results for the ternary and quaternary materials is due to the presence of alloy scattering in these materials which is not present in the binary materials. If alloy scattering had not been included all of the Monte Carlo results would have been around 80%-90% of the limiting value given by Equation (6).

Monte Carlo results are not shown for InSb and GaSb. The bandgap of InSb is too low for this material to be used near the peak velocity. For GaSb the presence of the L minima at only 0.09 eV above the Γ minima causes the negative resistance effect not to occur in this material. The data in Figure 6 indicates that there is a general trend toward larger peak velocities as the bandgap of the semiconductor decreases.

In addition to the fundamental role of polar optical scattering in the central valley, the band nonparabolicity also has an influence on the peak velocity which can be achieved. Figure 9 shows the velocity field curves for the central valley only of $\text{Al}_{.25}\text{In}_{.75}\text{As}$ with different α values where

$$\frac{\hbar^2 k^2}{2m^*} = \mathcal{E}(1 + \alpha\mathcal{E}) = \gamma(\mathcal{E}). \quad (7)$$

The theoretical value of α is

$$\alpha = \frac{1}{\mathcal{E}_g} \left(1 - \frac{m^*}{m_0}\right)^2, \quad (8)$$

and for $\text{Al}_{.25}\text{In}_{.75}\text{As}$ the value is 1.04 eV^{-1} corresponding to one of the curves in Figure 9. Also shown are velocity field curves for α values an order of magnitude smaller and an order of magnitude larger than the theoretical value. For values of α less than 0.1 the calculated values are close to the 0.104 curve of Figure 9. At the theoretical value of α the nonparabolicity is seen to reduce the low field mobility by about 37%, to reduce the peak velocity slightly, and to increase the threshold field from around 3 KV/cm to around 4 KV/cm. A very large nonparabolicity ($\alpha=10.4 \text{ eV}^{-1}$), which fortunately does not occur in the III-V materials, is seen to very drastically reduce the low field mobility and the peak velocity. The nonparabolicity will be most important in materials with narrow bandgaps and large valley spacings, since α is large for such materials and the carriers become heated to large energies before inter-valley transfer occurs.

IV. Summary and Conclusions

The presently accepted theory of negative resistance effects in III-V semiconductors attributes the effect to the transfer of electrons from a high mobility central (Γ) valley to lower mobility, higher lying energy valleys (L or X). The present work has shown that in materials with a large valley spacing the negative resistance becomes dominated by the central valley. Monte Carlo calculations have shown that the presence of the upper valleys is not required for a negative resistance effect but that polar optical scattering acting in the central valley alone gives rise to a peak velocity and negative resistance effect. For materials with valley spacings of 0.5 eV or larger the peak velocity and threshold field has been found to be determined almost entirely by the central valley negative resistance effect. Transfers to the upper valleys influence mainly the magnitude of the negative resistance and the carrier velocity near the valley minimum of the velocity field curve.

Materials which have large valley spacings and are dominated by the central valley have large peak-to-valley velocity ratios as predicted by Monte Carlo calculations. The ternary materials $\text{Al}_{1-x}\text{In}_x\text{As}$ ($x \sim 0.75$), $\text{Ga}_{1-x}\text{In}_x\text{As}$ ($x \sim 0.5$) and the quaternary $\text{Ga}_{1-x}\text{In}_x\text{P}_{1-y}\text{As}_y$ ($x \sim 0.75$, $y \sim 0.4$) are typical of central valley dominated materials. The largest peak velocities which have so far been calculated by the Monte Carlo technique have been found in these materials.

Acknowledgments

The assistance of K. Williams and J. Shade in the calculations reported in this work are gratefully acknowledged.

Table 1. Al_{0.25}In_{0.75}As Material Parameters Used in the Calculations

A. Bulk Material Parameters

Parameter	Value	Parameter	Value
Lattice Constant	5.959×10^{-8} cm	LO Phonon energy	0.03605 eV
Density	5.27 gm/cm ³	Sound velocity	5.11×10^5 cm/sec
Electron Affinity Diff.	1.32 eV	Optical Dielectric Constant	10.78
Piezoelectric Constant	.056 coulomb/m ²	Static Dielectric Constant	13.46

B. Valley-Dependent Material Parameters

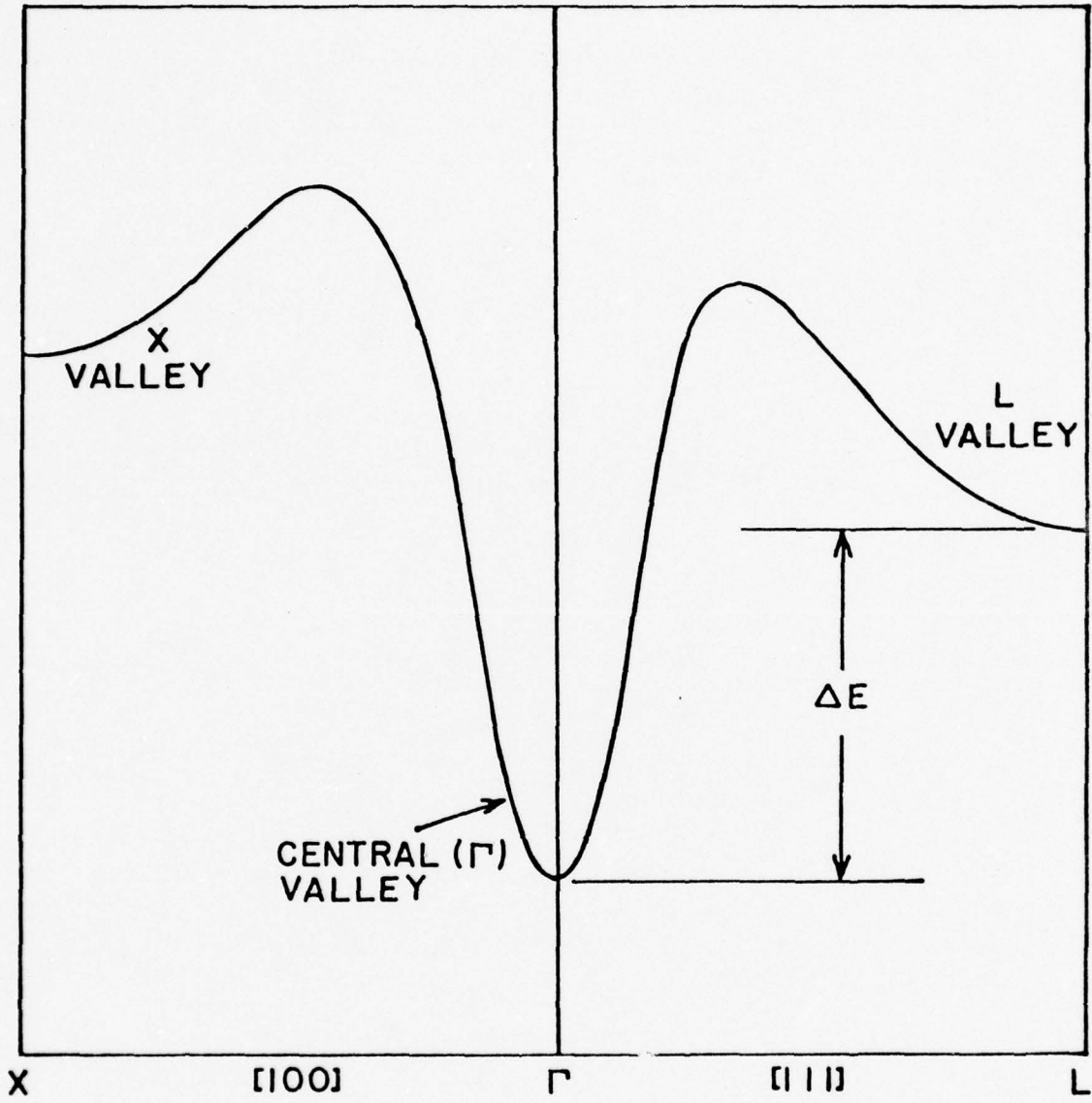
Parameter	Conduction Band Valley		
	$\Gamma(000)$	X(100)	L(111)
Acoustic Deformation Potential (eV)	6.73	9.35	8.83
Effective Mass (m^*/m_0)	0.028	0.62	0.34
Non-Parabolicity (eV^{-1})	1.04	0.204	0.814
Energy Band Gap (eV) (relative to valence band)	0.909	2.113	2.025
Optical Deformation Potential (eV/cm)	0	0	3×10^8
Optical Phonon Energy (eV)	-	-	0.0336
Intervalley Deformation Potential (eV/cm)			
From $\Gamma(000)$	0	6.25×10^8	5×10^8
From X(100)	6.25×10^8	6.25×10^8	5×10^8
From L(111)	5×10^8	5×10^8	5×10^8
Intervalley Phonon Energy (eV)			
From $\Gamma(000)$	0	0.0253	0.0262
From X(100)	0.0253	0.0253	0.0309
From L(111)	0.0262	0.0309	0.0254
Number of Equivalent Valleys	1	3	4

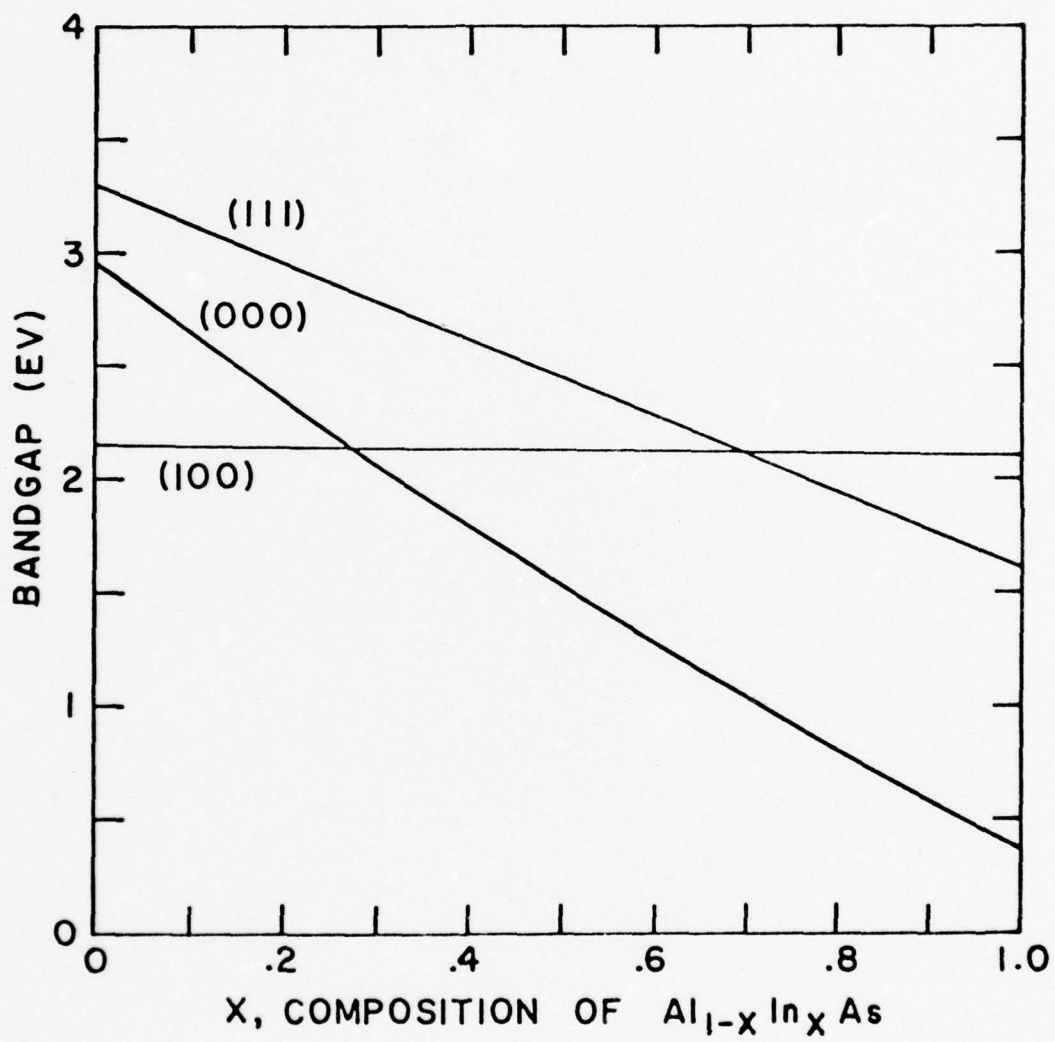
References

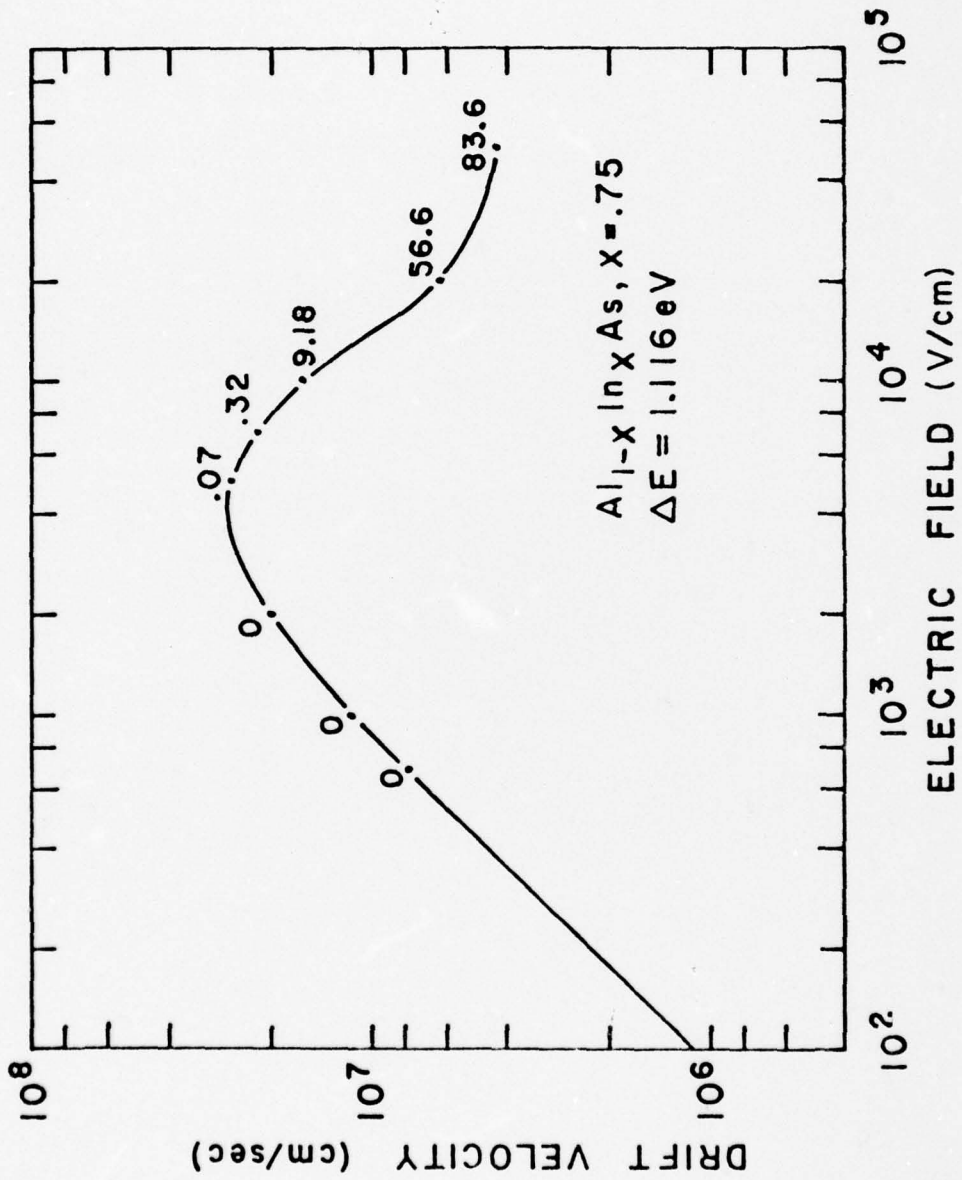
1. J. B. Gunn, *Solid-State Commun.* 1, 88 (1963).
2. J. B. Gunn, *IBM J. Res. Dev.* 8, 141 (1964).
3. B. K. Ridley, *J. Appl. Phys.* 48, 754 (1977).
4. B. K. Ridley and T. B. Watkins, *Proc. Phys. Soc. (Lond.)* 78, 293 (1961).
5. D. E. McCumber and A. G. Chynoweth, *IEEE Trans. on ED*, ED-13, 4 (1966).
6. T. Kurosawa, *Proc. Int. Conf. Semicond. Kyoto*, *J. Phys. Soc. Jpn. Suppl.* 21, 424 (1966).
7. W. Fawcett, A. D. Boardman and S. Swain, *J. Phys. Chem. Solids* 31, 1963 (1970).
8. J. G. Ruch and W. Fawcett, *J. Appl. Phys.* 41, 3843 (1970).
9. W. Fawcett and D. C. Herbert, *J. Phys. C* 7, 1641 (1974).
10. M. A. Littlejohn, J. R. Hauser and T. H. Glisson, *Appl. Phys. Lett.* 26, 625 (1975).
11. J. R. Hauser, M. A. Littlejohn and T. H. Glisson, *Appl. Phys. Lett.* 28, 458 (1976).
12. M. A. Littlejohn, J. R. Hauser and T. H. Glisson, *Appl. Phys. Lett.* 30, 242 (1977).
13. V. Borsari and C. Jacoboni, *Phys. Stat. Sol. (b)* 54, 649 (1972).
14. P. A. Houston and A. G. R. Evans, *Solid-State Elec.*, 20, 197 (1977).
15. M. A. Littlejohn, J. R. Hauser and T. H. Glisson, *Appl. Phys. Lett.*, accepted for publication.

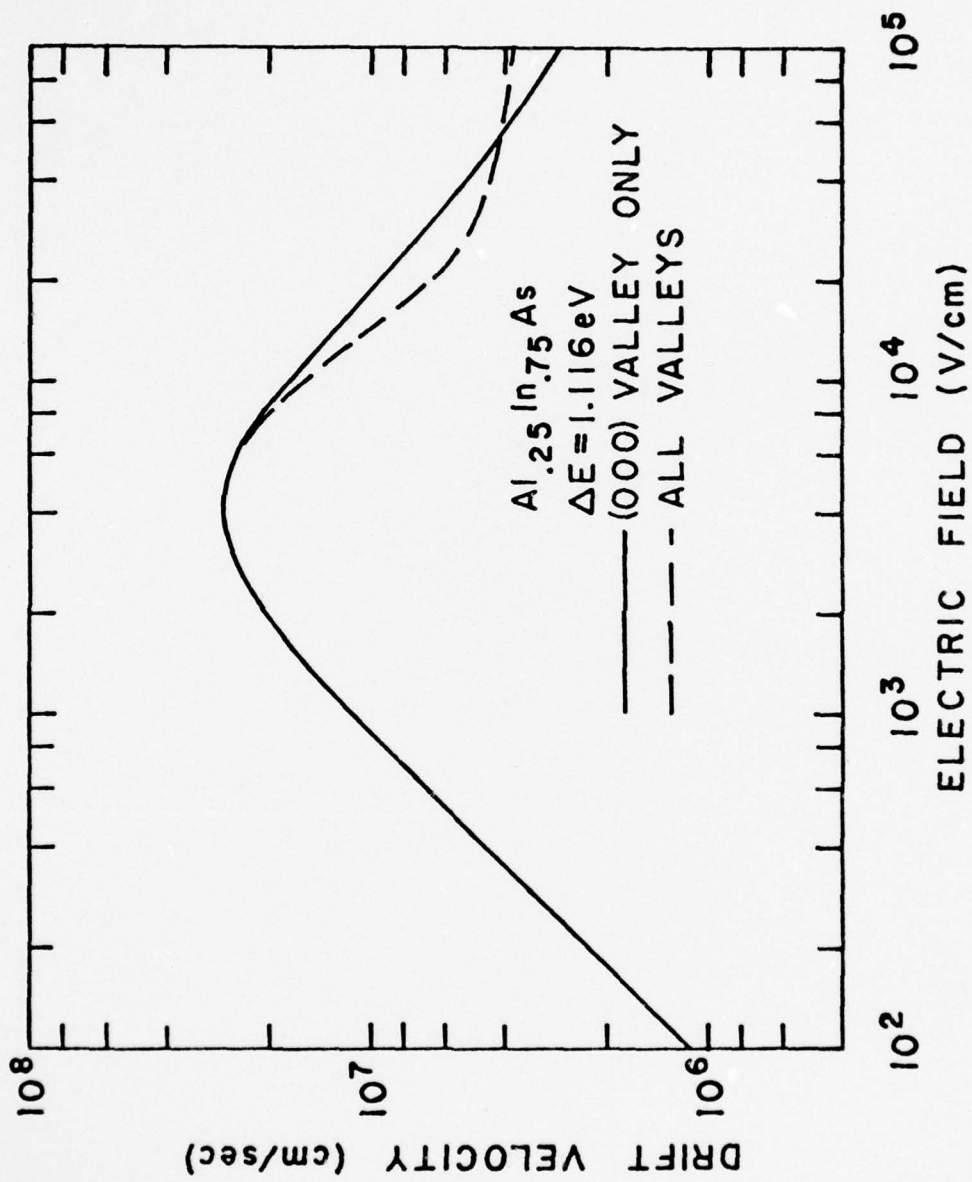
Figure Captions

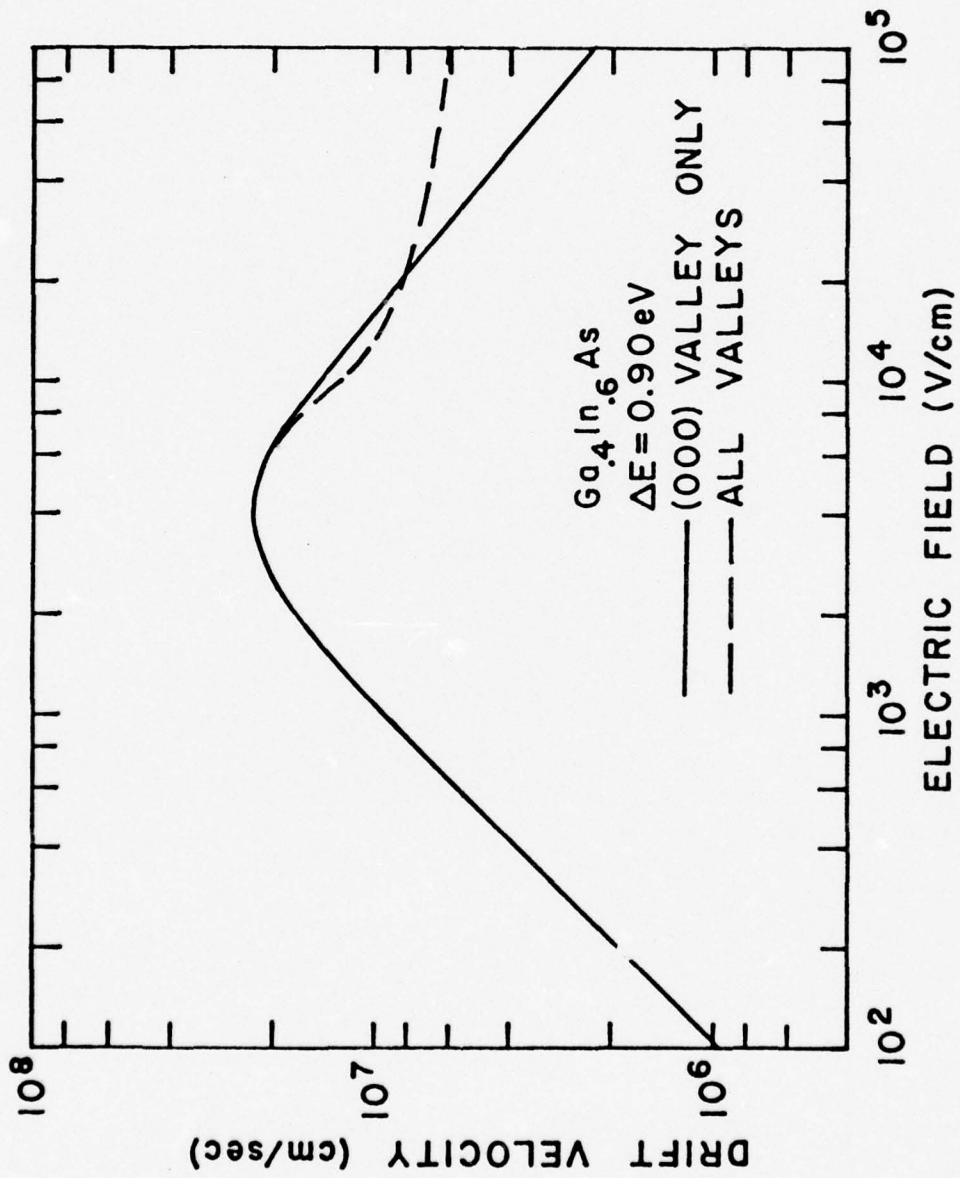
- Figure 1. Energy band diagram for general III-V direct bandgap semiconductor.
- Figure 2. Calculated energy gaps vs. composition for $\text{Al}_{1-x}\text{In}_x\text{As}$.
- Figure 3. Calculated velocity-field curve for $\text{Al}_{.25}\text{In}_{.75}\text{As}$. The values along the curve show the percentages of electrons in the upper (111 and 100) valleys.
- Figure 4. Comparison of velocity-field curves for $\text{Al}_{.25}\text{In}_{.75}\text{As}$ using central valley only and using all valleys.
- Figure 5. Velocity-field curves for $\text{Ga}_{.4}\text{In}_{.6}\text{As}$.
- Figure 6. Velocity-field curve for central valley with just polar optical scattering.
- Figure 7. Comparison of Monte Carlo calculations with simple momentum and energy balance expressions.
- Figure 8. Calculated upper limits to peak velocity considering central valley only.
- Figure 9. Velocity Field curves for $\text{Al}_{.25}\text{In}_{.75}\text{As}$ with different nonparabolicity factors. The theoretical value is $\alpha = 1.04 \text{ eV}^{-1}$.

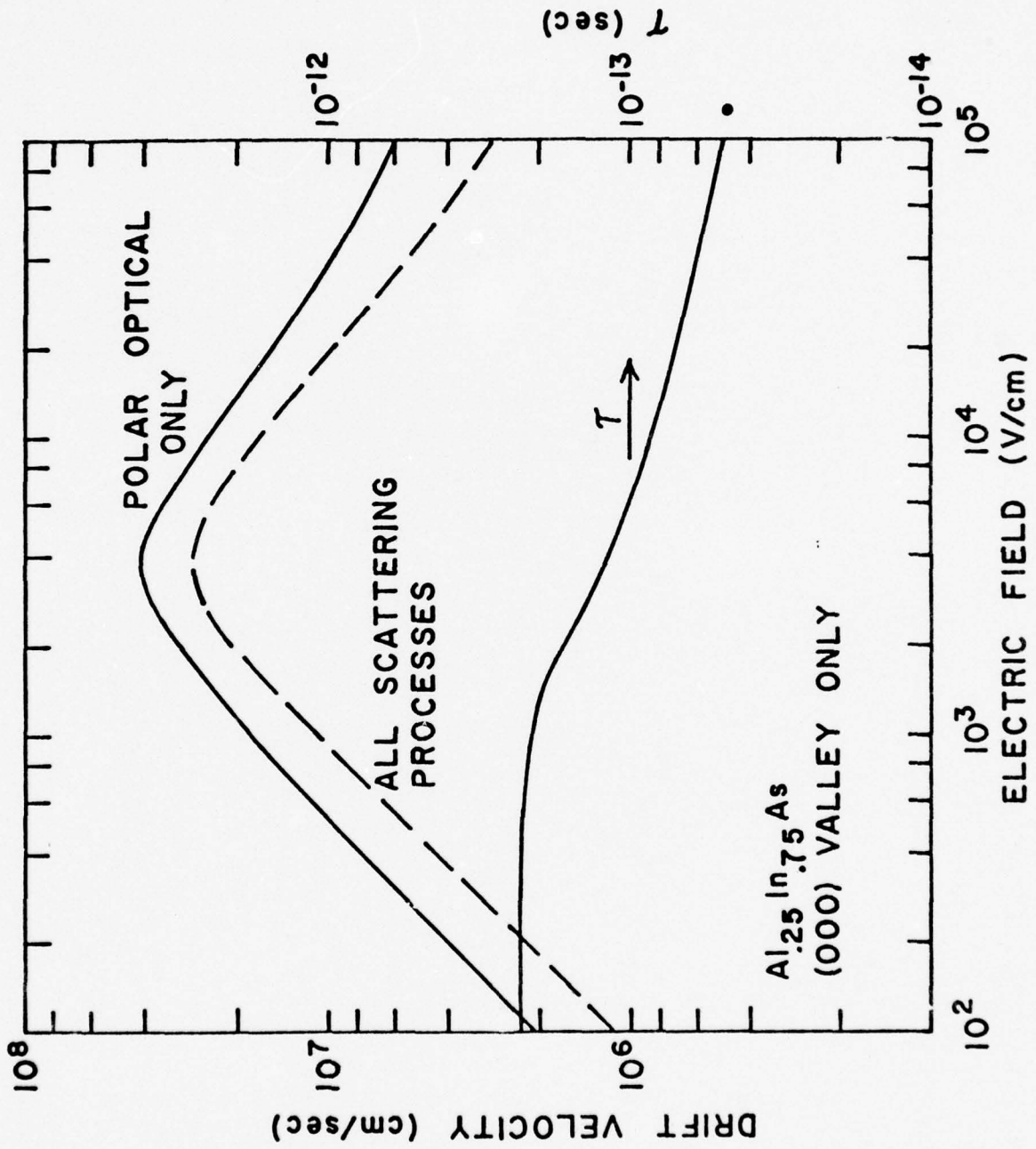


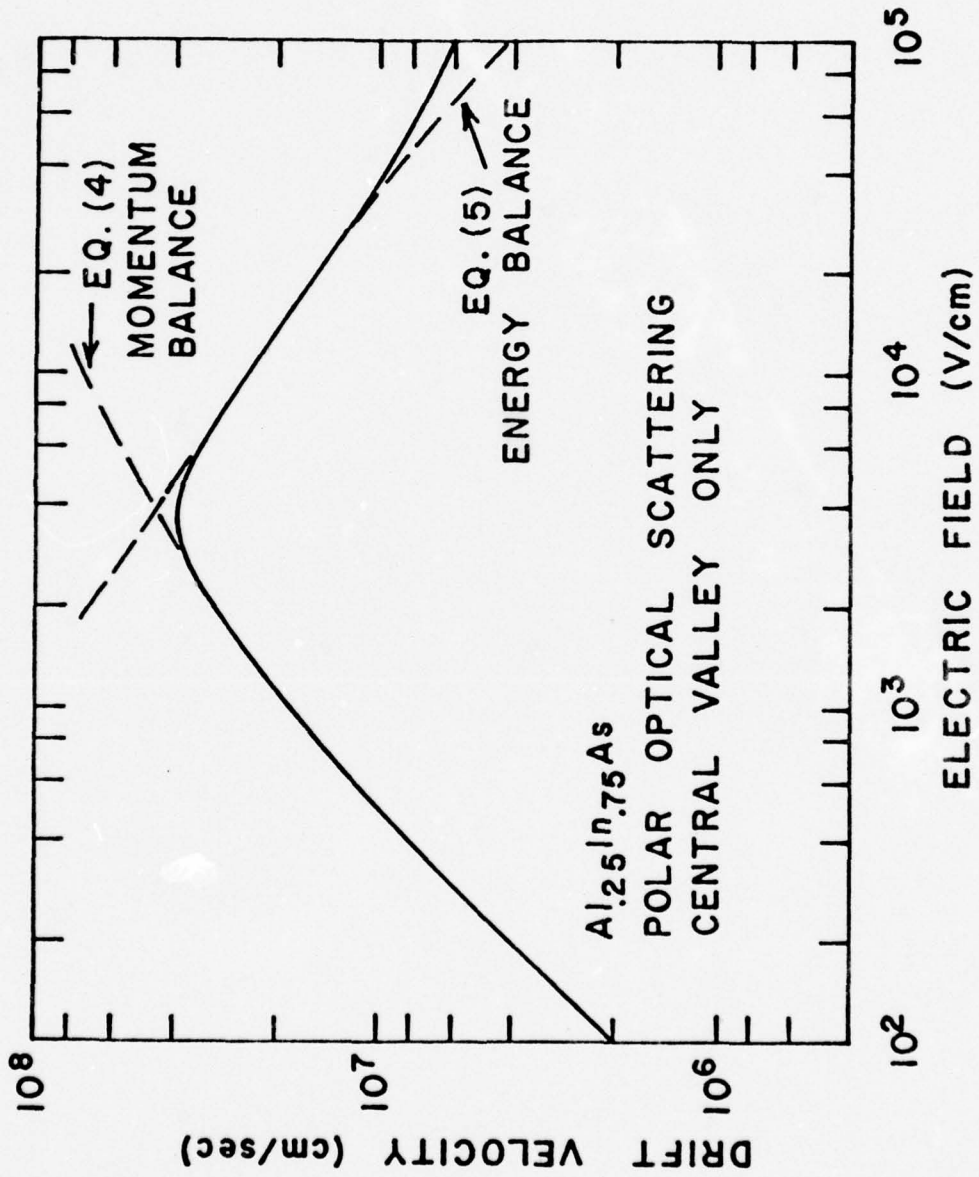


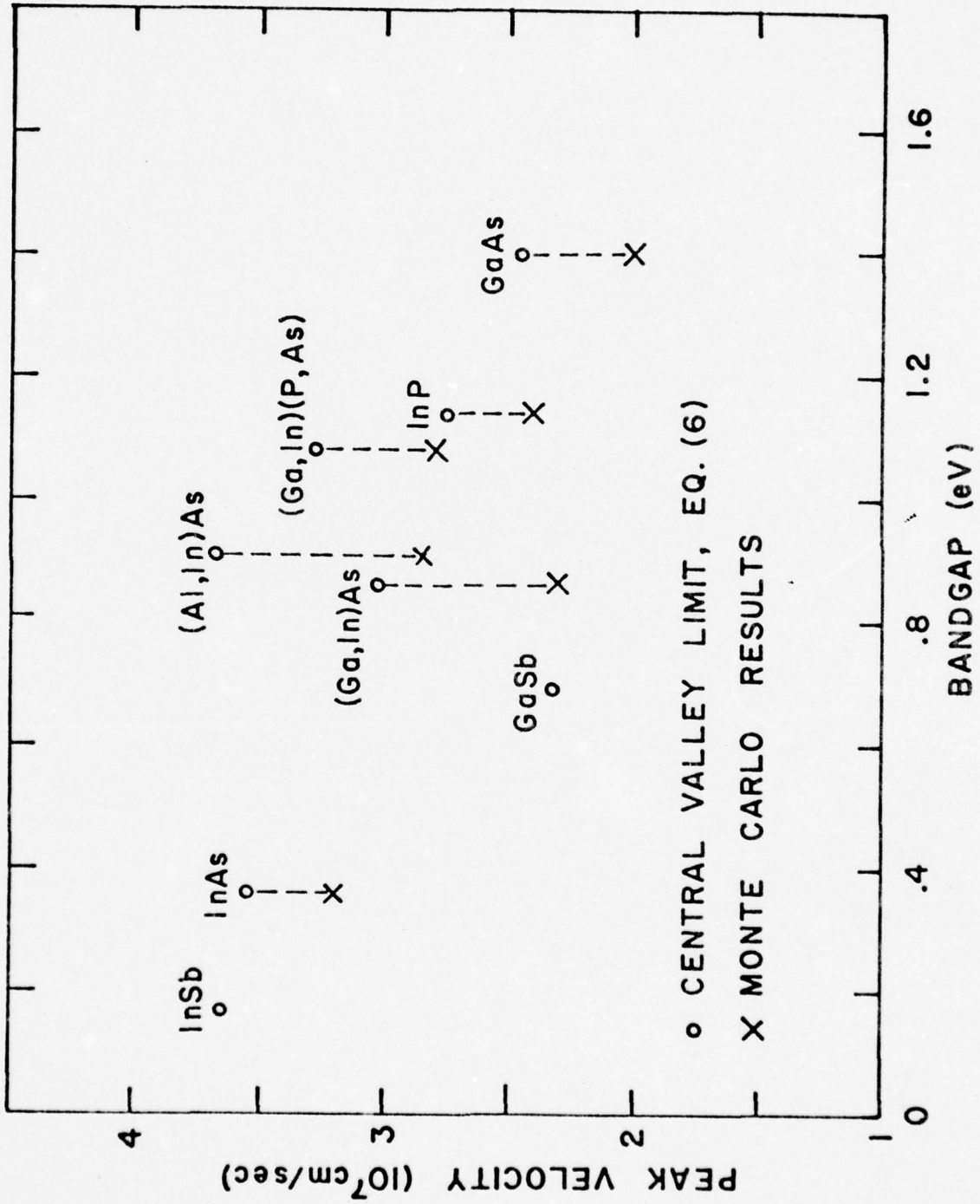


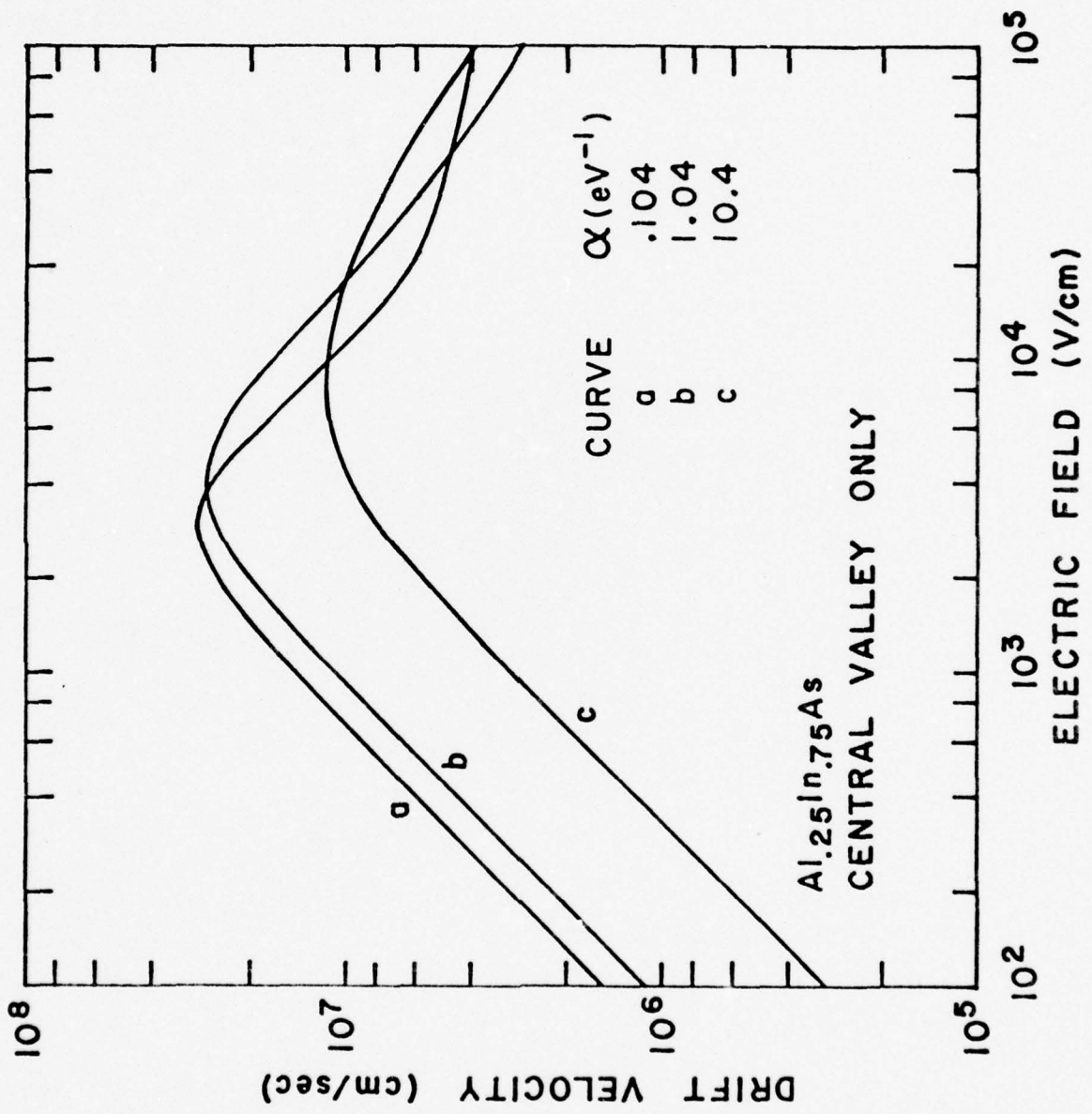












Velocity-field characteristics of $\text{Ga}_{1-x}\text{In}_x\text{P}_{1-y}\text{As}_y$ quaternary alloys*

M. A. Littlejohn, J. R. Hauser, and T. H. Glisson

Department of Electrical Engineering, North Carolina State University, Raleigh, North Carolina 27607
(Received 18 October 1976; in final form 27 December 1976)

The electron drift-velocity-electric-field relationship has been calculated for the $\text{Ga}_{1-x}\text{In}_x\text{P}_{1-y}\text{As}_y$ quaternary alloy using the Monte Carlo method. Emphasis has been placed on the compositional range for which the alloy is lattice matched to GaAs and InP. These calculations suggest that this quaternary offers promise as a material for microwave semiconductor devices, including field-effect transistors and transferred electron devices.

PACS numbers: 72.20.Fr, 85.30.De, 72.20.Dp, 85.30.Tv

Recent interest in the $\text{Ga}_{1-x}\text{In}_x\text{P}_{1-y}\text{As}_y$ quaternary alloy has centered around the applications of this material for optical devices, such as photoemission cathodes, double-heterojunction lasers, and light-emitting diodes.¹⁻⁵ One major advantage of the quaternary alloy system for these applications is that the material can be synthesized with a fixed lattice constant which is matched to a substrate over a wide energy band-gap range.⁶ This fact is also important in material considerations for microwave devices, such as the metal-epitaxial-semiconductor-field-effect transistor (MESFET) and transferred electron devices. The present study has been concerned with the electron drift-velocity-electric-field relationship in $\text{Ga}_{1-x}\text{In}_x\text{P}_{1-y}\text{As}_y$ quaternary alloys which can be lattice matched to either GaAs or InP. The results show, especially for lattice matching of the quaternary to InP, that substantial improvements in low field drift mobility and peak drift velocity can be obtained in comparison to GaAs, InP, and the $\text{Ga}_x\text{In}_{1-x}\text{As}$ ternary system, which are all important materials for microwave devices.

The computer simulation of transport processes used in obtaining the results presented here has been described in previous publications^{7,8} and is similar to other such programs discussed in the literature.⁹⁻¹¹ The allowed scattering mechanisms in the transport simulation include acoustic phonon scattering, optical phonon scattering, piezoelectric scattering, equivalent and nonequivalent intervalley scattering, ionized impurity scattering, and random potential alloy scattering.⁸ The program allows for calculations with any or all of these mechanisms in either the $\Gamma(000)$, $X(100)$, or $L(111)$ nonparabolic conduction bands.

The manner in which the material parameters for the quaternary alloy are calculated as a function of alloy composition (x, y) is as follows. First, the accepted values of binary material parameters for GaAs,⁹ InP,^{8,9} InAs,^{8,12} and GaP¹³⁻¹⁵ are used in theoretical models^{16,17} to calculate the material parameters for the four possible ternary combinations of these four binary materials. For some parameters, such as the equivalent and nonequivalent intervalley deformation potentials, such theoretical models do not exist, and in these

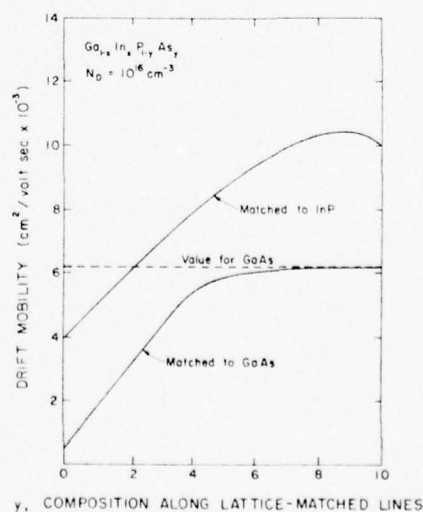


FIG. 1. Low-field mobility of $\text{Ga}_{1-x}\text{In}_x\text{P}_{1-y}\text{As}_y$ lattice matched to InP and GaAs. The quaternary doping level is 10^{16} cm^{-3} .

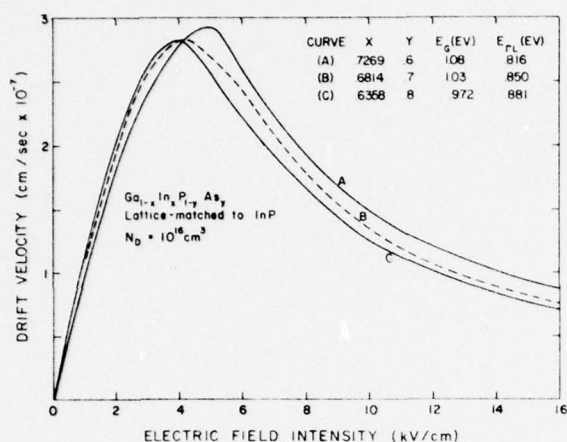


FIG. 2. Velocity-field characteristic of $\text{Ga}_{1-x}\text{In}_x\text{P}_{1-y}\text{As}_y$ lattice-matched to InP. The doping level is 10^{16} cm^{-3} .

cases linear interpolations are used for the ternary parameters.^{8,9} From the ternary material parameters, the following equation is used to calculate a given quaternary material parameter, Q , as a function of the quaternary alloy composition (x, y):

$$Q(x, y) = \{x(1-x)[(1-y)T_{12}(x) + yT_{43}(x)] + y(1-y) \times [(1-x)T_{14}(y) + xT_{23}(y)]\} [x(1-x) + y(1-y)]^{-1}, \quad (1)$$

where T_{ij} is the material parameter (such as band gap, deformation potential, etc.) for the ternary alloy of binary materials i and j . In this paper, GaP is material 1, InP is material 2, InAs material 3, and GaAs material 4. Thus $T_{12}(x)$ is a material parameter for $\text{Ga}_{1-x}\text{In}_x\text{P}$. Equation (1) is an empirical relation which reduces to the correct ternary expression (i.e., for x or y equal to either 0 or 1), and in the limit reduces to the correct expression for the binary materials. Also, for $x=y=0.5$ Eq. (1) reduces to the average of the four ternary alloy parameters. For other x and y values a smooth curve is generated which correctly matches the ternary boundary parameters. This empirical procedure for choosing the quaternary material parameters is similar to that used by Moon *et al.*⁶ for lattice constant and energy band gap.

Microwave device technology, such as that for the MESFET, usually requires thin epitaxial layers grown on a suitable substrate.¹⁸ The work discussed here is

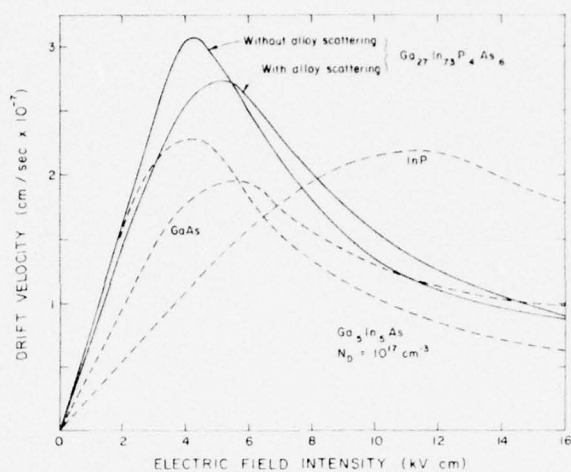


FIG. 3. Velocity-field characteristic of $\text{Ga}_{0.27}\text{In}_{0.73}\text{P}_{0.4}\text{As}_{0.6}$ with and without random potential alloy scattering. Shown for comparison are the velocity-field curves for GaAs, InP, and $\text{Ga}_{0.5}\text{In}_{0.5}\text{As}$. The doping level is 10^{17} cm^{-3} .

limited to the quaternary alloys which are lattice matched to either GaAs or InP, since these materials are presently the most popular binary III-V materials used for substrates in microwave applications. The values of x and y required for lattice matching to InP (lattice constant = 5.869 Å) and GaAs (lattice constant = 5.642 Å) can be found in Fig. 1 of Ref. 6. This figure has been reproduced in this work using Eq. (1). These values of x and y for lattice matching are given to a good approximation by the linear equations

$$\begin{aligned} y &\approx 2.197(1-x), & \text{matching to InP} \\ y &\approx 1 - 2.179x, & \text{matching to GaAs.} \end{aligned} \quad (2)$$

Figure 1 shows the calculated values of the low-field (100 V/cm) drift mobility for the $\text{Ga}_{1-x}\text{In}_x\text{P}_{1-y}\text{As}_y$ quaternary alloys with a doping level of 10^{16} cm^{-3} which are lattice matched to GaAs and InP. These mobility values are obtained by a maximum likelihood estimation of diffusion coefficient, and by using the Einstein relation between diffusion coefficient and mobility.¹⁹ This method is similar to a recent technique developed by Canali *et al.*²⁰ to calculate low-field drift mobility, and has been found to overcome some of the problems inherent in the application of the Monte Carlo method at low electric fields.^{19,20} As can be seen in Fig. 1, the drift mobility of the alloy matched to InP lies well above

TABLE I. Comparison of material parameters for a doping level of 10^{17} cm^{-3} obtained from Monte Carlo calculations.

	GaAs	InP	$\text{Ga}_{0.5}\text{In}_{0.5}\text{As}$		$\text{Ga}_{0.27}\text{In}_{0.73}\text{P}_{0.4}\text{As}_{0.6}$	
			Alloy	No alloy	Alloy	No alloy
μ_D ($\text{cm}^2/\text{V sec}$ at 100 V/cm) ^a	4600	3100	7900	9700	7000	7800
V_{max} (cm/sec) ^b	2.0×10^7	2.3×10^7	2.3×10^7	2.8×10^7	2.8×10^7	3.1×10^7
E_{max} (kV/cm) ^c	5.2	11.5	4.2	3.7	5.0	4.0
Peak-to-valley ratio (valley at 16 kV/cm)	2.1	1.3	3.6	4.0	3.1	3.6
$ \mu_{\text{ND}} $ ($\text{cm}^2/\text{V sec}$) ^d	2300	1100	3200	4800	3600	3700

^a μ_D = drift mobility at 100 V/cm.

^b V_{max} = maximum drift velocity.

^c E_{max} = electric field for $V = V_{\text{max}}$.

^d $|\mu_{\text{ND}}|$ = magnitude of maximum negative differential mobility.

the value for GaAs for $y > 0.30$ ($x < 0.86$). Since large values of electron drift mobility are desirable for MESFET's, this range of alloy composition looks especially attractive.

Velocity-field calculations have been made along both the GaAs and InP lattice-matched lines. For the GaAs substrate, the peak velocity for the quaternary was found to continually decrease from that for pure GaAs. For the InP substrate, the peak velocity was found to reach a maximum for quaternary alloy with $y \sim 0.6$.

Figure 2 shows the velocity-field relationships for the quaternary alloys matched to InP which have the largest calculated values of peak drift velocity. The value for $x=0.73$, $y=0.6$ of 2.95×10^7 cm/sec is the largest we have calculated for any material with a band gap and intervalley separation large enough to be useful for MESFET's. Also, it must be pointed out that the values presented in Fig. 2 assume a completely random alloy with no sublattice ordering,^{8,16,17} so that the amount of alloy scattering in the Monte Carlo simulation is maximum. If the material has some degree of ordering so that the amount of alloy scattering is reduced, the peak velocities could be larger by as much as 10–20%.

Figure 3 illustrates the influence of alloy scattering on the velocity-field characteristics of the quaternary with $x=0.73$, $y=0.6$, and a doping level of 10^{17} cm⁻³. Alloy scattering in a random alloy can be seen to decrease the peak velocity and increase the threshold field. Also shown in this figure are the velocity-field relationships obtained by the Monte Carlo method for GaAs, InP, and the ternary Ga_{0.5}In_{0.5}As, which has been proposed as a promising material for MESFET's.^{19,21} Finally, Table I summarizes the material properties of interest for microwave devices for the Ga_{0.27}In_{0.73}P_{0.4}As_{0.6} quaternary alloy, with and without random potential alloy scattering, along with the properties for GaAs, InP, and Ga_{0.5}In_{0.5}As. The ternary Ga_{0.5}In_{0.5}As can also be approximately lattice matched to InP and has a band gap of 0.89 eV.

In summary, this work indicates that the Ga_{1-x}In_xP_{1-y}As_y quaternary alloy should have desirable material properties for microwave devices. The calculated peak velocity for the quaternary system lattice matched to InP is larger than the calculated value for

the binary or ternary III-V materials. Also the quaternaries have a large negative mobility and a large peak-to-valley ratio, which should be useful in transferred electron devices. The work points out a need for experimental verification of the results, as well as pointing out the need for experimental studies of ordering in ternary and quaternary alloys, since the actual amount of ordering in these materials will determine which will be most useful for specific applications.

*Work supported by a research grant from the Office of Naval Research, Washington, D.C.

¹J.S. Eteher, G.A. Antypas, and J. Edgecombe, Appl. Phys. Lett. 29, 153 (1976).

²J.J. Coleman, N. Holonyak, M.J. Ludowisc, P.D. Wright, W.O. Groves, and D.L. Kuene, Appl. Phys. Lett. 29, 167 (1976).

³P.D. Wright, J.J. Coleman, N. Holonyak, M.J. Ludowisc, and G.E. Stillman, Appl. Phys. Lett. 29, 18 (1976).

⁴J.J. Hsieh, J.A. Rossi, and J.P. Donnelly, Appl. Phys. Lett. 28, 709 (1976).

⁵T.P. Pearsall, B.I. Miller, R.J. Clark, K.J. Bachmann, Appl. Phys. Lett. 28, 499 (1976).

⁶R.L. Moon, G.A. Antypas, and L.W. James, J. Electron. Mater. 3, 635 (1974).

⁷M.A. Littlejohn, J.R. Hauser, and T.H. Glisson, Appl. Phys. Lett. 26, 625 (1975).

⁸J.R. Hauser, M.A. Littlejohn, and T.H. Glisson, Appl. Phys. Lett. 28, 458 (1976).

⁹W. Fawcett and D.C. Herbert, J. Phys. C 7, 1641 (1974).

¹⁰W. Fawcett, A.D. Boardman, and S. Swain, J. Phys. Chem. Solids 31, 1963 (1970).

¹¹T. Kurosawa, Proc. Int. Conf. Phys. Semicond., Kyoto, 1966 (unpublished); J. Phys. Soc. Jpn. Suppl. 21, 424 (1966).

¹²D. Matz, Phys. Rev. 168, 843 (1968).

¹³K. Fletcher and P.N. Butcher, J. Phys. C 6, 976 (1973).

¹⁴D.L. Rode, Phys. Status Solidi B 53, 245 (1972).

¹⁵D.K. Ferry, Phys. Rev. B 12, 2361 (1975).

¹⁶J.W. Harrison and J.R. Hauser, J. Appl. Phys. 47, 292 (1976).

¹⁷J.W. Harrison and J.R. Hauser, Phys. Rev. B 13, 5347 (1976).

¹⁸J.S. Barrera and R.J. Archer, IEEE Trans. Electron Devices ED-22, 1023 (1975).

¹⁹M.A. Littlejohn, J.R. Hauser, and T.H. Glisson (unpublished).

²⁰C. Canali, C. Jacobini, F. Nava, G. Ottaviani, and A. Alberigi-Quaranta, Phys. Rev. B 12, 2265 (1975).

²¹D.R. Decker, R.D. Fairman, and C.K. Mishimoto, Proceedings 5th Biennial Cornell Elec. Engr. Conf., Cornell Univ., 1975, p. 305 (unpublished).

Reprinted from ANALYTICAL CHEMISTRY, Vol. 49, Page 1536, September 1977
Copyright 1977 by the American Chemical Society and reprinted by permission of the copyright owner

Qualitative Analysis of Thin Gallium Nitride Films with Secondary Ion Mass Spectrometry

J. Edward Andrews,¹ A. P. Duhamel,² and Michael A. Littlejohn

Department of Electrical Engineering, North Carolina State University, Raleigh, North Carolina 27607

Gallium nitride (GaN) thin films grown from the vapor phase by pyrolyzing $\text{Ga}(\text{C}_2\text{H}_5)_3 \cdot \text{NH}_3$, were analyzed using Secondary Ion Mass Spectrometry (SIMS). Comparative mass spectra were obtained from GaN grown by two other laboratories using two different techniques and were found to be similar. The SIMS technique identified the presence of Ga, N, and O, in all the GaN films. C was detected in the GaN film prepared by pyrolysis. Evidence of H as part of the ionic structure was in the higher mass spectra of all the samples; however, it could not be determined with certainty if the source of H originated in the SIMS instrument, the samples, or both.

Thin gallium nitride (GaN) films grown on $\alpha\text{-Al}_2\text{O}_3$ substrates by pyrolytic decomposition of $\text{Ga}(\text{C}_2\text{H}_5)_3 \cdot \text{NH}_3$ in a chemical vapor deposition system have been described in an earlier publication (1). The as-grown films were typically yellowish brown in color instead of transparent as would be expected for a material with a 3.5-eV energy band gap (2). This yellowish color was characteristic of the films grown

throughout the temperature range from 500 to 1000 °C. Since this was the first time that this growth process and system had been used to grow GaN, it was not at all certain that the deposits obtained were GaN, especially in view of the coloring noted above. Therefore effort during the early part of the research was directed toward obtaining a qualitative analysis of the deposits. Several analytical techniques were eventually used (electron microprobe, x-ray diffraction, electron diffraction, secondary ion mass spectrometry) with each providing some useful but not complete information concerning the nature of the deposits. The analytical technique reported here is worthy of note because of its ability to detect nitrogen as well as the lighter elements, including hydrogen, and was particularly valuable in analyzing deposits that were too amorphous to give useful diffraction data.

This paper reports the results of the qualitative analysis of the GaN thin films using the technique of Secondary Ion Mass Spectrometry (SIMS). The combination of sputter etching and mass spectrometry used in the SIMS technique permits a convenient and rapid qualitative analysis of thin films and surfaces. In depth discussions of the SIMS technique and available instrumentation have recently been presented (3-5). A comparison of the performance of the SIMS technique with Auger Electron Spectroscopy (AES) and x-ray photoelectron spectroscopy (XPS) given in Ref. 6 in-

¹Present address, Research Triangle Institute, P.O. Box 12194, Research Triangle Park, N.C. 27709

²Present address, U.S. Energy Research and Development Administration, Washington, D.C. 20545

Table I. Experimental Conditions Used for Sample Analysis

- (1) Primary ion beam gas: argon^a
- (2) Argon gas pressure: 3×10^{-4} Torr
- (3) Accelerating voltage for argon ions: 6 KeV
- (4) Ion-beam current at sample surface: 150 μ A

^a Oxygen was substituted for argon and mass spectrum retaken on the GaAs sample after the various samples had been analyzed.

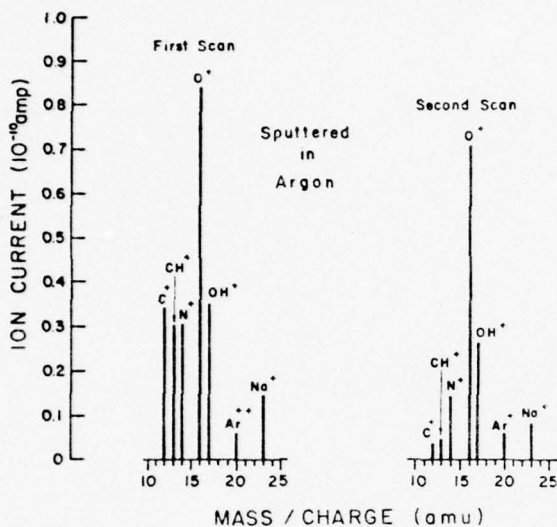


Figure 1. Two consecutive mass scans of sample 55S

indicates that the SIMS technique is capable of a much lower detection threshold.

For purposes of comparison, GaN samples furnished by courtesy of IBM and RCA were also analyzed. The IBM GaN was prepared by sputtering Ga in the presence of N₂ (7, 8). The RCA GaN was prepared by the ammonolysis of GaCl (9).

EXPERIMENTAL

The analysis of the GaN films (plus a sample of single crystal undoped GaAs) was performed using an Ion Beam Surface Mass Analyzer (ISMA). This instrument and its operation have been described in detail in (5). The analysis of the undoped GaAs was performed in order to eliminate possible background effects obtained from the instrument and to assist in the interpretation of the spectral data obtained from the GaN films.

The analysis of the GaN films and pure GaAs were performed under constant experimental conditions listed in Table I.

Sample chamber pressures prior to sample analysis were ordinarily of the order of 8×10^{-8} Torr. The mass resolution of the ISMA was typically 0.4 amu.

Mass spectra for the GaN and GaAs were obtained over the mass ranges 10-25, 62-77, and 80-95. Each range was scanned in a 2-min period at a rate of 0.125 amu/s with several scans performed consecutively to obtain data on the variation of various peak intensities as a function of time.

Species of potential interest in the mass ranges 10-25, 62-77, and 80-95 were ¹²C, ¹⁴N, ¹⁶O, ⁶⁹Ga, ⁷¹Ga, ⁶⁹Ga¹²C, ⁶⁹Ga¹⁴N, ⁶⁹Ga¹⁶O, ⁷¹Ga¹²C, ⁷¹Ga¹⁴N, and ⁷¹Ga¹⁶O, respectively.

RESULTS AND DISCUSSION

Figure 1 shows spectra resulting from the first two mass scans of GaN sample 55-S grown at 600 °C by the process described in Ref. 1. (The ordinate gives a measure of the ion beam current, in A, produced by the secondary ions sputtered from the surface of the sample.) Figure 1 indicates hydrocarbon fragments being detected only in the first few minutes of analysis. Normally, hydrocarbon fragments detected with this technique and exhibiting this behavior (disappearing after a few minutes of etching) are usually attributed to vacuum

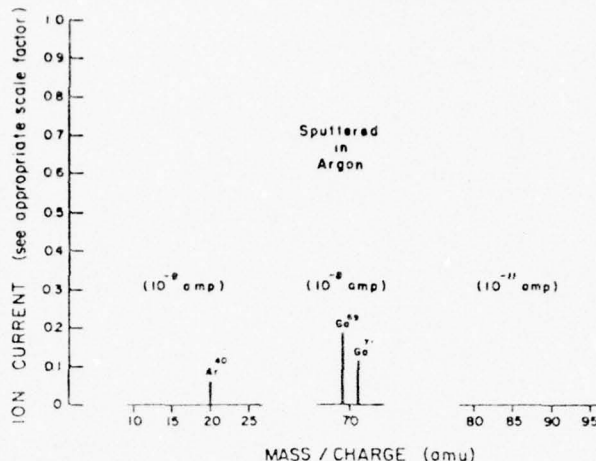


Figure 2. Mass spectrum of GaAs

system pump oil that has accumulated on the surface. However, GaAs spectra obtained under identical experimental conditions (see Figure 2) showed no indication of hydrocarbon fragments. This would strongly suggest that the hydrocarbon fragments observed in the GaN spectra were not an instrument artifact.

The sample 55-S mass peaks observed at 14 and 16 amu persisted with continued etching while those at 12 and 13 amu gradually disappeared. The peaks at 12, 13, and 16 amu were interpreted as [¹²C]⁺, [CH]⁺, and [¹⁶O]⁺, respectively.

The interpretation of the peak at 14 amu, however, is more complicated since it could be due to [CH₂]⁺, [¹⁴N] or both. The gradual disappearance of the [¹²C]⁺ and [CH]⁺ peaks suggests that the related [CH₂]⁺ peak should similarly disappear. Since the peak at 14 amu persisted, it could eventually be interpreted as being primarily [¹⁴N]⁺ as indicated in the second scan in Figure 1. The peak at 14 amu was seen to still be very evident in Figure 3 which is the spectrum after 8 to 10 min of etching. The absence of similar peaks in the GaAs spectra (Figure 2) indicates that background interferences were not responsible for the observed peaks in the GaN spectra.

It was noted (compare Figures 2 and 3) incidentally that the Ga ion yield for sample 55S was more than 1 order of magnitude larger than that of the GaAs sample. Sample 55S was determined previously to be nearly amorphous in nature and might therefore be expected to yield Ga ions much more easily than the single crystal GaAs used for the reference.

Figure 3 shows the mass spectra obtained for sample 55S through the mass range 80-95 amu. No significant mass peaks were observed for the GaAs in this mass range. The 55S spectra, however, show distinct peaks at 85, 86, 87, 88, and 89 amu. Weak peaks were also observed at 83 and 84.

It is interesting here to compare these data with the GaAs mass spectrum obtained in the 80-95 amu range using an O₂⁺ primary ion beam (see Figure 4). As was seen in Figure 2, the GaAs spectrum (sputtered with Ar) gave no observable peaks in the 80-90 amu range whereas Figure 4 shows peaks that were similar to the GaN spectra (the oxygen-containing fragments were formed as a result of ion-molecule reactions between the sample and O₂⁺ ions from the beam). This comparison would strongly indicate that the GaN films contained oxygen.

Figure 4 also indicates the existence of hydrogen in some of the fragments detected. Both [AsO]⁺ and [AsOH]⁺ fragments were believed to be responsible for the peaks observed at 91 and 92 amu, respectively. The Ga from the GaAs apparently gave rise to [GaO]⁺, [GaOH]⁺, and [GaOH₂]⁺ at (85, 87), (86, 88), and (87, 89) amu, respectively, with [GaOH]⁺ corresponding to the prominent peak.

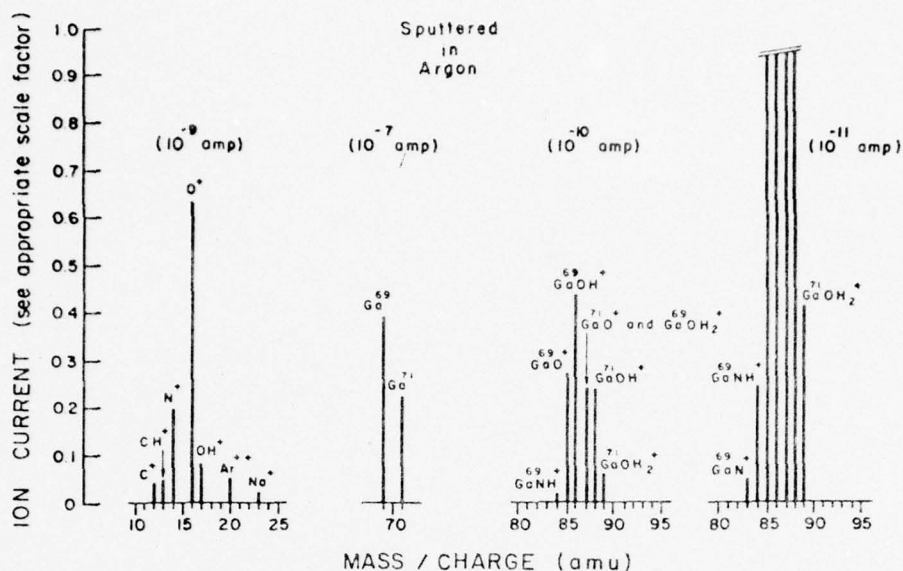


Figure 3. Mass spectrum of sample 55S (GaN) with the mass range 80-95 amu shown at two different sensitivities (this spectrum persisted throughout the remainder of the analysis of this work)

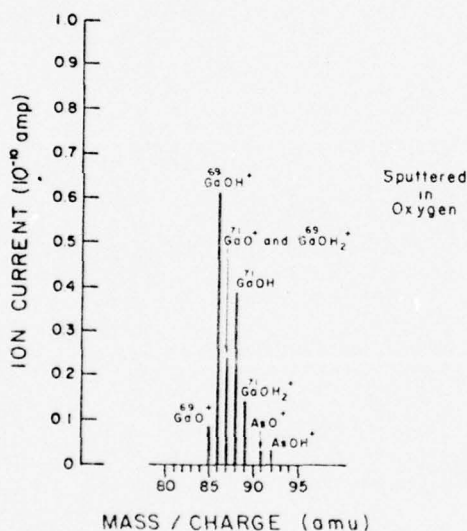


Figure 4. Mass spectrum of GaAs sputtered by O_2^+ primary ion beam. Evidence of formation of both gallium and arsenic oxide fragments in the analytical environment

It cannot be stated at this time whether the hydrogen is contributed by the ISMA environment or whether it is an impurity common to both the GaAs and GaN samples. A fragment corresponding to $[GaC]^+$ or $[GaCH]^+$ was not detected at 81 and 82 amu, respectively, and therefore cannot make any detectable contribution to the 83, 84 amu peaks.

The likelihood of $[^{69}GaCH_2]^+$ and $[^{69}GaCH_3]^+$ was considered in the interpretation of the peaks considered at 83 and 84 amu since it is here that $[^{69}GaN]^+$ and $[^{69}GaNH]^+$ would be detected if they exist and could result in an ambiguity in interpretation. The identification of the fragment ions at 83 and 84 amu as $[^{69}GaN]^+$ and $[^{69}GaNH]^+$, respectively, is supported by comparing the mass spectra of GaN samples grown by the two other processes referenced earlier.

Comparison of Mass Spectra for GaN Grown by Other Techniques. Two other samples of GaN grown by the two techniques referenced earlier (identified as the IBM and RCA samples) were analyzed while still using the GaAs for a reference. The spectra for the IBM sample are shown in

Figure 5 while the spectra for the RCA sample are shown in Figure 6.

These GaN samples resulted in spectra similar to 55S throughout the 83-89 amu range. In addition, these spectra were also similar to the one shown in Figure 4 (GaAs sputtered with oxygen) in the 85-89 amu range. The RCA sample was small and thus exposed the edge of the sapphire ($\alpha-AlO_3$) substrate to the primary ion beam; thus the oxygen indicated by the spectra for the RCA sample (i.e., through $[GaO]^+$ fragments) could easily have resulted from the ion-molecule reaction between substrate furnished oxygen and sample supplied Ga atoms. The RCA sample contributed rather definite peaks at 83 and 84 amu which were interpreted at $[^{69}GaN]^+$ and $[^{69}GaNH]^+$, respectively, which supports a similar interpretation in the 55S spectra.

Sample 55S and the IBM sample did not experience any substrate interference; therefore oxygen indicated in their spectra was interpreted as originating from the samples.

As stated earlier, hydrogen is also very much in evidence in these spectra, but cannot be identified as originating from the sample or the ISMA.

CONCLUSIONS

The qualitative analysis of deposits obtained from the pyrolysis of $Ga(C_2H_5)_3 \cdot NH_3$ has shown that the sample contains gallium, nitrogen, oxygen, and carbon, the latter being concentrated near the surface of the sample. While x-ray diffraction was relied on for the verification of the deposits to be GaN, it is significant that SIMS provided a means of directly detecting the presence of nitrogen in the deposits. Hydrocarbons from the vacuum system oil were ruled out as a source of carbon because of the absence of hydrocarbons in the GaAs spectra. Hydrocarbons detected in the S-55S film would be significant since this was suspected to be the reason for the yellow-brown color that has been characteristic of the films grown from $Ga(C_2H_5)_3 \cdot NH_3$. It was interesting to note that sample 55S has changed color (in the region being analyzed) from yellowish brown to gray. No explanation can be offered for this change in color at the present time.

The GaAs sample permitted establishing a background baseline against which the GaN spectra could be compared. The mass spectra obtained from the GaN grown by two other laboratories added confidence to the interpretation of the mass peaks as did the spectra obtained by using the oxygen primary

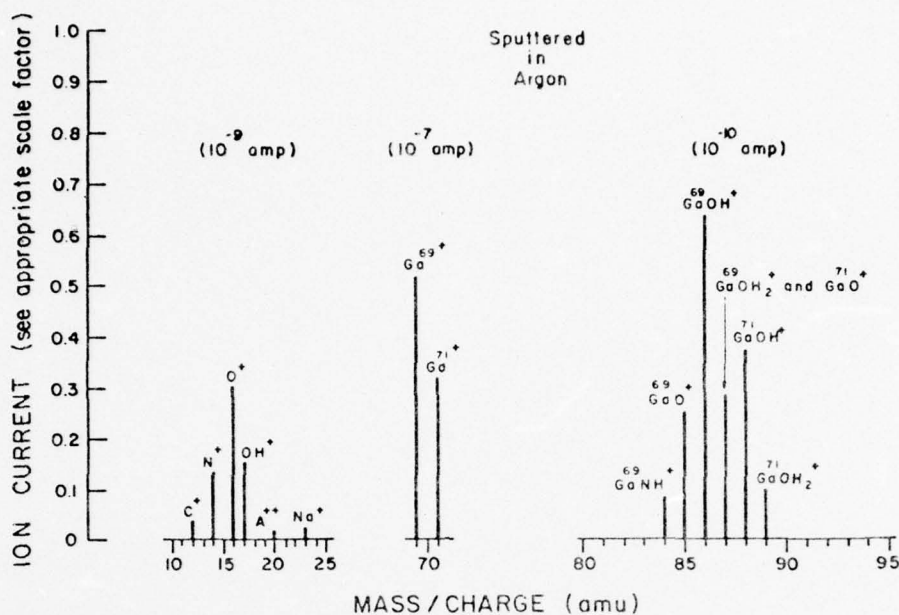


Figure 5. Mass spectrum of IBM GaN

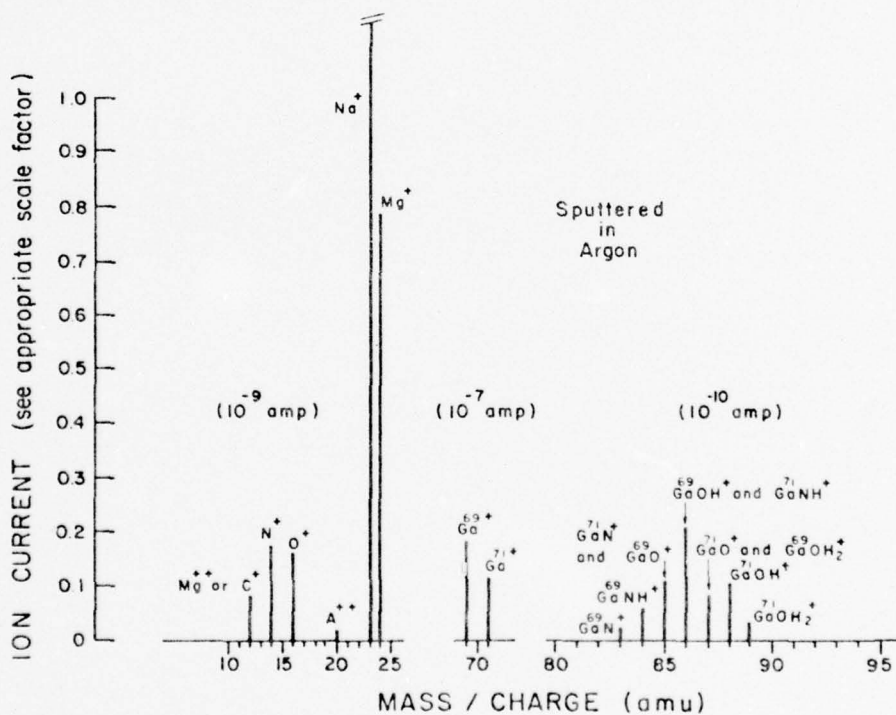


Figure 6. Mass spectrum of RCA GaN

ion beam on the GaAs sample at the end of the analysis.

Some of the fragment ions occurred at an m/e that could be explained only through the addition of one or two hydrogen atoms (or ions). Although the analytical environment of the ISMA could itself be a source of hydrogen, one cannot rule out the actual growth process and systems as a source, especially where reactants such as NH_3 or $\text{Ga}(\text{C}_2\text{H}_5)_2\text{NH}_3$ are involved. It was in fact the hydrogen question that motivated the analysis of the IBM sample which did not intentionally use any hydrogen-containing reactants. Only extremely careful experimental procedure can hope to pinpoint the source(s) of the hydrogen. It is emphasized here that the evidence for hydrogen persisted even after extended lengths of sputter etching.

Upon reviewing these spectra, it appears unnecessary to seek $[\text{GaN}]^+$ ions directly as evidence of the N in GaN for the experimental conditions described here. Nitrogen ions detected at 14 amu are attributed to the sample and not to the instrument background for the conditions of our analysis.

ACKNOWLEDGMENT

The authors are especially grateful for the courtesy and generosity extended by the Commonwealth Scientific Co., which provided the ISMA used for the analyses reported. Special thanks are due to J. I. Pankove, RCA, Princeton, N.J., and P. J. Burkhardt, IBM, Hopewell Junction, N.Y., who donated their samples for comparison, and for their permission to publish the results of the analyses related to these samples.

LITERATURE CITED

- (1) J. E. Andrews and M. A. Littlejohn, *J. Electrochem. Soc.*, **122**, 1273 (1975).
- (2) M. Ilegems, R. Dingle, and R. A. Logan, *J. Appl. Phys.*, **43**, 3797-3800 (1972).
- (3) C. A. Evans, Jr., *Anal. Chem.*, **44**, (13), 67A (1972).
- (4) C. A. Evans, Jr., *Thin Solid Films*, **19**, 11-19 (1973).
- (5) F. W. Karasek, *Res./Dev.*, **24**, 40-46 (1973).
- (6) M. Gettings and J. P. Coad, *Surf. Sci.*, **53**, 636-648 (1975).
- (7) H. J. Hovel and J. J. Cuomo, *Appl. Phys. Lett.*, **20**, 71-73 (1972).
- (8) J. C. Veseley, M. Shatzkes, and P. J. Burkhardt, *Phys. Rev. B*, **10**, 582 (1974).
- (9) R. E. Enstrom, E. A. Miller, and A. G. Sigai, Final Report for NASA-Langley Research Center, Contract NAS 12-538 (1971).

RECEIVED for review August 9, 1976. Accepted June 6, 1977.
This work was partially supported by the Office of Naval Research.

Velocity-field characteristics of GaAs with $\Gamma_6^c-L_6^c-X_6^c$ conduction-band ordering^{a)}

M. A. Littlejohn, J. R. Hauser, and T. H. Glisson

Electrical Engineering Department, North Carolina State University, Raleigh, North Carolina 27607
(Received 11 May 1977; accepted for publication 1 June 1977)

This paper describes Monte Carlo calculations of velocity-field characteristics for GaAs using the recent experimental conduction-band ordering of Aspnes, which places the $L_6^c(111)$ conduction-band minima lower in energy than the $X_6^c(100)$ minima. These calculations use intervalley deformation potentials which give the best fit to recent high-field drift velocity measurements, and at the same time give good agreement with accepted peak velocity and threshold field values.

PACS numbers: 71.25.Tn, 72.20.Ht

The recent Schottky-barrier electroreflectance measurements using synchrotron radiation^{1,2} have offered evidence that the $L_6^c(111)$ conduction-band minima in GaAs is lower in energy than the $X_6^c(100)$ minima. This is contrary to previous conduction-band ordering,³ and the observation has led to a great deal of activity toward evaluating consequences of it. Hydrostatic pressure and uniaxial stress measurements in GaAs^{4,5} suggest the $\Gamma_6^c-L_6^c-X_6^c$ ordering and are in agreement with Monte Carlo calculations based on this assumed band structure. Separate hydrostatic pressure measurements⁶ and uniaxial stress measurements⁷ complement the above experiments, and the results of resonant Raman

scattering have also been interpreted in terms of this conduction-band structure.⁸ It appears that the evidence being accumulated indicates that the $\Gamma_6^c-L_6^c-X_6^c$ conduction-band ordering is correct for GaAs.

There are Monte Carlo calculations of velocity-field characteristics for GaAs⁹⁻¹¹ using the previously accepted conduction-band ordering which are in good agreement with experimental data. These calculations are based not only on the band structure, but require a knowledge of material parameters which have not been measured and which are used as adjustable parameters in obtaining agreement between these computer

TABLE I. GaAs material parameters used in the calculations.

Bulk material parameters			
Parameter	Value	Parameter	Value
Lattice constant	5.642×10^{-8}	LO phonon energy	0.03536 eV
Density	5.36 g/cm^3	Sound velocity	$5.24 \times 10^5 \text{ cm/sec}$
Electron affinity	4.07 eV	Optical dielectric constant	10.92
Piezoelectric constant	0.16 C/m^2	Static dielectric constant	12.90
Valley-dependent material parameters			
Parameter	Conduction-band valley		
	$\Gamma(000)$	$X(100)$	$L(111)$
Acoustic deformation potential (eV)	7.0	9.27	9.2
Effective mass (m^*/m_0)	0.063	0.58	0.222
Nonparabolicity (eV^{-1})	0.610	0.204	0.461
Energy band gap (eV) (relative to valence band)	1.439	1.961	1.769
Optical deformation potential (eV/cm)	0	0	3×10^8
Optical phonon energy (eV)	0.0343
Intervalley deformation potential (eV/cm)			
from $\Gamma(000)$	0	1×10^9	1×10^9
from $X(100)$	1×10^8	7×10^8	5×10^8
from $L(111)$	1×10^9	5×10^8	1×10^9
Intervalley phonon energy (eV)			
from $\Gamma(000)$	0	0.0299	0.0278
from $X(100)$	0.0299	0.0299	0.0293
from $L(111)$	0.0278	0.0293	0.0290
Number of equivalent valleys	1	3	4

^{a)}This work was supported by a research grant from the Office of Naval Research, Washington, D.C.

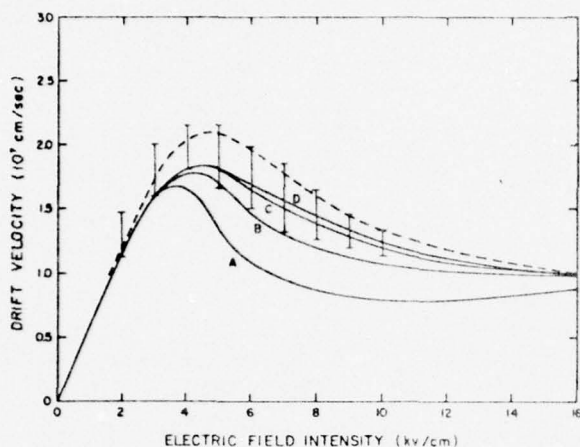


FIG. 1. Drift velocity versus electric field intensity for GaAs with a doping level of 10^{16} cm^{-3} . The solid curves are for Γ - L - X conduction-band ordering with $\Delta E_{\Gamma-L} = 0.284 \text{ eV}$ and $\Delta E_{L-X} = 0.192 \text{ eV}$. The dotted curve is for Γ - X - L ordering using $E_{\Gamma} = 1.439 \text{ eV}$, $E_X = 1.869 \text{ eV}$, $E_L = 2.0 \text{ eV}$, and $m^*(X) = 0.39m_0$. The bars show the range of reported experimental values. The values of $D_{\Gamma-L}$ are $2.5 \times 10^8 \text{ eV/cm}$ (curve A), $5 \times 10^8 \text{ eV/cm}$ (curve B), $1 \times 10^9 \text{ eV/cm}$ (curve C), $2.5 \times 10^9 \text{ eV/cm}$ (curve D).

simulations and the experimental velocity-field curves. The question arises as to what effect the new conduction-band ordering has on the Monte Carlo calculations, and what material parameter adjustments have to be made in order to obtain the same good agreement with experiment. Previous authors^{4,5} have addressed this question to some extent, although they have been primarily concerned with pressure and stress effects and with electric field intensities near the threshold field, i. e., $E \leq 5 \text{ kV/cm}$. In addition, much experimental velocity-field data taken to date has been restricted to electric field values below about 20 kV/cm .¹² Data taken at higher electric fields (20 – 100 kV/cm) show much variation in absolute values between different authors, probably due to differing experimental techniques¹³ and possibly due to contact effects.⁶ This makes theoretical calculations in the high-field region uncertain.

Houston and Evans¹³ have very recently used the time-of-flight technique to obtain what appears to be the most reliable velocity-field data taken to date for fields between 20 and 100 kV/cm . Using this data, and other reliable low-field data near the threshold field,^{11,12} as an experimental basis this paper describes Monte Carlo calculations for GaAs from low fields to 100 kV/cm considering the Γ_6^c - L_6^c - X_6^c conduction-band ordering. Intervalley deformation potentials have been used which give reasonable fits to high-field data and which also give good agreement with data near the threshold field.

The Monte Carlo transport program has been previously described,^{14,16} and is very similar to others reported for GaAs studies.^{9-11,17} Table I summarizes the material parameters used to calculate velocity-field characteristics for GaAs with Γ - L - X conduction-band ordering in our work. These parameters are essentially the same as those employed in other published simulations,^{9-11,17} except for the L and X band gaps and a few other changes to be discussed in the text.

Figure 1 shows velocity-field curves for GaAs calculated with Γ - L - X conduction-band ordering. The energy band separations of $\Delta E_{\Gamma-L} = 0.284 \text{ eV}$ and $\Delta E_{L-X} = 0.192 \text{ eV}$ originally reported by Aspnes,¹⁸ the X effective mass of $0.39m_0$,¹¹ and the equivalent intervalley deformation potential in the L valley, D_{L-L} , of $3 \times 10^8 \text{ eV/cm}$ ¹¹ have been used. Shown for comparison is a curve computed using Γ - X - L ordering with the previously accepted material parameters.¹¹ The Γ - L intervalley deformation potential, $D_{\Gamma-L}$, has been varied from 2.5×10^8 to $2.5 \times 10^9 \text{ eV/cm}$. Besides the variations in $D_{\Gamma-L}$, the effective mass $m^*(X)$, the deformation potential D_{L-L} , and the different conduction-band ordering and separations, all other material parameters have the values given in Table I. Figure 1 also shows the range of experimental values of drift velocity for fields between 2 and 10 kV/cm .^{11,12} Ionized impurity scattering has been included in the simulations with an impurity concentration of 10^{16} cm^{-3} . The inclusion of this scattering mechanism is known to reduce the maximum velocity and to increase the threshold field^{10,15,16} and was not included in previous pressure effect studies.^{4,5} It is to be noted that for these energy separations the higher values of $D_{\Gamma-L}$ ($\sim 10^9 \text{ eV/cm}$) are required to move the calculated curves into the range of experimental values near the threshold field. The low-field (100 V/cm) drift mobility for the curves of Fig. 1 has been computed by the maximum-likelihood estimation technique^{15,16} and is $6600 \text{ cm}^2/\text{V sec}$.

Our calculations indicate that the only material parameter which can be reasonably varied to extend the velocity-field curves toward those for the Γ - X - L ordering is the energy separation $\Delta E_{\Gamma-L}$. Other authors^{4,5} have had to use Γ - L separations larger than 0.284 eV to obtain agreement between stress experiments and Monte Carlo calculations. Very recently, Aspnes has used uniaxial stress experiments to infer a Γ - L separation of $\Delta E_{\Gamma-L} = 0.330 \pm 0.05 \text{ eV}$.⁷ Our calculations have

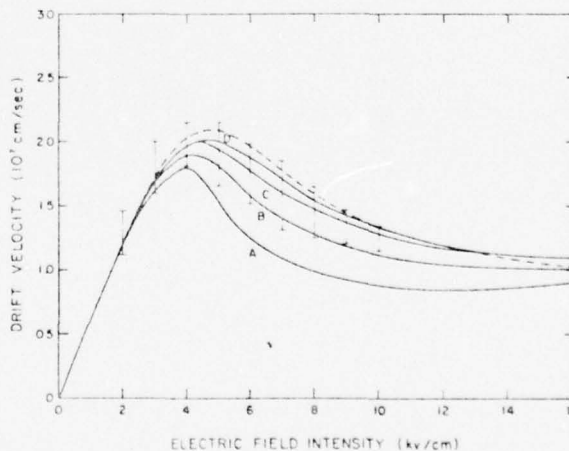


FIG. 2. Drift velocity versus electric field intensity for GaAs with a doping level of 10^{17} cm^{-3} . The solid curves are for Γ - L - X conduction-band ordering with $E_{\Gamma-L} = 0.33 \text{ eV}$ and $E_{L-X} = 0.192 \text{ eV}$. The dotted curve is for Γ - X - L ordering using the band gaps given in Fig. 1. The bars show the range of reported experimental values. The values of $D_{\Gamma-L}$ are $2.5 \times 10^8 \text{ eV/cm}$ (curve A), $5 \times 10^8 \text{ eV/cm}$ (curve B), $1 \times 10^9 \text{ eV/cm}$ (curve C), $2.5 \times 10^9 \text{ eV/cm}$ (curve D).

been repeated for higher separations and Fig. 2 shows the results for $\Delta E_{\Gamma-L} = 0.33$ eV and $\Delta E_{L-X} = 0.192$ eV. The velocity near the threshold field is very similar to both experimental data and previous simulations. However the slope of the velocity-field curve above the threshold field appears to be too small. For $\Delta E_{\Gamma-L} = 0.38$ eV and $\Delta E_{L-X} = 0.192$ eV the peak velocities are somewhat higher ($v_{max} = 2.1 \times 10^7$ cm/sec for $E = 4.7$ kV/cm with $D_{\Gamma-L} = 1 \times 10^9$ eV/cm) and the slope above threshold is smaller still. All our calculations indicate that $\Delta E_{\Gamma-L} \geq 0.33$ eV and $D_{\Gamma-L} \approx 1 \times 10^9$ eV/cm are required to give agreement between the Monte Carlo simulations and experimental velocity-field data near the threshold field.

The value of the equivalent L_6^c intervalley deformation potential, D_{L-L} , was varied to change the slope of the velocity-field curve above threshold. It was found that as D_{L-L} was varied from 3×10^8 to above 10^9 eV/cm, the velocity at 16 kV/cm could be decreased while the velocity at 5 kV/cm was effectively unchanged, indicating the desired increase in slope. The best value of D_{L-L} seems to be about $(1-2) \times 10^9$ eV/cm which results in a value of velocity at 16 kV/cm equal to the value required by the experimental data and the previous $\Gamma-X-L$ curves shown in Figs. 1 and 2. The actual best value of D_{L-L} depends somewhat on the $\Delta E_{\Gamma-L}$ separation, and good fits to the data can be achieved for fields up to 20 kV/cm using $D_{L-L} \approx 10^9$ eV/cm and $\Delta E_{\Gamma-L} \approx 0.33$ eV.

The value of $D_{L-L} = 10^9$ eV/cm also gives reasonable agreement with the best high-field data available. Figure 3 shows this data compared with the Monte Carlo calculations using $\Delta E_{\Gamma-L} = 0.33$ and 0.38 eV. Two sets of data are shown representing original measurements¹⁹ and a very recent refinement¹³ both taken by the time-of-flight technique. The Monte Carlo data for $\Delta E_{\Gamma-L} = 0.33$ eV results in a nearly correct field dependence for the velocity. However, because of the higher calcu-

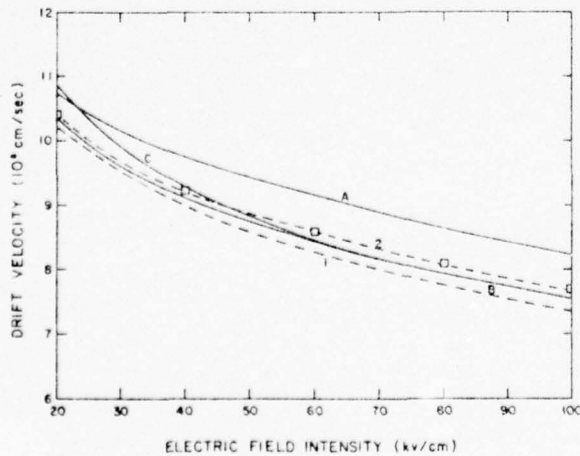


FIG. 3. Drift velocity versus electric field intensity for GaAs with a doping level of 10^{16} cm⁻³. The dotted curves are experimental data (Curve 1—least-squares fit to data of Ref. 19; curve 2—data of Ref. 13). The solid curves are Monte Carlo data (curve A— $\Delta E_{\Gamma-L} = 0.33$ eV, $m^*(X) = 0.39m_0$; curve B— $\Delta E_{\Gamma-L} = 0.33$ eV, $m^*(X) = 0.58m_0$; curve C— $\Delta E_{\Gamma-L} = 0.38$ eV, $m^*(X) = 0.58m_0$). For all curves $\Delta E_{L-X} = 0.192$ eV.

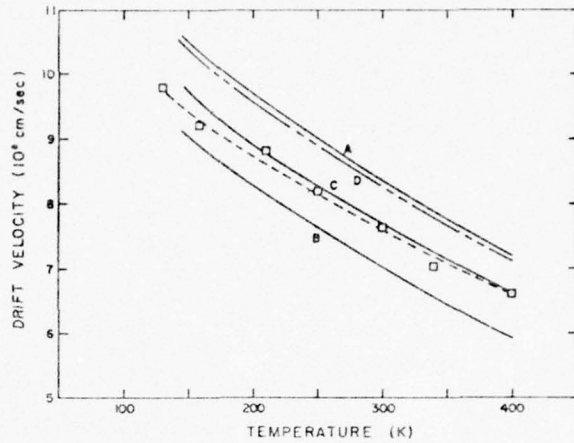


FIG. 4. Drift velocity versus temperature for GaAs with a doping level of 10^{16} cm⁻³, $E = 100$ kV/cm, $\Delta E_{\Gamma-L} = 0.33$ eV, and $\Delta E_{L-X} = 0.192$ eV. Curve A— $m^*(X) = 0.39m_0$, curve B— $m^*(X) = 0.78m_0$, curve C— $m^*(X) = 0.58m_0$, curve D— $\Delta E_{\Gamma-L} = 0.33$ eV, $\Delta E_{L-X} = 0.142$ eV, $m^*(X) = 0.39m_0$.

lated values compared with the experimental values, the effective mass in the X_6^c valley was increased to reduce the high-field velocity.¹³ The results of this calculation are shown in Fig. 3. The L_6^c mass could also be varied to reduce the velocity, but the value for this band seems more certain than the mass for the X_6^c band,² and varying the L_6^c mass would affect the near-threshold drift velocity. A value for the effective mass ratio in the X valley of 0.58 gives the best fit to the data for $\Delta E_{\Gamma-L} = 0.33$ eV, while increasing the separation to 0.38 eV causes a deviation at the lower fields. This agreement is also manifested in the temperature dependence of the near-saturation velocity. Figure 4 shows the measured temperature dependence of the drift velocity at 100 kV/cm compared to the Monte Carlo calculations as the mass in the X_6^c valley is varied. The temperature dependence and field dependence of the high-field drift velocity obtained from Monte Carlo calculations are in agreement with experiment using $m^*(X_6^c) = 0.58m_0$.

Another significant variable is the $L_6^c-X_6^c$ energy spacing, ΔE_{L-X} . Aspnes has reported this parameter to be 0.170 ± 0.03 eV at 2°K,² with a value of $0.192 + 0.04$ eV¹⁸ at 300°K. We have studied variations of ΔE_{L-X} on the Monte Carlo calculations for GaAs with $\Gamma-L-X$ conduction-band ordering. For example, curve D of Fig. 4 shows the 100-kV/cm drift velocity versus temperature for $\Delta E_{\Gamma-L} = 0.33$ eV, $m^*(X) = 0.39m_0$, and $\Delta E_{L-X} = 0.142$ eV. There is essentially no change with the decrease in ΔE_{L-X} . In fact, ΔE_{L-X} would have to be decreased below 0.1 eV to result in significant changes in any results presented so far, and this is viewed as an unreasonable value in light of Aspnes's data. At the same time, other authors^{4,5} have used ΔE_{L-X} as small as 0.02 eV in interpreting pressure effect data. However, there is a question regarding this data,⁶ and the present authors view such small values of ΔE_{L-X} as somewhat unreasonable until further results are achieved.

In summary, Monte Carlo calculations and experimental velocity-field data are in agreement using the Γ_6^c - L_6^c - X_6^c conduction-band ordering. The major parameter changes required from those used in previous Γ - X - L band-ordering calculations to achieve this agreement are $D_{\Gamma-L} = 1 \times 10^8$ eV/cm, $D_{L-L} = 1 \times 10^8$ eV/cm, and $m^*(X_6^c) = 0.58m_0$, with a minimum Γ - L energy separation of 0.33 eV. These values of deformation potentials do not coincide with the values $D_{\Gamma-L} = 2.8 \times 10^8$ eV/cm and $D_{L-L} = 1.8 \times 10^8$ eV/cm required to give the best agreement to pressure and uniaxial stress experiments.⁴ However, the actual variation and amount of increase of peak velocity and threshold field for hydrostatic pressures up to 10 kbar appears to be in question,⁶ and the previous Monte Carlo calculations probably need to be reevaluated in light of new data.⁶ In view of this uncertainty, the calculations made here are presented with material parameters which give agreement with experimental data for electric fields as large as 100 kV/cm. Additional calculations as well as experimental verification of deformation potential values should be made.

¹D.E. Aspnes, C.G. Olson, and D.W. Lynch, *Phys. Rev. Lett.* **37**, 766 (1976).

²D.E. Aspnes, *Phys. Rev. B* **14**, 5331 (1976).

³H. Ehrenreich, *Phys. Rev.* **120**, 1951 (1960).

⁴P.J. Vinson, C. Pickering, A.R. Adams, W. Fawcett, and G.D. Pitt, *Proceedings of 13th International Conference on Physics of Semiconductors, Rome, 1976*, p. 1243 (unpublished).

⁵A.R. Adams, P.J. Vinson, C. Pickering, G.D. Pitt, and W. Fawcett, *Electron. Lett.* **13**, 47 (1977).

⁶W. Czubytyj and M.P. Shaw, *Appl. Phys. Lett.* **30**, 205 (1977).

⁷D.E. Aspnes and M. Cardona, *Bull. Am. Phys. Soc.* **22**, 410 (1977).

⁸R. Trommer and M. Cardona, *Solid State Commun.* **21**, 153 (1977).

⁹W. Fawcett, A.D. Boardman, and S. Swain, *J. Phys. Chem. Solids* **31**, 1963 (1970).

¹⁰J.G. Ruch and W. Fawcett, *J. Appl. Phys.* **41**, 3843 (1970).

¹¹W. Fawcett and D.C. Herbert, *J. Phys. C* **7**, 1641 (1974).

¹²B.G. Bosch and R.W.H. Engelmann, *Gunn-effect Electronics* (Wiley, New York, 1975), pp. 25 and 206.

¹³P.A. Houston and A.G.R. Evans, *Solid-State Electron.* **20**, 197 (1977).

¹⁴M.A. Littlejohn, J.R. Hauser, and T.H. Glisson, *Appl. Phys. Lett.* **26**, 625 (1975).

¹⁵J.R. Hauser, M.A. Littlejohn, and T.H. Glisson, *Appl. Phys. Lett.* **28**, 458 (1976).

¹⁶M.A. Littlejohn, J.R. Hauser, and T.H. Glisson, *Appl. Phys. Lett.* **30**, 242 (1977).

¹⁷T.J. Maloney and J. Frey, *J. Appl. Phys.* **48**, 781 (1977).

¹⁸D.E. Aspnes, *IEEE Trans. Electron Devices* **ED-23**, 1256 (1976).

¹⁹P.A. Houston and A.G.R. Evans, *IEEE Trans. Electron Devices* **ED-23**, 584 (1976).

ENERGY BANDGAP AND LATTICE CONSTANT
CONTOURS OF III-V QUATERNARY ALLOYS*

T. H. Glisson, J. R. Hauser, M. A. Littlejohn, C. K. Williams

North Carolina State University
Electrical Engineering Department
Raleigh, North Carolina 27607

Energy band gap and lattice constant contours are presented for the nine quaternary alloys formed from Al, Ga, In and P, As, Sb. The quaternary bandgaps were obtained using an interpolation formula proposed by Moon et al. The quaternary lattice constants were obtained by use of a linear interpolation technique using the binary lattice constants as boundary values.

Key words: quaternary alloys, bandgap, lattice constant.

Introduction

There has been considerable interest in the quaternary III-V semiconductor materials for many applications, such as electro-optics and microwave devices [1-6]. One significant reason for this interest is the ability to synthesize materials with a fixed lattice constant and a variable range of energy bandgaps or, conversely, to synthesize materials with a constant energy bandgap and a variable lattice constant [7].

*This work was supported by a research grant from the Office of Naval Research, Washington, D.C.

In order to predict the energy bandgap or lattice constant for a quaternary material a two-step sequence is involved. Initially, it is necessary to have available experimental (or theoretical) values of these material parameters for the four possible binary III-V constituents of the quaternary compound. These values are readily available for most III-V materials in the literature [8]. There are also four possible ternary (pseudobinary) III-V systems in a given quaternary compound. In the first step, the energy bandgap and lattice constant as a function of alloy composition for each ternary system is computed from the known binary material parameters. This computation is on a good experimental and theoretical basis [9-13] involving the use of Vegard's law and the concept of the "bowing parameter" for the energy bandgap [14]. The final step involves the use of the compositional dependence of the energy bandgap and lattice constant for the four ternary combinations to interpolate to the desired quaternary energy bandgap and lattice constant. This final interpolation step is somewhat empirical in nature. There appear to be several such interpolation techniques used in the literature [6,7,15] and while these are similar, they also have non-trivial differences. This paper will discuss this critical interpolation procedure in view of the small amount of experimental quaternary data, and will present calculations for energy bandgaps and lattice constants for the nine quaternary alloys formed from Al, Ga, In and P, As, Sb using one of these interpolation techniques.

Notation

There appears to be no generally-accepted scheme for symbolically describing the III-V quaternary alloys. In this paper the following convention has been adopted. Within both the group III and group V pairing, the first position is occupied by the element with lowest atomic number. The composition variables are associated with the four elements in the order $1-x$, x , $1-y$, y . For example, a quaternary alloy will be denoted as $A_{1-x}B_xC_{1-y}D_y$. Here A and B are group III elements with A having lower atomic number than B. Likewise, C and D are group V elements with C having lower atomic number than D. Following previous authors [6,7], a quaternary alloy parameter (e.g., bandgap or lattice constant) is described by a surface $Q(x,y)$ over

the x, y composition plane ($0 < x < 1, 0 < y < 1$). At the corners (x and y equal to zero and/or one) the values of the parameter for the four binary elements $Q(0,0) = B_1$, $Q(1,0) = B_2$, $Q(1,1) = B_3$ and $Q(0,1) = B_4$ are obtained. Along the boundaries of the plane the parameter for the four ternary elements $Q(x,0) = T_{12}(x)$, $Q(1,y) = T_{23}(y)$, $Q(x,1) = T_{43}(x)$ and $Q(0,y) = T_{14}(y)$ are obtained.

Estimation of Alloy Parameters

Many ternary alloy parameters (e.g. lattice constant) are obtained by linear interpolation from those of the constituent binary compounds, i.e.,

$$T_{ij}(x) = xB_j + (1-x)B_i \quad (1)$$

For some parameters the theoretical variation with composition is nonlinear [14,16]. For the direct bandgap for example, Thompson and Woolley [9] have shown that

$$T_{ij}(x) = xB_j + (1-x)B_i - C_{ij}x(1-x) \quad (2)$$

where C_{ij} is the bowing parameter for the ternary alloy bandgap T_{ij} .

In the absence of definitive theories for quaternary parameters, estimates of a quaternary alloy parameter $Q(x,y)$ must be obtained by interpolation from the four ternary alloy parameters T_{ij} . Various interpolation schemes have been proposed. Onton and Chicotka [15] used the solution of Laplace's equation subject to the boundary conditions $Q(x,0) = T_{12}(x)$, etc. In Monte Carlo transport studies [6] the present authors have used the interpolation equation

$$Q(x,y) = \frac{x(1-x)[(1-y)T_{12}(x) + yT_{43}(x)] + y(1-y)[(1-x)T_{14}(y) + xT_{23}(y)]}{x(1-x) + y(1-y)} \quad (3)$$

This interpolation equation reduces to the ternary parameters on the quaternary plane boundaries and to the average

of the ternary parameters at the midpoint ($x=0.5, y=0.5$) of the compositional plane. This is incidentally the solution to Laplace's equation if the T_{ij} are linear as in Eq. (1). Moon et al. [7] have proposed similar schemes for the estimation of lattice constant and bandgap. For the lattice constant, Moon gives (in the above notation)

$$Q(x,y) = B_1 + (B_2 - B_1)x + (B_4 - B_1)y + (B_1 - B_2 + B_3 - B_4)xy \quad (4)$$

For the lattice constant, the T_{ij} are assumed to be linear in their arguments, so the solution to Laplace's equation is identical to Eq. (3), which in turn also reduces to Eq. (4).

For the bandgap, Moon et al. have used the equation

$$Q(x,y) = (1-x)T_{14}(y) + x T_{23}(y) - \Delta \quad (5)$$

where the T_{ij} are determined from Eq. (1) and

$$\Delta = x(1-x)[(1-y)C_{12} + yC_{43}] + y(1-y)[(1-x)C_{14} + xC_{23}] \quad (6)$$

An important difference between this bandgap estimate and that obtained from Eq. (3) is in the manner in which the ternary bowing parameters C_{ij} enter the calculation. In Eq. (3), the ternary bowing effects are included in the T_{ij} , whereas in Moon's method the bowing enters as a separate quaternary bowing parameter term given in Eq. (6). At the center of the composition plane, Eq. (3) yields (for the quaternary bowing) $1/16 (C_{12} + C_{43} + C_{14} + C_{23})$ and Eq. (5) gives $1/8 (C_{12} + C_{43} + C_{14} + C_{23})$, which is twice as large. Thus, at the center, Eq. (3) gives the average of the bowing contributions from the four ternaries, whereas Eq. (5) gives the average of the bowing contributions from the two sublattices. This is the principle difference between the interpolation schemes of Refs. 6 and 7.

Comparison with Experiment

Onton and Chicotka compared their interpolation approach (solution to Laplace's equation) with measured values of the quaternary bandgap in $\text{Ga}_{1-x}\text{In}_x\text{P}_{1-y}\text{As}_y$ and found the interpolated values to be within ± 30 meV of the measured values. We have repeated this comparison, using their measured data. The results are given in Table 1. The average error and standard deviation of the error are also shown, and it is seen that Eqs. (3) and (5) give comparable errors.

Table I. Comparison of Eqs (3) and (5) with Experimental Data for $\text{Ga}_{1-x}\text{In}_x\text{P}_{1-y}\text{As}_y$.

Composition		Bandgap (eV)		
x	y	Eq (3)	Eq (5)	Measured [15]
0.004	0.260	2.357	2.353	2.222
0.006	0.340	2.244	2.239	2.124
0.006	0.420	2.136	2.131	1.993
0.009	0.500	2.027	2.020	1.881
0.008	0.590	1.913	1.907	1.738
0.010	0.710	1.763	1.755	1.592
0.012	0.830	1.619	1.609	1.475
0.017	0.910	1.521	1.510	1.351
0.015	0.970	1.455	1.447	1.326
0.060	0.220	2.336	2.297	2.203
0.060	0.280	2.255	2.214	2.135
0.070	0.340	2.160	2.113	2.038
0.080	0.440	2.014	1.963	1.869
0.110	0.650	1.709	1.650	1.535
0.110	0.700	1.649	1.591	1.472
0.170	0.850	1.383	1.326	1.236
0.190	0.975	1.184	1.166	1.165
0.250	0.140	2.124	2.054	2.101
0.230	0.190	2.100	2.021	2.041
0.250	0.240	2.008	1.921	1.953
0.250	0.310	1.924	1.830	1.809
0.260	0.630	1.523	1.430	1.388
0.330	0.800	1.225	1.145	1.170
0.340	0.090	2.029	1.971	2.077

Table I continued.

Composition		Bandgap (eV)		
x	y	Eq (3)	Eq (5)	Measured [15]
0.370	0.120	1.954	1.883	1.978
0.410	0.170	1.843	1.757	1.850
0.400	0.030	1.983	1.957	2.086
0.460	0.040	1.887	1.854	2.019
0.500	0.040	1.830	1.797	1.953
0.570	0.060	1.723	1.678	1.854
0.650	0.060	1.625	1.580	1.750
0.710	0.060	1.558	1.513	1.686
0.830	0.100	1.401	1.346	1.470
0.870	0.130	1.333	1.276	1.389
0.920	0.190	1.216	1.166	1.268
Average error (eV)		-0.052	-0.008	
rms error (eV)		0.109	0.118	

Calculation of Lattice Constant and Bandgap

For the calculation of the lattice constant, the three methods discussed above are identical, as given in Eq. (4). For the calculation of the bandgap, we have elected to use Moon's procedure, since it has some theoretical basis, whereas the other two are more or less ad hoc.

The quaternary lattice constant and energy bandgap contours are presented in Figure 1(a)-(i). These contours were obtained by numerical solutions of Eqs. (4) and (5), using the data given in Table 2. In all cases, the lowest quaternary bandgap is plotted in Figure 1. The shaded regions represent compositions for which the quaternary alloy is an indirect bandgap material.

Table II. Parameters Used in the Calculation of Quaternary Bandgaps and Lattice Constants

Compound	Bandgaps (ev)			Lattice Constant (Å)
	$\Gamma(000)$	X(100)	L(111)	
AlP	3.6	2.42	4.0	5.462
AlAs	2.95	2.153	3.3	5.6611
AlSb	2.25	1.52	1.85	6.135
GaP	2.74	2.26	3.0	5.4495
GaAs	1.439	1.961	1.769	5.64191
GaSb	0.69	1.11	0.765	6.094
InP	1.34	2.04	1.87	5.86875
InAs	0.359	2.1	1.6	6.0584
InSb	0.175	1.0	0.63	6.47877

a) Binary bandgaps and lattice constants

Alloy	Bowling Parameter		
	$\Gamma(000)$	X(100)	L(111)
(Al,Ga)P	0.0*	0.0	0.0
(Al,Ga)As	0.26	0.02	0.45
(Al,Ga)Sb	0.0	0.0	0.0
(Al,In)P	0.0	0.0	0.0
(Al,In)As	0.52*	0.0	0.0
(Al,In)Sb	0.42*	0.0	0.0
(Ga,In)P	0.758	0.15	0.68
(Ga,In)As	0.6	0.15	0.5
(Ga,In)Sb	0.43	0.24	0.33
Al(P,As)	0.22*	0.0	0.0
Al(P,Sb)	1.2*	0.0	0.0
Al(As,Sb)	0.72*	0.0	0.0
Ga(P,As)	0.21	0.21	0.25
Ga(P,Sb)	1.2*	0.0	0.0
Ga(As,Sb)	0.65*	0.0	0.0
In(P,As)	0.27	0.27	0.26
In(P,Sb)	1.2	0.0	0.0
In(As,Sb)	0.596	0.6	0.55

b) Ternary bowling parameters

*denotes estimate from Figure 2. In the X&L valleys unknown parameters are equated to zero.

Estimation of Unknown Ternary Bowing Constants

Relatively few of the III-V ternary bowing constants are known with any certainty, especially for the X(100) and L(111) valleys. Figure 2 shows the reported bowing parameters for several ternary materials as a function of the lattice constant difference between the two end-point binary compounds. While there is some uncertainty in the experimental data there does appear to be a definite trend toward larger bowing parameters with larger lattice constant differences. The solid line relationship shown in Figure 2 has been used to estimate several unknown bowing constants, as identified by the asterisks in Table 2. Since bowing is known to occur, it was felt that this procedure is better than arbitrarily setting the unknown bowing constants to zero.

Summary

Calculated bandgap and lattice constant contours have been presented for nine quaternary III-V material systems. The calculated values are based upon interpolation techniques which use known values of ternary III-V parameters to estimate the bandgap and lattice constant parameters for the quaternary systems. Since there is some uncertainty in both the ternary parameters and the best interpolation technique these calculated values must be considered as first order approximations until more experimental data is obtained for the quaternary systems. However, the curves should prove useful for many studies of the general properties of the increasingly important III-V quaternary materials.

Acknowledgments

We would like to express our appreciation to J. Shade for his assistance in this work.

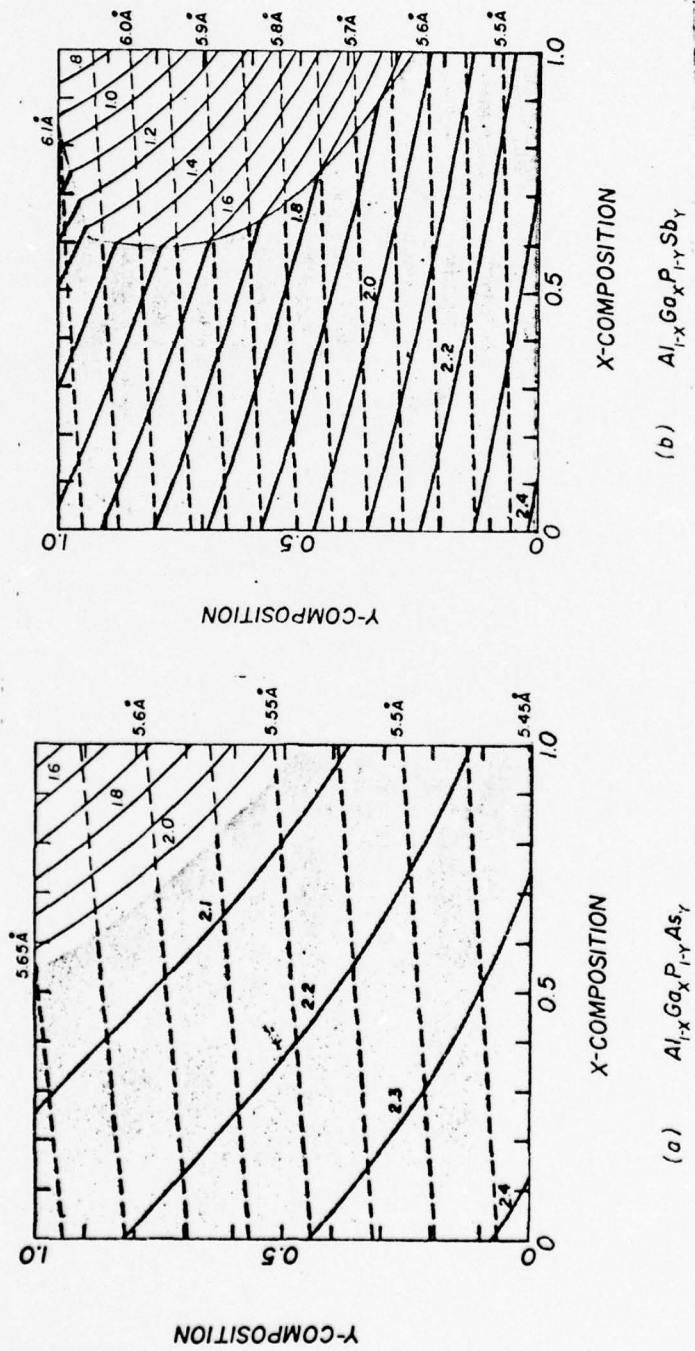


Figure 1. Energy bandgap and lattice constant contours for III-V quaternary alloys. The solid curves are the energy gap contours and the dashed curves are lattice constant contours. The shaded region shows the compositional range over which the material has an indirect bandgap.

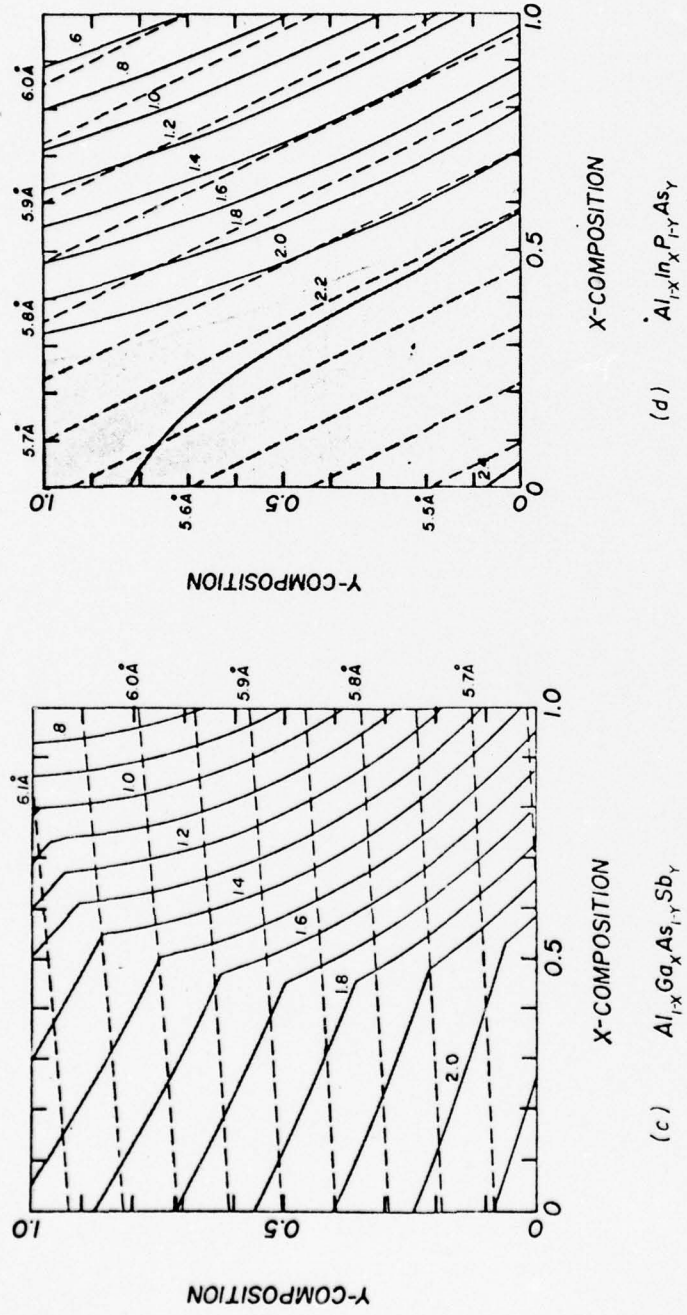


Figure 1 (continued)

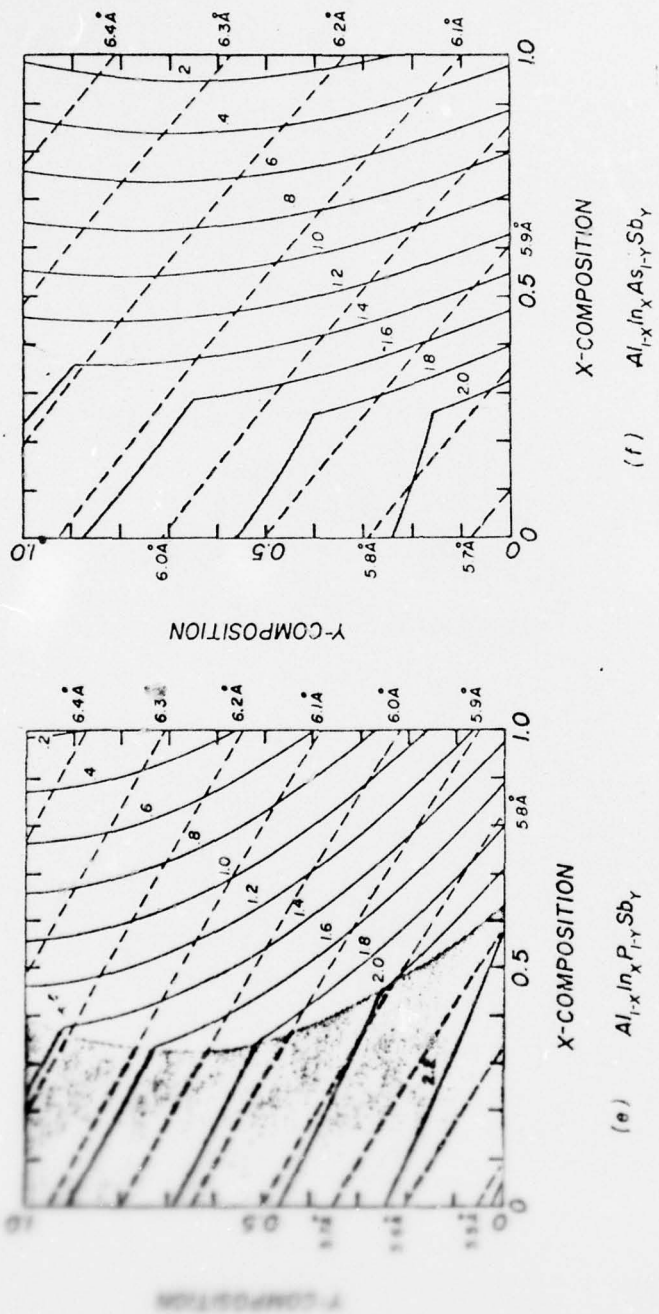


Figure 1 (continued)

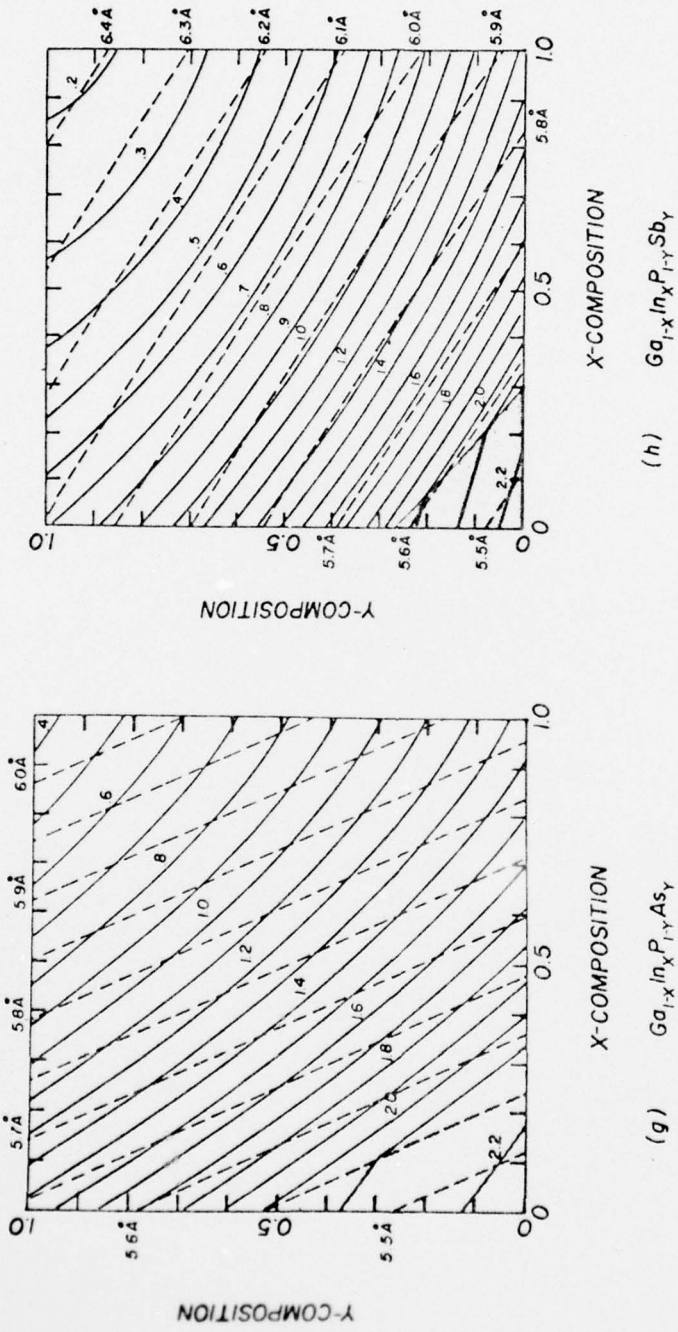


Figure 1 (continued)

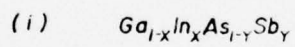
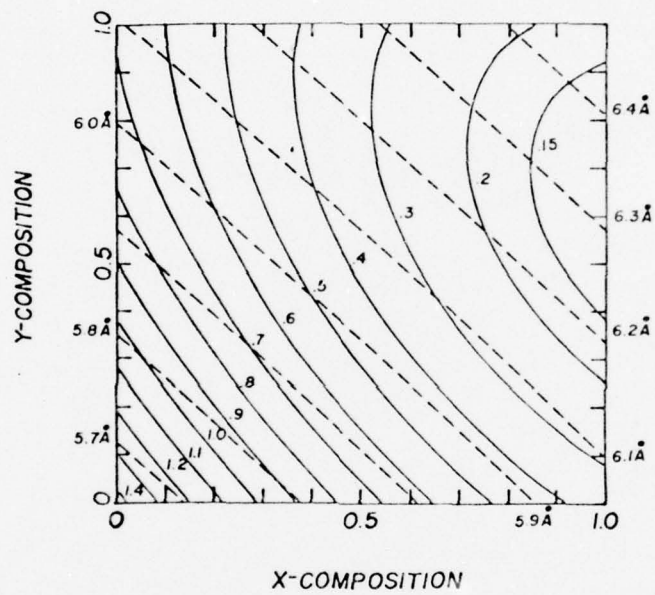


Figure 1 (continued)

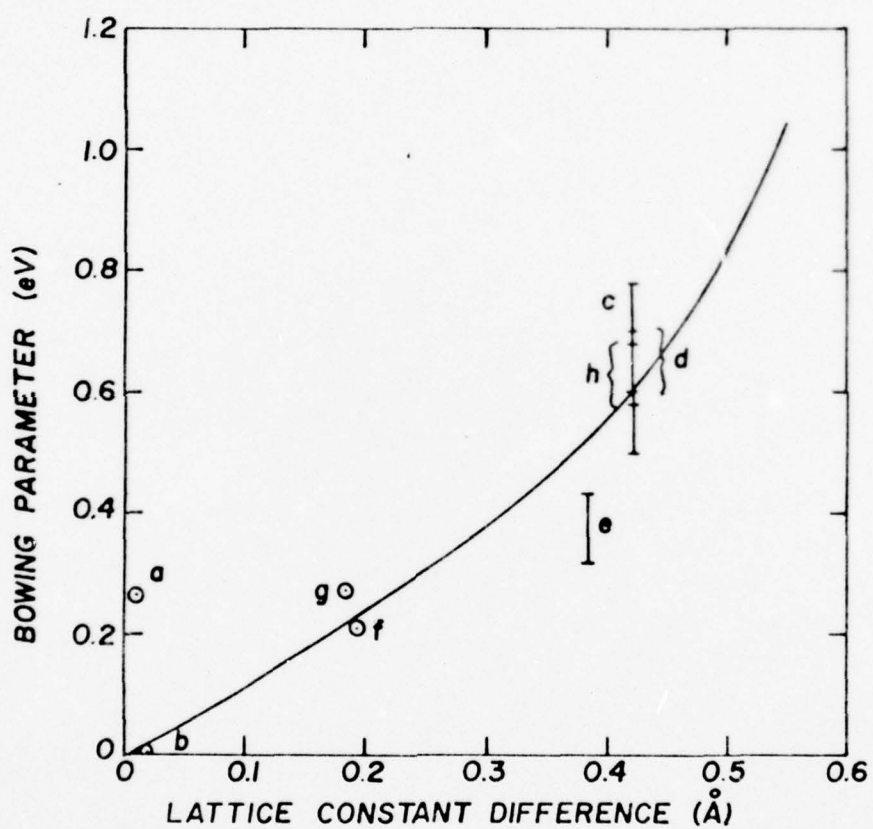


Figure 2. Experimental bowing parameters versus lattice constant difference for III-V ternary alloys. (a) $\text{Al}_{1-x}\text{Ga}_x\text{As}$, (b) $\text{Al}_{1-x}\text{Ga}_x\text{Sb}$, (c) $\text{Ga}_{1-x}\text{In}_x\text{P}$, (d) $\text{Ga}_{1-x}\text{In}_x\text{As}$, (e) $\text{Ga}_{1-x}\text{In}_x\text{Sb}$, (f) $\text{GaP}_{1-x}\text{As}_x$, (g) $\text{InP}_{1-x}\text{As}_x$, (h) $\text{InAs}_{1-x}\text{Sb}_x$.

References

1. J. S. Etcher, G. A. Antypas, and J. Edgecombe, Appl. Phys. Lett. 29, 153 (1976).
2. P. D. Wright, J. J. Coleman, N. Holonyak, M. J. Ludowisc, and G. E. Stillman, Appl. Phys. Lett. 29, 18 (1976).
3. J. J. Hsieh, J. A. Rossi, and J. P. Donnelly, Appl. Phys. Lett. 28, 709 (1976).
4. T. P. Pearson, B. I. Miller, R. J. Clark, K. J. Bachmann, Appl. Phys. Lett. 28, 499 (1976).
5. C. J. Neuse, Technical Digest IEDM, Washington, D.C., p. 125, Dec. 1976.
6. M. A. Littlejohn, J. R. Hauser, and T. H. Glisson, Appl. Phys. Lett. 30, 242 (1977).
7. R. L. Moon, G. A. Antypas, and L. W. James, J. Electron. Mater. 3, 635 (1974).
8. M. Neuberger, Handbook of Electronic Materials, vol. 2, III-V Semiconducting Compounds (IFI/Plenum, New York, 1971).
9. A. G. Thompson and J. C. Woolley, Can. Jour. Phys. 45, 255 (1967).
10. J. A. Van Vechten and T. K. Bergstresser, Phys. Rev. B 1, 3351 (1970).
11. K. S. Song, Solid State Commun. 13, 1397 (1973).
12. M. Altarelli, Solid State Commun. 15, 1607 (1974).
13. A. Onton, Jour. Luminescence 7, 95 (1973).
14. J. W. Harrison and J. R. Hauser, Phys. Rev. B 13, 5347 (1976).
15. A. Onton and R. J. Chicotka, International conf. on Luminescence, Leningrad, 1972.

References continued.

16. J. W. Harrison and J. R. Hauser, Jour. Appl. Phys.
47, 292 (1976).

HIGH FIELD TRANSPORT AND MICROWAVE MESFET PERFORMANCE IN TERNARY AND QUATERNARY III-V SEMICONDUCTORS

H. A. Littlejohn, J. R. Hauser, T. H. Glisson and L. A. Arledge
North Carolina State University
Raleigh, N. C. 27607

INTRODUCTION

The GaAs MESFET has become widely recognized as an excellent microwave transistor for both low-noise, small signal amplification and power amplification through X-band [1,2], and it is also emerging as an important logic element for high-speed digital applications [3]. The advantages of this device can be attributed primarily to its technologically simple structure and to the material transport properties of GaAs [4]. This naturally prompts an examination of other materials having properties which could lead to improvements in basic device performance. Based on this consideration microwave transistors have been fabricated from InP [5] and $Ga_{1-x}In_xAs$ [7] and theoretical calculations have suggested that $InP_{1-x}As_x$ [7] and $Ga_{1-x}In_xP_{1-y}As_y$ [8] have transport properties which are favorable for improvements in MESFET performance.

This paper will discuss MESFET performance in the three quaternary material systems $Ga_{1-x}In_xP_{1-y}As_y$, $Al_{1-x}In_xP_{1-y}As_y$, and $Ga_{1-x}In_xP_{1-y}Sb_y$. This discussion will center around results obtained from the Monte Carlo method. These results have been applied in device models to obtain performance parameters relative to GaAs. Several aspects related to the device performance will also be addressed. These include the influence of alloy scattering, non-uniform field distributions, non-equilibrium transient effects (velocity overshoot), and the revised conduction band structure of GaAs [9].

MATERIAL PROPERTIES FOR MONTE CARLO CALCULATIONS

If the Monte Carlo method is to be used as a predictive tool for ternary and quaternary materials, an important factor relates to the manner in which material parameters are estimated and computed. This can be illustrated by reference to Figure 1, where the compositional plane ($0 \leq x \leq 1$, $0 \leq y \leq 1$) is shown for a quaternary alloy $A_{1-x}^{III}B_x^{III}C_{1-y}^{IV}D_y^{IV}$. First, it is assumed that all material parameters needed for the Monte Carlo method are known for the binary III-V compounds at the corners of the compositional plane (AC, BC, AD, BD). This is a reasonable assumption, although some material parameters for the higher energy conduction band minima (e.g. the L and X conduction bands) are uncertain. These parameters are usually estimated from those for materials having these minima at the lowest conduction band valley [10,11]. Next, the material properties for the four ternary materials are calculated based on theoretical models [12,13] or else they are linearly interpolated between those parameters for the respective binary constituent compounds [7,8].

The final step in the procedure is to use an interpolation equation for the quaternary material parameter at the general composition point (x,y) , or else to use available theoretical results [8]. The measure of success of this procedure must depend on the accumulation of experimental data, and the results for the $\text{Ga}_{1-x}\text{In}_x\text{P}_{1-y}\text{As}_y$ quaternary system support the validity of this interpolation method. These results include the energy band gap data [14], the LO phonon data [15], and the effective mass, low-field mobility, and drift-velocity data [16].

DEVICE MODELS AND MONTE CARLO CALCULATIONS

The availability of material parameters allows a steady-state drift velocity-electric field characteristic to be computed for a given material by the Monte Carlo method. The relationship of a computed velocity-field characteristic to two other characteristics which have been used in device models to calculate MESFET performance parameters is shown in Figure 2 for GaAs. The Monte Carlo velocity-field curve has been computed using the Γ -L-X conduction band ordering for GaAs [9], and the material parameters have been adjusted to give a good fit to experimental velocity-field data for GaAs [21]. The peak velocity is somewhat lower than previous calculations, and has some slight effects on the results presented here. The device models have been described by Lehovc and Zuleeg [17] and by Pucel, et al. [1,18], and both have been used recently in the literature as design models for MESFET's [1,18,19]. While these models include velocity saturation in two different ways, they do not include the negative differential mobility present in the static velocity-field curve. These models are used here in only a quantitative way to obtain a comparison between the performance parameters for GaAs and the quaternary materials.

Table 1 shows a comparison between the calculated performance parameters for a GaAs MESFET using the Monte Carlo velocity-field curve to provide the data for the model characteristics. The most serious discrepancy between the two models lies in the values of the small signal drain-source resistance, r_{DS} . This discrepancy affects other parameters leading primarily to differences between f_{max} and unilateral gain for the two models. This points out one of the most serious limitations of these analytical device models.

TERNARY AND QUATERNARY MESFET PERFORMANCE

The velocity-field characteristics for the quaternary materials $\text{Ga}_{1-x}\text{In}_x\text{P}_{1-y}\text{As}_y$, $\text{Al}_{1-x}\text{In}_x\text{P}_{1-y}\text{As}_y$, and $\text{Ga}_{1-x}\text{In}_x\text{P}_{1-y}\text{Sb}_y$ have been studied in this work. For the purpose of this paper Table 2 summarizes the results for six significant compositions from these materials. Tabulated for comparison are the results for GaAs. The table shows velocity-field data both with and without alloy scattering to illustrate the effects of this important scattering process on the transport characteristics [20]. More will be said on this point in the next section.

Table 3 shows the results of the MESFET calculations using the material parameters in Table 2 as a basis. Results are given for Pucel's model only, both with and without alloy scattering. There are slight discrepancies between the two models used for Table 1, but the results shown here are representative of both models. It can be seen that there are predicted improvements in MESFET performance for these ternary and quaternary materials with respect to GaAs.

OTHER DEVICE-RELATED ASPECTS

There are several other aspects of the Monte Carlo method which are viewed as important in their relation to device performance. A brief discussion of these follows:

- a. Alloy Scattering: The results have indicated that alloy scattering degrades device performance. Presently, there is a great deal of uncertainty in the scattering potential used to estimate the influence of alloy scattering on transport properties, and three different scattering potentials have been proposed [20]. Figure 3 shows the effect of these scattering potentials on the velocity-field calculations for $\text{Al}_{.25}\text{In}_{.75}\text{P}_{.25}\text{As}_{.75}$ and Table 4 shows the extent of device performance degradation for this quaternary material. Depending on the scattering potential used, the degree of degradation can be quite severe. The actual extent of alloy scattering in the ternary and quaternary materials will most likely determine their usefulness for the MESFET and other microwave devices.
- b. Transient Transport Effects: The dynamics of electron transport in small devices such as the MESFET have been proposed as a basic frequency-determining phenomena in these devices [22,23]. These effects have been investigated in the quaternary systems, and a typical result is shown in Figure 4. Here the "velocity overshoot" is shown for $\text{Ga}_{.27}\text{In}_{.73}\text{P}_{.4}\text{As}_{.6}$ with and without alloy scattering and compared to GaAs. The results for GaAs are slightly different from previous results [22,23]. The differences can be attributed to the use here of a three-band model appropriate to the band structure of Aspnes [9]. Again, the influence of alloy scattering is evident.
- c. Non-Uniform Field Distribution: In a realistic device, the electric field intensity will vary with position along the channel. We have developed a Monte Carlo program which allows calculations to be made with a non-uniform field. Figure 5 shows the velocity along the channel of a device with a field distribution which varies linearly from 1 kV/cm at $x=0$ to 16 kV/cm at $x=1.5 \mu\text{m}$ and $x=3 \mu\text{m}$. Also, shown in this figure is the static drift velocity along the channel. It can be seen that there are velocity overshoot effects for this non-uniform field variation where the electron has been injected at $x=0$ from a static electron distribution corresponding to a field of 1 kV/cm. These overshoot effects are not as dramatic as those for a step-field distribution [22,23], but when averaged over the channel could lead to reduced transit time.

The overshoot effects for a device with an electric field distribution calculated from a short channel JFET model [24] are shown in Figure 6. This field distribution allows for both source and drain parasitic regions

to be included. For this model, the gain-bandwidth product has been numerically evaluated and the results are indicated in Figure 6 for both GaAs and $\text{Ga}_{.27}\text{In}_{.73}\text{P}_{.4}\text{As}_{.6}$. The results agree reasonably well with the device models, and are somewhat less than previous overshoot calculations [25].

SUMMARY

High field transport properties of several ternary and quaternary III-V semiconductors used in small signal device models predict that improvements in MESFET performance over GaAs can be achieved. The effect of alloy scattering generally degrades device performance and limits the improvements which are predicted for these materials. In addition, dynamic effects in these ternary and quaternary III-V semiconductors are enhanced when compared to similar effects for GaAs.

ACKNOWLEDGMENTS

This work was supported by research contract No. N00014-70-A-0120-0004 from the Office of Naval Research, Arlington, VA, and by research contract No. F33615-76-1265 from the Air Force Avionics Laboratory, Wright-Patterson AFB, Ohio.

LIST OF REFERENCES

1. R. A. Pucel, D. J. Masse, and C. F. Krumm, *IEEE J. Solid-State Ckts.* SC-11 243 (1976).
2. H. M. Macksey, R. L. Adams, D. N. McQuidy, D. W. Shaw, and W. R. Wisseman, *IEEE Trans. Elec. Dev.* ED-24 113 (1977).
3. C. A. Liechti, *Proc. Sixth Int. Symp. on Gallium Arsenide and Related Compounds*, Inst. Phys. Conf. Serv. No. 33A, p. 227 (1976).
4. J. Frey and R. Bowers, *Adv. in Electronics and Electron Physics*, vol. 38, p. 147 (1975).
5. J. Barrera and R. Archer, *IEEE Trans Elec. Dev.* ED-22 1023 (1975).
6. D. R. Decker, R. D. Fairman, and C. K. Nishimoto, *Proc. Fifth Biennial Cornell Electrical Engineering Conf.*, vol. 5, p. 305 (1975).
7. J. R. Hauser, M. A. Littlejohn, and T. H. Glisson, *Appl. Phys. Lett.* 28 458 (1976).
8. M. A. Littlejohn, J. R. Hauser, and T. H. Glisson, *Appl. Phys. Lett.* 30 242 (1977).
9. D. E. Aspnes, *Phys. Rev. B* 14 5331 (1976).
10. W. Fawcett, A. D. Boardman, and S. Swain, *J. Phys. Chem. Sol.* 31 1963 (1970).
11. W. Fawcett and D. C. Herbert, *J. Phys. C* 7 1641 (1974).
12. J. W. Harrison and J. R. Hauser, *Phys. Rev. B* 13 5347 (1976).
13. J. W. Harrison and J. R. Hauser, *Jour. Appl. Phys.* 47 292 (1976).
14. R. L. Moon, G. A. Antypas, and L. W. James, *J. Electron. Mat.* 3 635 (1974).
15. M. J. Ludowisc, E. A. Rezek, H. Shichijo, P. D. Wright, and N. Holonyak, Jr., *Jour. Appl. Phys.*, to be published.
16. B. B. Houston, J. B. Restorf, J. R. Burke, and R. E. Hayes, paper CK10

- APS Solid State Meeting, San Diego (1977). Also, results presented at Int. Hot Electron Conf., July 6-8, 1977, to be published in Solid-State Electronics.
17. K. Lehovc and R. Zuleeg, Solid-State Electronics 13 1415 (1970).
 18. R. A. Pucel, H. A. Haus, and H. Statz, Adv. in Electronics, and Electron Physics, vol. 38, p. 195 (1975).
 19. S. Asai, S. Okazaki, and H. Kodera, Solid-State Electronics, 19 461 (1976).
 20. M. A. Littlejohn, J. R. Hauser, T. H. Glisson, D. K. Ferry, and J. W. Harrison, presented at Hot Electron Conf., Denton, Texas, July 6-8, 1977, to be published in Solid State Electronics.
 21. M. A. Littlejohn, J. R. Hauser, T. H. Glisson, to be published in Jour. Appl. Phys., Nov., 1977.
 22. J. G. Ruch, IEEE Trans. Elec. Dev. ED-19 652 (1972).
 23. T. J. Maloney and J. Frey, Jour. Appl. Phys. 48 781 (1977).
 24. J. R. Hauser, Solid-State Electronics 10 577 (1967).
 25. T. J. Maloney and J. Frey. IEEE Trans. Elec. Dev. ED-23 519 (1976).

TABLE 1: Device performance parameters for GaAs obtained by using Monte Carlo data in the models of Lehovc and Zuleeg [17] and Pucel, et al [18].

A. Channel width = $0.3\mu\text{m}$, Channel length = $1.5\mu\text{m}$, Channel depth = $300\mu\text{m}$,

$$N_D = 10^{17} \text{ cm}^{-3}$$

	g_m (mS)	C_{gs} (pf)	r_{ds} (ohms)	f_t (GHz)	f_{max} (GHz)	T_t (psec)	U (db)
1a.	30.5	.364	445	13.3	24.6	9.25	14.9
1b.	25.6	.37	460	11.0	18.9	11.2	12.7
2a.	37.8	.369	1583	16.3	63.1	6.7	23.7
2b.	31.8	.38	2538	13.2	59.2	8.5	23.0

B. Channel width = $0.2\mu\text{m}$, Channel length = $0.75\mu\text{m}$, Channel depth = $300\mu\text{m}$,

$$N_D = 10^{17} \text{ cm}^{-3}$$

1a.	33.6	.192	460	27.9	54.8	4.8	21.6
1b.	28.1	.194	474	23.0	42.0	5.7	19.3
2a.	45.0	.240	872	29.9	93.6	3.6	27.2
2b.	37.0	.245	1422	24.1	87.5	4.6	26.4

Notation: g_m = transconductance, C_{gs} = gate-source capacitance, r_{ds} = small signal drain-source resistance, f_t = gain-bandwidth product, f_{max} = maximum frequency of oscillation, T_t = source-drain transit time, U = Unilateral gain at 5GHz. Also, gate voltage = 0 volts and drain-source voltage equals the pinch-off voltage. Here the number 1 denotes Lehovc and Zuleeg and number 2 denotes Pucel, et al. The letter a denotes $v_{sat} = v_{peak}$ and the letter b denotes $v_{sat} = 0.8 v_{peak}$, where v_{peak} is the maximum Monte Carlo velocity and v_{sat} is the device model saturation velocity.

TABLE 2: Summary of Monte Carlo data for Ternary and Quaternary Materials at a doping level of 10^{17} cm^{-3} and $T = 300\text{K}$.

Material	μ_o ($\text{cm}^2/\text{V sec}$)	v_{peak} (cm/sec)	E_p (kV/cm)	v (at 16 kV/cm, cm/sec)
GaAs	4900	1.82×10^7	4.5	1.12×10^7
Ga _{.5} In _{.5} As	a.	9700	3.7	1.00×10^7
	b.	8000	4.2	0.93×10^7
InP _{.6} As _{.4}	a.	7450	6.0	1.45×10^7
	b.	6750	6.5	1.40×10^7
Al _{.25} In _{.75} As	a.	10,700	4.0	$.91 \times 10^7$
	b.	8530	5.0	$.84 \times 10^7$
Ga _{.27} In _{.73} P _{.4} As _{.6}	a.	8080	4.0	1.26×10^7
	b.	7100	5.0	1.18×10^7
Al _{.25} In _{.75} P _{.25} As _{.75}	a.	8800	4.5	0.90×10^7
	b.	7000	5.5	0.94×10^7
Ga _{.25} In _{.75} P _{.84} Sb _{.16}	a.	6000	6.5	1.60×10^7
	b.	5100	6.5	1.60×10^7

Notation: μ_o = low-field (100 V/cm) mobility, v_{peak} - peak velocity, E_p - electric field intensity for $v = v_{\text{peak}}$. Here a denotes calculations without alloy scattering and b denotes calculations with alloy scattering.

TABLE 3: Device performance parameters for ternary and quaternary materials using the device model of Pucel, et al [18]. Results are listed both with (b) and without (a) alloy scattering. For notation see Table 1. The device gate length is 1.5 μm .

Material	g_m (mS)	C_{gs} (pf)	r_{ds} (ohms)	f_t (GHz)	f_{max} (GHz)	τ_t (psec)	U(db) at 5GHz
GaAs	37.8	.369	1583	16.3	63.1	6.7	23.7
Ga _{.5} In _{.5} As	a:	.386	1792	25.4	88.5	4.2	26.7
	b:	.407	1223	19.9	78.5	5.5	25.5
InP _{.6} As _{.4}	a:	.359	1545	27.9	81.6	3.7	26.1
	b:	.365	631	25.5	77.4	4.1	25.6
Al _{.25} In _{.75} As	a:	.359	526	31.3	95.5	3.3	27.5
	b:	.387	1127	21.8	84.0	5.0	26.2
Ga _{.27} In _{.73} P _{.4} As _{.6}	a:	.365	1652	26.8	84.6	3.9	26.4
	b:	.373	770	24.0	78.7	4.4	25.7
Al _{.25} In _{.75} P _{.25} As _{.75}	a:	.357	654	27.9	89.2	3.7	26.9
	b:	.368	846	23.2	78.3	4.6	25.7
Ga _{.25} In _{.75} P _{.84} Sb _{.16}	a:	.348	650	25.3	76.0	4.1	25.5
	b:	.349	626	24.2	69.7	4.2	24.8

TABLE 4: Device performance parameters for $Al_{.25}In_{.75}P_{.25}As_{.75}$ illustrating the effects of different alloy scattering potentials. The calculations use the model of Lehocve and Zuleeg [17] and are for a device with a $1.5 \mu m$ gate length and channel doping = $10^{17} cm^{-3}$. The GaAs parameters are shown for comparison.

	g_m (mS)	C_{gs} (pf)	r_{ds} (ohms)	f_t (GHz)	f_{max} (GHz)	T_t (psec)
a) No alloy	57.9	.407	235	22.6	41.7	5.34
b) ΔU_{EN}	56.7	.408	236	22.1	40.5	5.46
c) ΔU_{EA}	47.5	.406	294	18.6	34.8	6.49
d) ΔU_{EG}	42.7	.410	303	16.6	29.8	7.28
e) GaAs	30.5	.364	445	13.3	24.6	9.25

Notation: (see ref. 20): ΔU_{EN} - scattering potential using electron-egativity difference, ΔU_{EA} - using electron affinity difference, ΔU_{EG} - using band gap difference.

Figure 1. Quaternary composition-al plane illustrating interpolation procedure. The T_{ij} 's are ternary parameters and Q is the interpolated quaternary parameter.

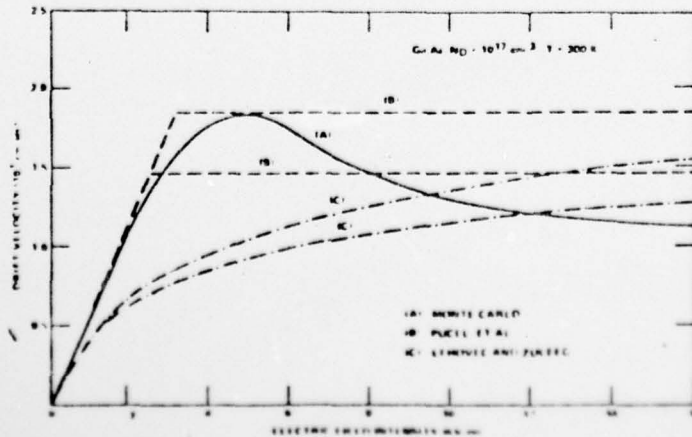
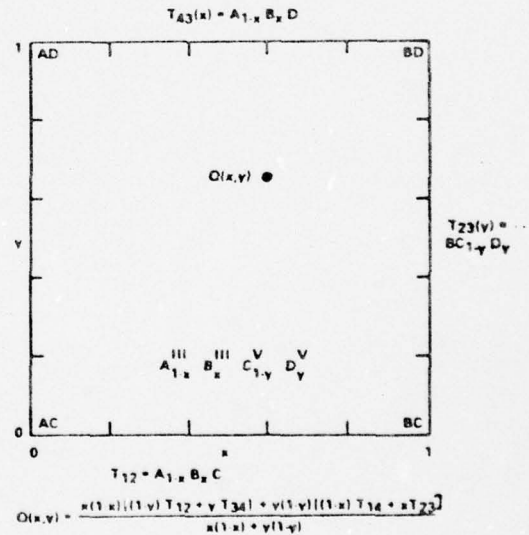


Figure 2. Velocity-field characteristic from Monte Carlo method (A) compared to approximations for device models (B & C).

AD-A053 585

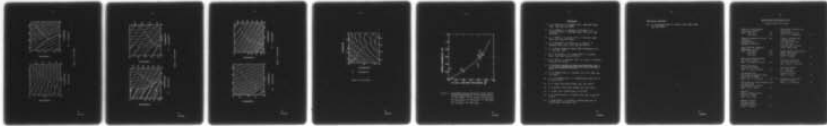
NORTH CAROLINA STATE UNIV RALEIGH DEPT OF ELECTRICAL--ETC F/G 20/12
A THEORETICAL SEARCH FOR SUPER-VELOCITY SEMICONDUCTORS. (U)
JAN 78 M A LITTLEJOHN, J R HAUSER

N00014-76-C-0480

NL

UNCLASSIFIED

2 OF 2
AD
A053 585



END
DATE
FILMED
6-78
DDC

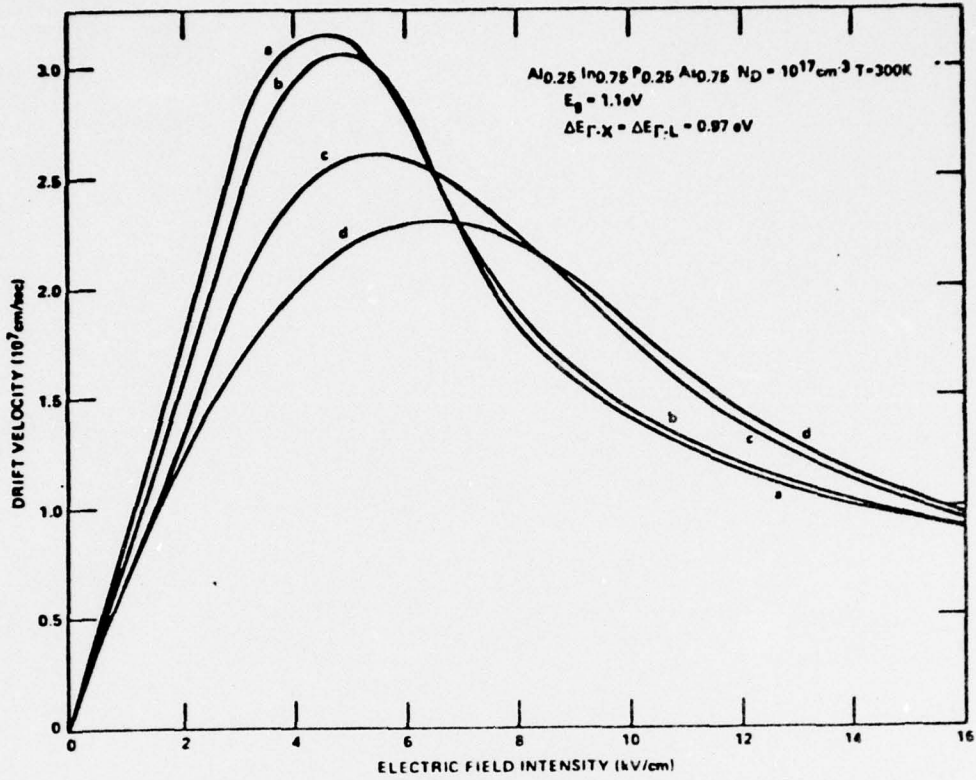


Figure 3. Monte Carlo velocity-field curves for $\text{Al}_{0.25}\text{In}_{0.75}\text{P}_{0.25}\text{As}_{0.75}$ illustrating effects of alloy scattering. See Table 4 for notation (a-d).

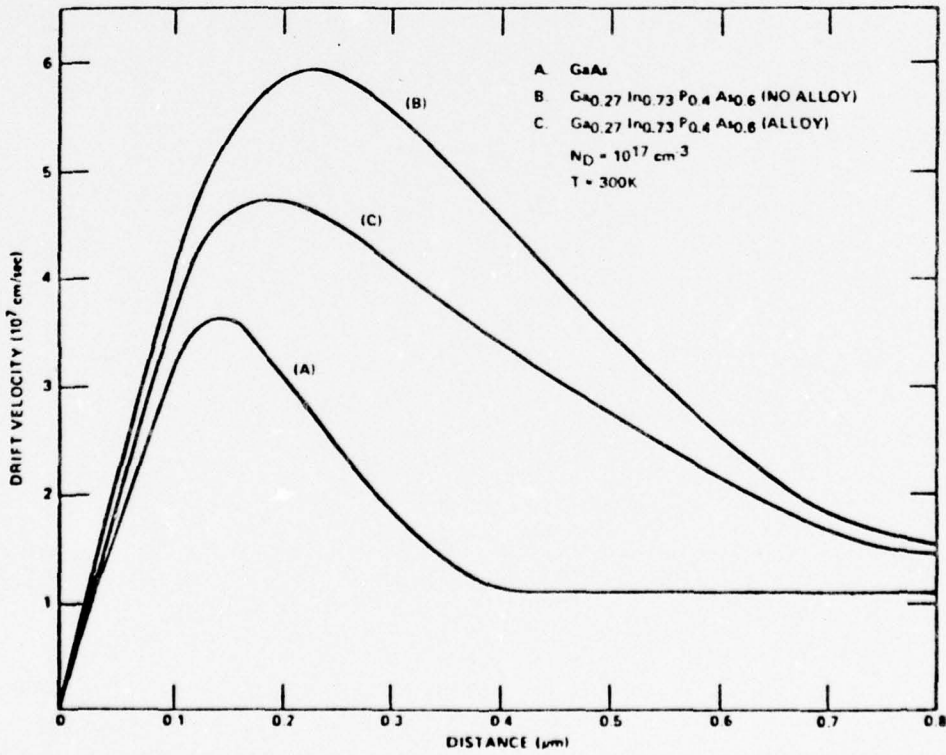


Figure 4. Velocity overshoot for GaAs and $\text{Ga}_{0.27}\text{In}_{0.73}\text{P}_{0.4}\text{As}_{0.6}$.

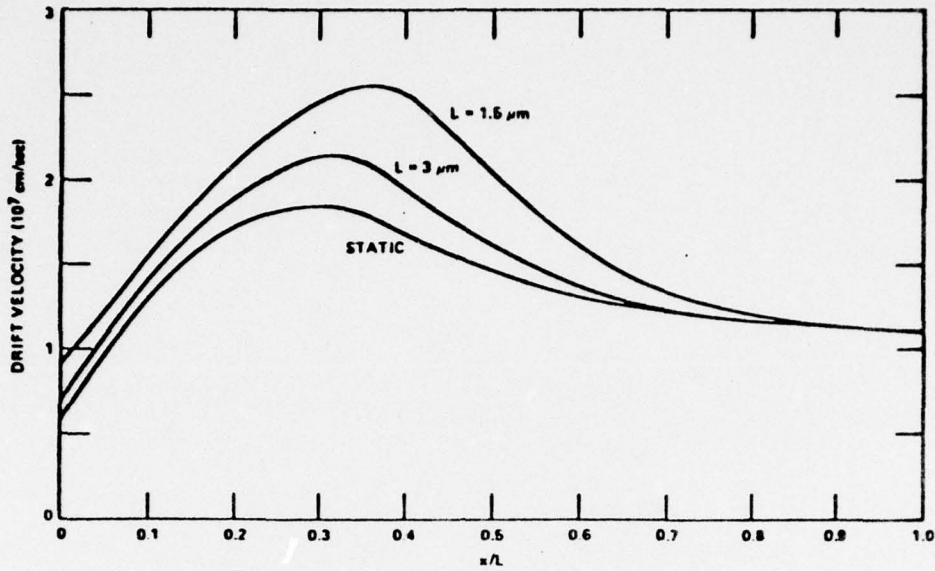


Figure 5. Velocity versus distance for GaAs with a linear field increasing from 1kV/cm ($x=0$) to 16 kV/cm ($x=L$).

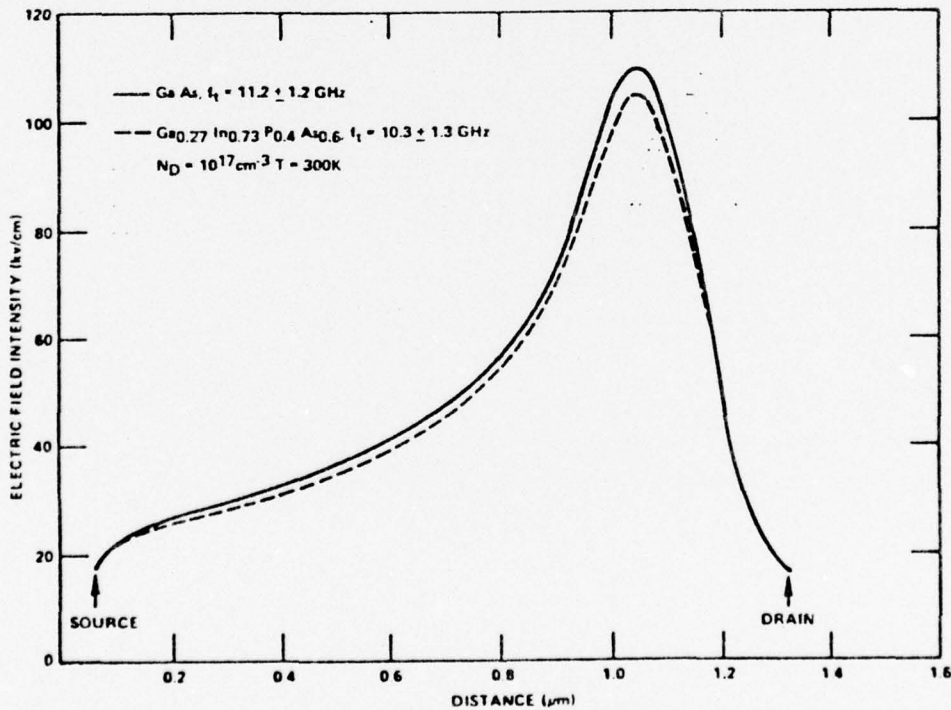


Figure 6. Static field distribution between source and drain from a device model; f_t is calculated from the total transit time between source and drain.

ENERGY BANDGAP AND LATTICE CONSTANT
CONTOURS OF III-V QUATERNARY ALLOYS*

T. H. Glisson, J. R. Hauser, M. A. Littlejohn, C. K. Williams

North Carolina State University
Electrical Engineering Department
Raleigh, North Carolina 27607

Energy band gap and lattice constant contours are presented for the nine quaternary alloys formed from Al, Ga, In and P, As, Sb. The quaternary bandgaps were obtained using an interpolation formula proposed by Moon *et al.* The quaternary lattice constants were obtained by use of a linear interpolation technique using the binary lattice constants as boundary values.

Key words: quaternary alloys, bandgap, lattice constant.

Introduction

There has been considerable interest in the quaternary III-V semiconductor materials for many applications, such as electro-optics and microwave devices [1-6]. One significant reason for this interest is the ability to synthesize materials with a fixed lattice constant and a variable range of energy bandgaps or, conversely, to synthesize materials with a constant energy bandgap and a variable lattice constant [7].

*This work was supported by a research grant from the Office of Naval Research, Washington, D.C.

In order to predict the energy bandgap or lattice constant for a quaternary material a two-step sequence is involved. Initially, it is necessary to have available experimental (or theoretical) values of these material parameters for the four possible binary III-V constituents of the quaternary compound. These values are readily available for most III-V materials in the literature [8]. There are also four possible ternary (pseudobinary) III-V systems in a given quaternary compound. In the first step, the energy bandgap and lattice constant as a function of alloy composition for each ternary system is computed from the known binary material parameters. This computation is on a good experimental and theoretical basis [9-13] involving the use of Vegard's law and the concept of the "bowing parameter" for the energy bandgap [14]. The final step involves the use of the compositional dependence of the energy bandgap and lattice constant for the four ternary combinations to interpolate to the desired quaternary energy bandgap and lattice constant. This final interpolation step is somewhat empirical in nature. There appear to be several such interpolation techniques used in the literature [6,7,15] and while these are similar, they also have non-trivial differences. This paper will discuss this critical interpolation procedure in view of the small amount of experimental quaternary data, and will present calculations for energy bandgaps and lattice constants for the nine quaternary alloys formed from Al, Ga, In and P, As, Sb using one of these interpolation techniques.

Notation

There appears to be no generally-accepted scheme for symbolically describing the III-V quaternary alloys. In this paper the following convention has been adopted. Within both the group III and group V pairing, the first position is occupied by the element with lowest atomic number. The composition variables are associated with the four elements in the order $1-x$, x , $1-y$, y . For example, a quaternary alloy will be denoted as $A_{1-x} B_x C_{1-y} D_y$. Here A and B are group III elements with A having lower atomic number than B. Likewise, C and D are group V elements with C having lower atomic number than D. Following previous authors [6,7], a quaternary alloy parameter (e.g., bandgap or lattice constant) is described by a surface $Q(x,y)$ over

In order to predict the energy bandgap or lattice constant for a quaternary material a two-step sequence is involved. Initially, it is necessary to have available experimental (or theoretical) values of these material parameters for the four possible binary III-V constituents of the quaternary compound. These values are readily available for most III-V materials in the literature [8]. There are also four possible ternary (pseudobinary) III-V systems in a given quaternary compound. In the first step, the energy bandgap and lattice constant as a function of alloy composition for each ternary system is computed from the known binary material parameters. This computation is on a good experimental and theoretical basis [9-13] involving the use of Vegard's law and the concept of the "bowing parameter" for the energy bandgap [14]. The final step involves the use of the compositional dependence of the energy bandgap and lattice constant for the four ternary combinations to interpolate to the desired quaternary energy bandgap and lattice constant. This final interpolation step is somewhat empirical in nature. There appear to be several such interpolation techniques used in the literature [6,7,15] and while these are similar, they also have non-trivial differences. This paper will discuss this critical interpolation procedure in view of the small amount of experimental quaternary data, and will present calculations for energy bandgaps and lattice constants for the nine quaternary alloys formed from Al, Ga, In and P, As, Sb using one of these interpolation techniques.

Notation

There appears to be no generally-accepted scheme for symbolically describing the III-V quaternary alloys. In this paper the following convention has been adopted. Within both the group III and group V pairing, the first position is occupied by the element with lowest atomic number. The composition variables are associated with the four elements in the order $1-x$, x , $1-y$, y . For example, a quaternary alloy will be denoted as $A_{1-x}B_xC_{1-y}D_y$. Here A and B are group III elements with A having lower atomic number than B. Likewise, C and D are group V elements with C having lower atomic number than D. Following previous authors [6,7], a quaternary alloy parameter (e.g., bandgap or lattice constant) is described by a surface $Q(x,y)$ over

the x, y composition plane ($0 < x < 1, 0 < y < 1$). At the corners (x and y equal to zero and/or one) the values of the parameter for the four binary elements $Q(0,0) = B_1$, $Q(1,0) = B_2$, $Q(1,1) = B_3$ and $Q(0,1) = B_4$ are obtained. Along the boundaries of the plane the parameter for the four ternary elements $Q(x,0) = T_{12}(x)$, $Q(1,y) = T_{23}(y)$, $Q(x,1) = T_{43}(x)$ and $Q(0,y) = T_{14}(y)$ are obtained.

Estimation of Alloy Parameters

Many ternary alloy parameters (e.g. lattice constant) are obtained by linear interpolation from those of the constituent binary compounds, i.e.,

$$T_{ij}(x) = xB_j + (1-x)B_i \quad (1)$$

For some parameters the theoretical variation with composition is nonlinear [14,16]. For the direct bandgap for example, Thompson and Woolley [9] have shown that

$$T_{ij}(x) = xB_j + (1-x)B_i - C_{ij}x(1-x) \quad (2)$$

where C_{ij} is the bowing parameter for the ternary alloy bandgap T_{ij} .

In the absence of definitive theories for quaternary parameters, estimates of a quaternary alloy parameter $Q(x,y)$ must be obtained by interpolation from the four ternary alloy parameters T_{ij} . Various interpolation schemes have been proposed. Onton and Chicotka [15] used the solution of Laplace's equation subject to the boundary conditions $Q(x,0) = T_{12}(x)$, etc. In Monte Carlo transport studies [6] the present authors have used the interpolation equation

$$Q(x,y) = \frac{x(1-x)[(1-y)T_{12}(x) + yT_{43}(x)] + y(1-y)[(1-x)T_{14}(y) + xT_{23}(y)]}{x(1-x) + y(1-y)} \quad (3)$$

This interpolation equation reduces to the ternary parameters on the quaternary plane boundaries and to the average

of the ternary parameters at the midpoint ($x=0.5, y=0.5$) of the compositional plane. This is incidentally the solution to Laplace's equation if the T_{ij} are linear as in Eq. (1). Moon et al. [7] have proposed similar schemes for the estimation of lattice constant and bandgap. For the lattice constant, Moon gives (in the above notation)

$$Q(x,y) = B_1 + (B_2 - B_1)x + (B_4 - B_1)y + (B_1 - B_2 + B_3 - B_4)xy \quad (4)$$

For the lattice constant, the T_{ij} are assumed to be linear in their arguments, so the solution to Laplace's equation is identical to Eq. (3), which in turn also reduces to Eq. (4).

For the bandgap, Moon et al. have used the equation

$$Q(x,y) = (1-x)T_{14}(y) + x T_{23}(y) - \Delta \quad (5)$$

where the T_{ij} are determined from Eq. (1) and

$$\Delta = x(1-x)[(1-y)C_{12} + yC_{43}] + y(1-y)[(1-x)C_{14} + xC_{23}] \quad (6)$$

An important difference between this bandgap estimate and that obtained from Eq. (3) is in the manner in which the ternary bowing parameters C_{ij} enter the calculation. In Eq. (3), the ternary bowing effects are included in the T_{ij} , whereas in Moon's method the bowing enters as a separate quaternary bowing parameter term given in Eq. (6). At the center of the composition plane, Eq. (3) yields (for the quaternary bowing) $1/16 (C_{12} + C_{43} + C_{14} + C_{23})$ and Eq. (5) gives $1/8 (C_{12} + C_{43} + C_{14} + C_{23})$, which is twice as large. Thus, at the center, Eq. (3) gives the average of the bowing contributions from the four ternaries, whereas Eq. (5) gives the average of the bowing contributions from the two sublattices. This is the principle difference between the interpolation schemes of Refs. 6 and 7.

Comparison with Experiment

Onton and Chicotka compared their interpolation approach (solution to Laplace's equation) with measured values of the quaternary bandgap in $\text{Ga}_{1-x}\text{In}_x\text{P}_{1-y}\text{As}_y$ and found the interpolated values to be within ± 30 meV of the measured values. We have repeated this comparison, using their measured data. The results are given in Table 1. The average error and standard deviation of the error are also shown, and it is seen that Eqs. (3) and (5) give comparable errors.

Table I. Comparison of Eqs (3) and (5) with Experimental Data for $\text{Ga}_{1-x}\text{In}_x\text{P}_{1-y}\text{As}_y$.

Composition		Bandgap (eV)		
x	y	Eq (3)	Eq (5)	Measured [15]
0.004	0.260	2.357	2.353	2.222
0.006	0.340	2.244	2.239	2.124
0.006	0.420	2.136	2.131	1.993
0.009	0.500	2.027	2.020	1.881
0.008	0.590	1.913	1.907	1.738
0.010	0.710	1.763	1.755	1.592
0.012	0.830	1.619	1.609	1.475
0.017	0.910	1.521	1.510	1.351
0.015	0.970	1.455	1.447	1.326
0.060	0.220	2.336	2.297	2.203
0.060	0.280	2.255	2.214	2.135
0.070	0.340	2.160	2.113	2.038
0.080	0.440	2.014	1.963	1.869
0.110	0.650	1.709	1.650	1.535
0.110	0.700	1.649	1.591	1.472
0.170	0.850	1.383	1.326	1.236
0.190	0.975	1.184	1.166	1.165
0.250	0.140	2.124	2.054	2.101
0.230	0.190	2.100	2.021	2.041
0.250	0.240	2.008	1.921	1.953
0.250	0.310	1.924	1.830	1.809
0.260	0.630	1.523	1.430	1.388
0.330	0.800	1.225	1.145	1.170
0.340	0.090	2.029	1.971	2.077

Table I continued.

Composition		Bandgap (eV)		
x	y	Eq (3)	Eq (5)	Measured [15]
0.370	0.120	1.954	1.883	1.978
0.410	0.170	1.843	1.757	1.850
0.400	0.030	1.983	1.957	2.086
0.460	0.040	1.887	1.854	2.019
0.500	0.040	1.830	1.797	1.953
0.570	0.060	1.723	1.678	1.854
0.650	0.060	1.625	1.580	1.750
0.710	0.060	1.558	1.513	1.686
0.830	0.100	1.401	1.346	1.470
0.870	0.130	1.333	1.276	1.389
0.920	0.190	1.216	1.166	1.268
Average error (eV)		-0.052	-0.008	
rms error (eV)		0.109	0.118	

Calculation of Lattice Constant and Bandgap

For the calculation of the lattice constant, the three methods discussed above are identical, as given in Eq. (4). For the calculation of the bandgap, we have elected to use Moon's procedure, since it has some theoretical basis, whereas the other two are more or less ad hoc.

The quaternary lattice constant and energy bandgap contours are presented in Figure 1(a)-(i). These contours were obtained by numerical solutions of Eqs. (4) and (5), using the data given in Table 2. In all cases, the lowest quaternary bandgap is plotted in Figure 1. The shaded regions represent compositions for which the quaternary alloy is an indirect bandgap material.

Table II. Parameters Used in the Calculation of Quaternary Bandgaps and Lattice Constants

Compound	Bandgaps (ev)			Lattice Constant (Å)
	$\Gamma(000)$	X(100)	L(111)	
AlP	3.6	2.42	4.0	5.462
AlAs	2.95	2.153	3.3	5.6611
AlSb	2.25	1.52	1.85	6.135
GaP	2.74	2.26	3.0	5.4495
GaAs	1.439	1.961	1.769	5.64191
GaSb	0.69	1.11	0.765	6.094
InP	1.34	2.04	1.87	5.86875
InAs	0.359	2.1	1.6	6.0584
InSb	0.175	1.0	0.63	6.47877

a) Binary bandgaps and lattice constants

Alloy	Bowling Parameter		
	$\Gamma(000)$	X(100)	L(111)
(Al,Ga)P	0.0*	0.0	0.0
(Al,Ga)As	0.26	0.02	0.45
(Al,Ga)Sb	0.0	0.0	0.0
(Al,In)P	0.0	0.0	0.0
(Al,In)As	0.52*	0.0	0.0
(Al,In)Sb	0.42*	0.0	0.0
(Ga,In)P	0.758	0.15	0.68
(Ga,In)As	0.6	0.15	0.5
(Ga,In)Sb	0.43	0.24	0.33
Al(P,As)	0.22*	0.0	0.0
Al(P,Sb)	1.2*	0.0	0.0
Al(As,Sb)	0.72*	0.0	0.0
Ga(P,As)	0.21	0.21	0.25
Ga(P,Sb)	1.2*	0.0	0.0
Ga(As,Sb)	0.65*	0.0	0.0
In(P,As)	0.27	0.27	0.26
In(P,Sb)	1.2	0.0	0.0
In(As,Sb)	0.596	0.6	0.55

b) Ternary bowling parameters

*denotes estimate from Figure 2. In the X&L valleys unknown parameters are equated to zero.

Estimation of Unknown Ternary Bowing Constants

Relatively few of the III-V ternary bowing constants are known with any certainty, especially for the X(100) and L(111) valleys. Figure 2 shows the reported bowing parameters for several ternary materials as a function of the lattice constant difference between the two end-point binary compounds. While there is some uncertainty in the experimental data there does appear to be a definite trend toward larger bowing parameters with larger lattice constant differences. The solid line relationship shown in Figure 2 has been used to estimate several unknown bowing constants, as identified by the asterisks in Table 2. Since bowing is known to occur, it was felt that this procedure is better than arbitrarily setting the unknown bowing constants to zero.

Summary

Calculated bandgap and lattice constant contours have been presented for nine quaternary III-V material systems. The calculated values are based upon interpolation techniques which use known values of ternary III-V parameters to estimate the bandgap and lattice constant parameters for the quaternary systems. Since there is some uncertainty in both the ternary parameters and the best interpolation technique these calculated values must be considered as first order approximations until more experimental data is obtained for the quaternary systems. However, the curves should prove useful for many studies of the general properties of the increasingly important III-V quaternary materials.

Acknowledgments

We would like to express our appreciation to J. Shade for his assistance in this work.

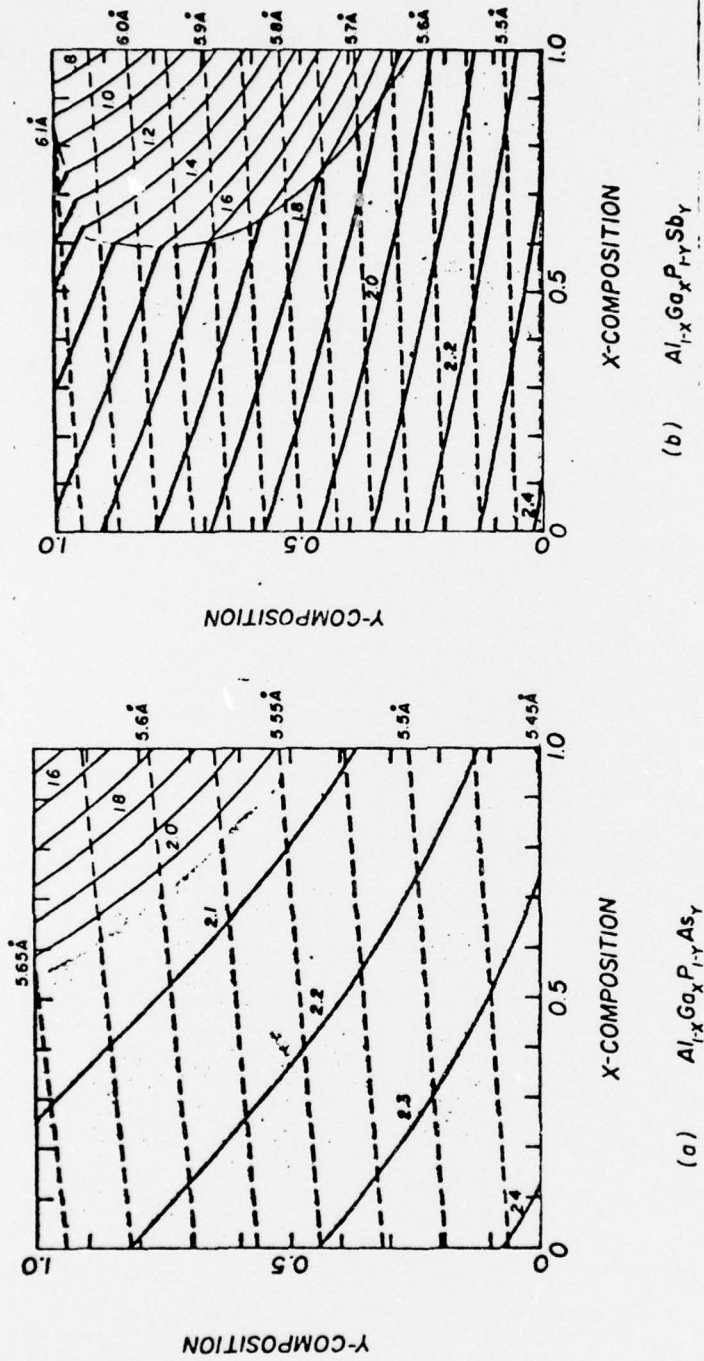
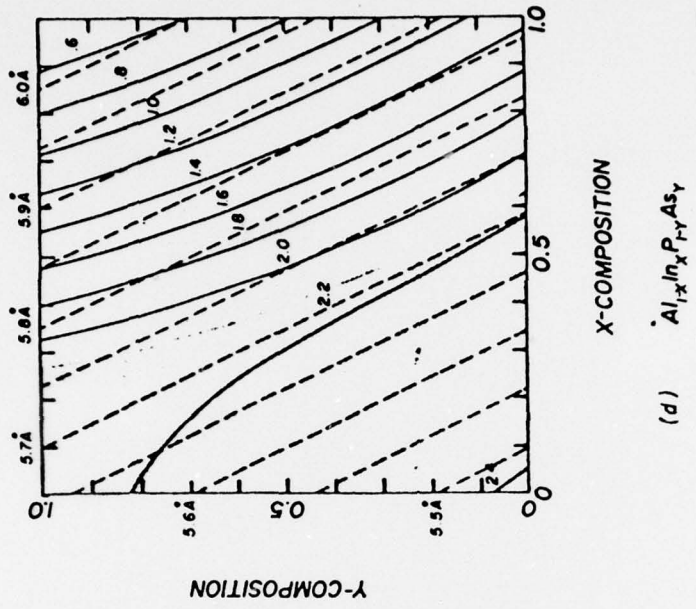
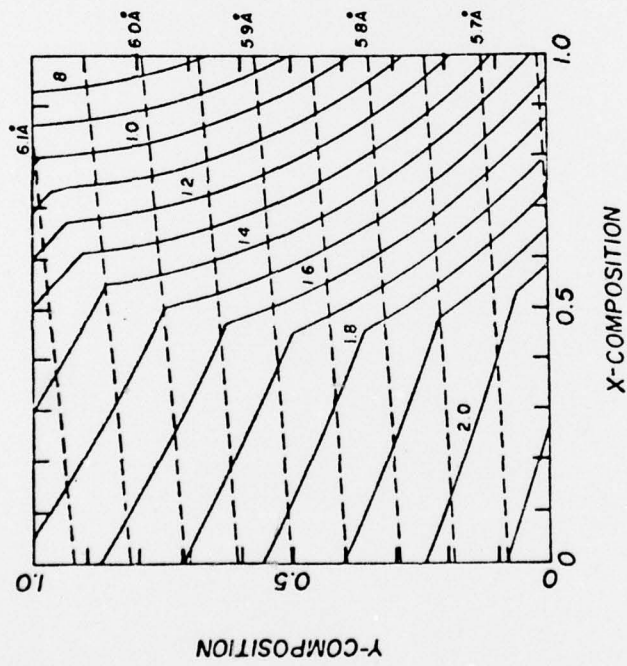


Figure 1. Energy bandgap and lattice constant contours for III-V quaternary alloys. The solid curves are the energy gap contours and the dashed curves are lattice constant contours. The shaded region shows the compositional range over which the material has an indirect bandgap.



(c) $Al_{1-x}Ga_xAs_{1-y}Sb_y$



(d) $Al_{1-x}In_xP_{1-y}As_y$

Figure 1 (continued)

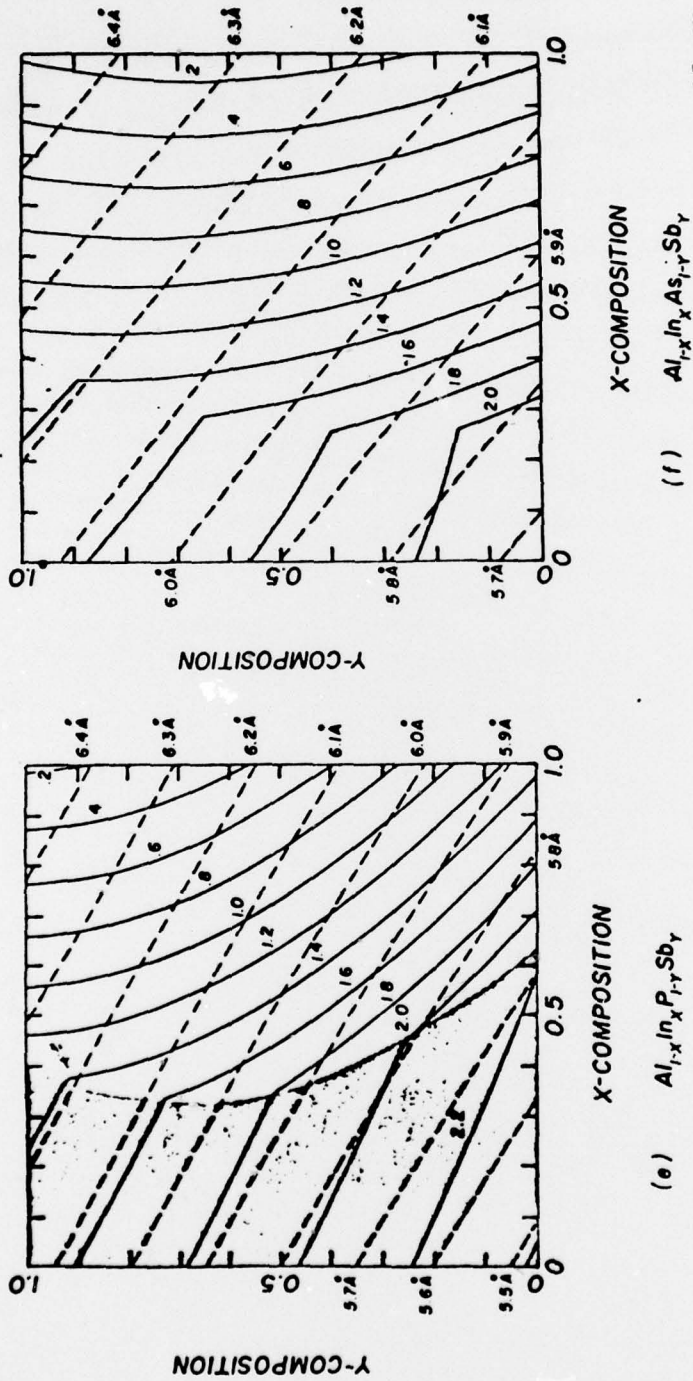


Figure 1 (continued)

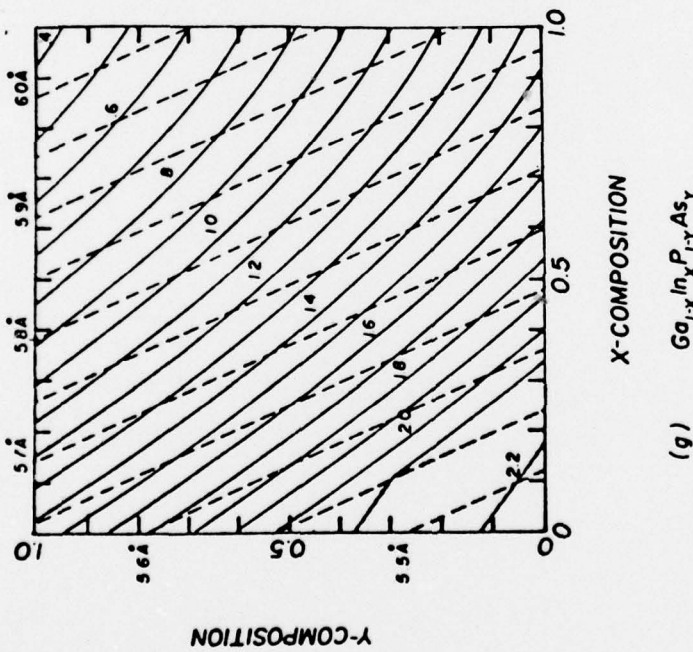
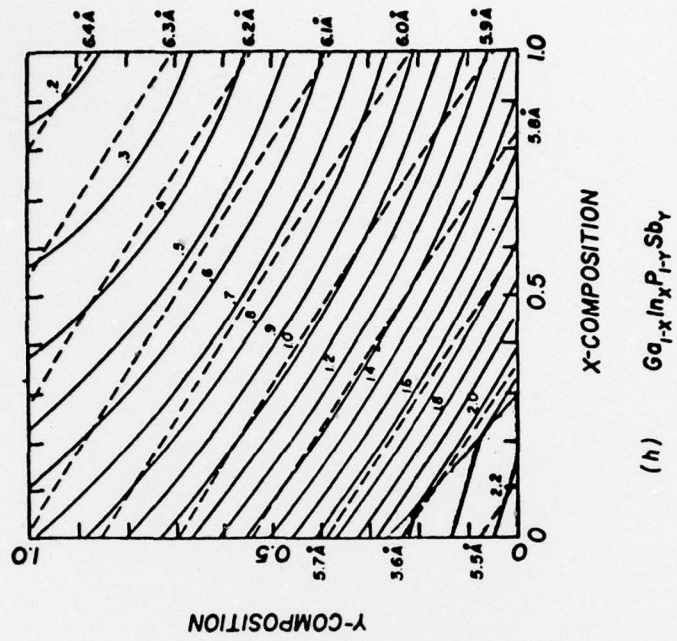


Figure 1 (continued)

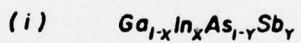
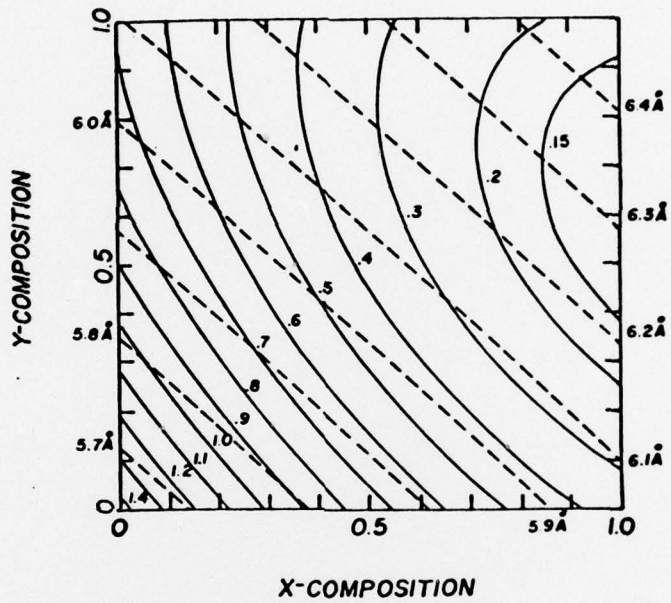


Figure 1 (continued)

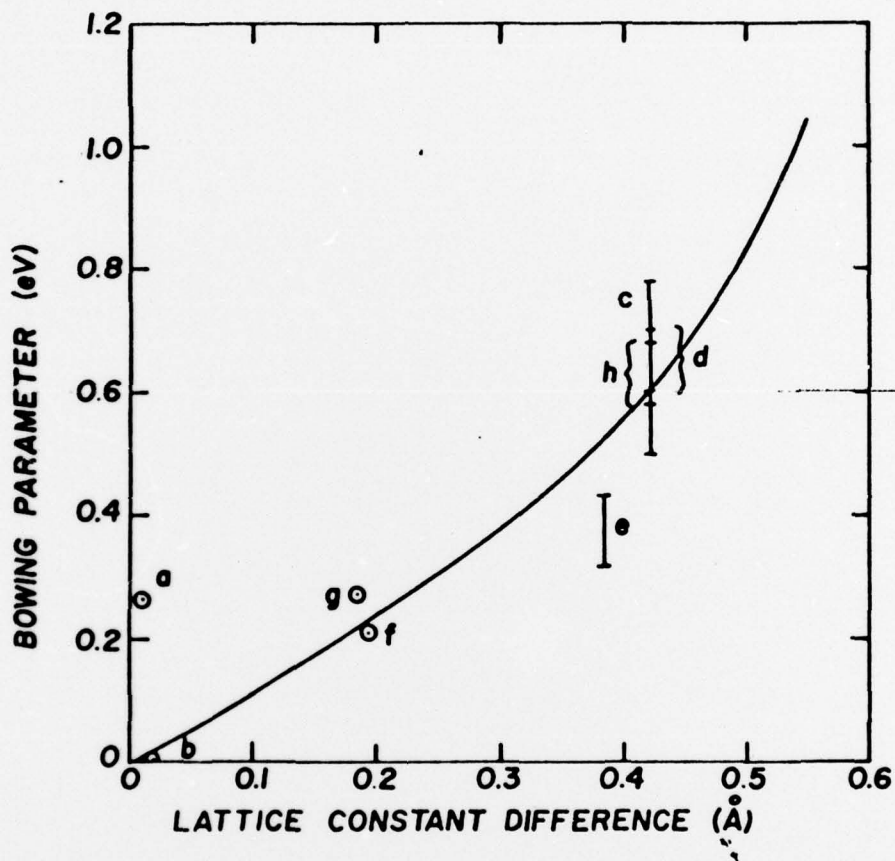


Figure 2. Experimental bowing parameters versus lattice constant difference for III-V ternary alloys. (a) $\text{Al}_{1-x}\text{Ga}_x\text{As}$, (b) $\text{Al}_{1-x}\text{Ga}_x\text{Sb}$, (c) $\text{Ga}_{1-x}\text{In}_x\text{P}$, (d) $\text{Ga}_{1-x}\text{In}_x\text{As}$, (e) $\text{Ga}_{1-x}\text{In}_x\text{Sb}$, (f) $\text{GaP}_{1-x}\text{As}_x$, (g) $\text{InP}_{1-x}\text{As}_x$, (h) $\text{InAs}_{1-x}\text{Sb}_x$.

References

1. J. S. Etcher, G. A. Antypas, and J. Edgecombe, Appl. Phys. Lett. 29, 153 (1976).
2. P. D. Wright, J. J. Coleman, N. Holonyak, M. J. Ludowisc, and G. E. Stillman, Appl. Phys. Lett. 29, 18 (1976).
3. J. J. Hsieh, J. A. Rossi, and J. P. Donnelly, Appl. Phys. Lett. 28, 709 (1976).
4. T. P. Pearson, B. I. Miller, R. J. Clark, K. J. Bachmann, Appl. Phys. Lett. 28, 499 (1976).
5. C. J. Neuse, Technical Digest IEDM, Washington, D.C., p. 125, Dec. 1976.
6. M. A. Littlejohn, J. R. Hauser, and T. H. Glisson, Appl. Phys. Lett. 30, 242 (1977).
7. R. L. Moon, G. A. Antypas, and L. W. James, J. Electron. Mater. 3, 635 (1974).
8. M. Neuberger, Handbook of Electronic Materials, vol. 2, III-V Semiconducting Compounds (IFI/Plenum, New York, 1971).
9. A. G. Thompson and J. C. Woolley, Can. Jour. Phys. 45, 255 (1967).
10. J. A. Van Vechten and T. K. Bergstresser, Phys. Rev. B 1, 3351 (1970).
11. K. S. Song, Solid State Commun. 13, 1397 (1973).
12. M. Altarelli, Solid State Commun. 15, 1607 (1974).
13. A. Onton, Jour. Luminescence 7, 95 (1973).
14. J. W. Harrison and J. R. Hauser, Phys. Rev. B 13, 5347 (1976).
15. A. Onton and R. J. Chicotka, International conf. on Luminescence, Leningrad, 1972.

References continued.

16. J. W. Harrison and J. R. Hauser, Jour. Appl. Phys.
47, 292 (1976).

ANNUAL REPORT DISTRIBUTION LIST

Contract N00014-76-C-0480

Office of Naval Research Arlington, VA 22217 Attn: Code 427 (4) Code 102IP (6)	Westinghouse Research Lab Beulah Road Pittsburgh, PA 15235 Attn: H. C. Nathanson (1)
Defense Documentation Center (12) Building 5 Cameron Station Alexandria, VA 22314	Rockwell International Science Center 1049 Camino Dos Rios P. O. Box 1085 Thousand Oaks, CA 91360 Attn: Daniel Chen (1)
Naval Research Laboratory Washington, DC 20375 Attn: Code 2627 (6) Code 5220 (1) Code 5211 (1)	Hughes Research Laboratories Malibu Canyon Road Malibu, CA 90265 Attn: C. Krumm (1)
Naval Ocean Systems Center San Diego, CA 92152 Attn: H. Wieder, Code 922 (1)	Washington University St. Louis, MO 63130 Attn: Prof. C. M. Wolfe (1)
Varian Associates Palo Alto, CA 94303 Attn: R. Bell, Box K101 (1)	Texas Instruments Mail Stop 118 P. O. Box 5012 Dallas, TX 75222 Attn: D. Shaw (1)
RCA Laboratories David Sarnoff Research Center Princeton, NJ 08540 Attn: Dr. Y. S. Narayan (1) (1)	University of Illinois Urbana, IL 61801 Attn: G. E. Stillman (1)
TRW Defense and Space Systems Group One Space Park Redondo Beach, CA 90278 Attn: Dr. T. Mills (1)	
Motorola 5005 E. McDowell Street Phoenix, AZ 85008 Attn: T. S. Heng (1)	
Raytheon Company 28 Seyon Street Waltham, MA 02154 Attn: R. Berig (1)	